Dynamics and Instabilities of Free Surface and Vortex Flows

Tophøj, Laust Emil Hjerrild

Publication date:
2012

Document Version
Publisher's PDF, also known as Version of record

Dynamics and Instabilities of Free Surface and Vortex Flows

Laust Tophøj
laustemil@gmail.com
March 14, 2012

PhD thesis from DTU Physics,
Technical University of Denmark (DTU)

Supervisors:

Tomas Bohr
DTU Physics

Hassan Aref
Fluid DTU & Virginia Tech.

Contents

Summary

This PhD thesis consists of two main parts. The first part describes the dynamics of an ideal fluid on a stationary free surface of a given shape. It turns out that one can formulate a set of self-contained equations of momentum conservation for the tangential flow, with no reference to the flow of the fluid bulk. With these equations, one can in principle predict the surface flow on a given free surface, once its shape has been measured. The equations are expressed for a general surface using Riemannian geometry and their solutions are discussed, including some difficulties that may arise. Furthermore, the equations are applied to an experiment involving a poorly understood symmetry-breaking instability of a rotating fluid with a free surface, cf. Bergmann et al., [*J. Fl. Mech.* **679**, 415-431 (2011)], with the result confirmed by direct measurement. This experiment is discussed in some detail together with an ongoing investigation of the fluid motion in question and the elusive instability mechanism. The second main part of the thesis describes work on point vortex dynamics and instability. The problem of point vortex pair scattering is briefly revisited together with a short discussion of chaotic advection, and the stability of vortex leapfrogging is investigated within the framework of Floquet theory. An analytical criterion is found, giving the exact location of the transition to instability earlier observed in numerical investigations by Acheson [*Eur. J. Phys.* **21**, 269-273 (2000)]. Finally, an experimental work on elastic collisions of wet spheres is briefly discussed.

Summary in Danish

Overflade- og hvirvelstrømninger: Dynamik og instabiliteter

Denne PhD-afhandling består af to hoveddele. I første del præsenteres en undersøgelse af ideelle væskestrømninger på en stationær fri overflade af en givet form. Ved projektion af Euler-ligningerne på overfladens tangentplan udledes dynamiske ligninger for strømningen i overfladen, uafhængigt af strømningen under overfladen. Med disse ligninger kan man i princippet bestemme strømningen på en stationær fri overflade, hvis man først måler overfladens form. Ligningerne udledes for en generel overflade beskrevet som en Riemannsk mangfoldighed, og løsningsmulighederne diskuteres. Disse resultater anvendes på et eksperimentelt studie af et endnu dårligt forstået symmetribrud i en roterende væskestrømning, se Bergmann et al., [*J. Fl. Mech.* **679**, 415-431 (2011)]. Resultaterne bekræftes ved direkte måling. Desuden diskuteres eksperimentet og en igangværende undersøgelse af den involverede komplekse væskedynamik og mekanismen bag det omtalte symmetribrud. I afhandlingens anden del præsenteres resultater om punkthvirveldynamik og instabilitet. Kollisioner af punkthvirvler studeres sammen med kaotisk partikelbevægelse i ideelle væskestrømninger. Desuden undersøger vi en hvirvelbevægelse, såkaldt "leapfrogging", hvor to hvirvelpar overhaler hinanden på skift i en periodisk bevægelse. Bevægelsens stabilitet analyseres, og vi finder et eksakt kriterie for overgangen til instabilitet, der bekræfter resultatet af en numerisk undersøgelse udført af D. Acheson [*Eur. J. Phys.* **21**, 269-273 (2000)]. Sluttelig præsenteres resultaterne fra et kort eksperimentelt studie af elastiske kollisioner mellem våde partikler.

Populært Resumé

Strømninger i vand bemærkes ofte ved at overfladen ændrer form. Vi kender det fra håndvasken, hvor en fordybning i vandoverfladen over afløbet fortæller os, at der er en hvirvel dernede. Men hvad kan man engentlig sige om strømningen, hvis man kender overfladens form? Det viser sig, at man kan sige en hel del. I afhandlingens første del beskrives en teori for strømningen på en vandoverflade af konstant form. Desuden diskuteres et eksperiment, hvor en roterende væske i en rund beholder pludselig bliver ustabil og går fra en cirkulær til en kantet form. Teorien for overfladestrømninger bruges på dette eksperiment, og jeg fortæller om vores forsøg på at forstå de mystiske kantede former i strømningen. Afhandlingens anden del beskriver dynamikken i en simpel model af hvirvelstrømninger. Jeg præsenterer resultater om kaotisk bevægelse i et system af hvirvler og stabiliteten af den såkaldte "leapfrog"-bevægelse, hvor to par af hvirler overhaler hinanden på skift. Bevægelsen er ustabil under bestemte betingelser, som bestemmes matematisk.

Introduction

This thesis gives a condensed account of my PhD project at DTU Physics in 2008-2012. A number of research papers are included, some of which have been published in journals, while others have been submitted for review. Not included is the number of failed ideas and the hours of futile work spent during the project.

The thesis is divided into two main chapters, each containing a set of papers. In the introduction to each set, I give a brief account of the papers and the work leading up to them. The style of these introductory sections is informal, and squarely technical discussions are reserved for the included papers.

Chapter 1 deals with the description of free surface flows and my efforts to analyze an experiment performed at DTU Physics. Much will be said about this so-called "rotating polygon" experiment in chapter 1. The main part of the chapter deals with the introduction and application of a set of dynamical equations governing the flow of an ideal fluid on a stationary free surface. The equations find an application in an all but ideal fluid in the rotating polygon experiment. Lessons learned from the above-mentioned work is in turn applied in an ongoing work on understanding the observed phenomenon and the underlying symmetry-breaking instability.

Chapter 2 recounts a very different part of my PhD project, which was done in collaboration with my co-supervisor Hassan Aref. This work is on point vortex dynamics, a simple low-dimensional model which captures much of the dynamics of real fluid dynamics, while providing a lot of interesting problems for the mathematically inclined. In this project, we have mainly worked on an analysis of the stability of vortex leapfrogging, and we have found analytically a criterion identifying stable and unstable leapfrogging motions. This work is presented in chapter 2 along with other results on point vortex motion, in particular the scattering of vortex pairs. The chapter also gives a small preview of a piece work to come, on the scattering problem in the limit of weak interaction.

Finally, the short chapter 3 provides the results of my short visit during the PhD to the École Polytechnique in Paris, where I performed an experimental study of collisions of elastic spheres covered in a viscous film.

A complete list of references is found at the end of the thesis.

The thesis page number is shown at the bottom of each page. For those reading on a computer, the page footer provides a link to the table of contents.

This PhD project was funded by DTU Physics.
I wish to express my gratitude toward my friend and teacher Hassan Aref, who recently passed away.

Chapter 1

Modelling of Free Surface Flows

This work is motivated by an experiment first described by [Vatistas (1990)] and later by [Jansson *et al.* (2006)], whose work has been continued by the Complex Motion in Fluids Group at DTU Physics. The experiment consists of a cylindrical bucket partially filled with water. The bucket is so constructed, that the bottom plate can be rotated while the side wall is kept stationary. Thus forced, the fluid spins around at rather high speeds in a turbulent flow, and the free surface deforms considerably. The setup is carefully manufactured and arranged to have circular symmetry, so one might expect to observe a symmetric flow and free surface deformation. But on the contrary, the flow breaks the symmetry for a range of control parameters (bottom plate rotation rate, fluid viscosity and volume of fluid). Observing the shape of the free surface, one then sees a polygon-shaped deformation that rotates while keeping its shape. The rotation of the deformation is considerably slower than both that of the bottom plate and that of the fluid itself. The flow itself is complex and not too well understood, and we do not understand the symmetry-breaking instability leading to the polygon states.

While trying to understand these flows, I made an observation on the problem of deducing flow velocities from observation of the free surface shape. If one treats the fluid as ideal, i.e. free of shear forces from viscous friction between fluid particles, the flow is governed by the well-known Euler equations. Now, when the flow is stationary as seen from some (possibly rotating) frame of reference, the Euler equations can be projected onto the free surface to yield dynamical equations for the tangential flow without reference to the underlying flow in the fluid bulk. The force on fluid particles moving on the surface is given entirely in terms of potential gradients, e.g. from gravity, surface tension and possibly Coriolis forces, all of which can be calculated in terms of the free surface shape and the tangential fluid velocity components. These equations can be solved independently of the bulk flow. It is important to note that in any physical flow, the motion of the fluid bulk is has a great influence on the flow on the free surface. But, neglecting viscosity, this influence is conveyed entirely through the *shape* of the free surface, which we can in principle observe and quantify.

Aside from the rather mathematical problem mentioned above, I have been working on the dynamics of the flow. Aspects of this work are briefly discussed.

Outline

The work is presented in a reverse order, starting with the most recent paper giving an up-to-date exposition of the theory, followed by an earlier paper on the experiment that motivated the theoretical developments.

First, on pp. 9-32 I include the paper "Stationary ideal flow on a free surface of a given shape" by Laust Tophøj and Tomas Bohr. The paper was submitted to Journal of Fluid Mechanics on March 14, 2012. We set about to introduce the dynamical equations governing the free surface flow, emphasizing theoretical results. The paper introduces the mathematical formalism necessary to write the equations for a given surface, including the use of Riemannian geometry and a representation of the free surface as a smooth 2D manifold, and discusses the possibility of solving them in certain cases.

Next, on pp. p. 33-49, I include the paper "Polygon formation and surface flow on a rotating fluid" by Raymond Bermann, Laust Tophøj, Tess Homan, Pascal Hersen, Anders Andersen and Tomas Bohr, published by Journal of Fluid Mechanics in 2011, [Bergmann *et al.* (2011)]. The paper is centered on three aspects of the rotating polygon experiment: The observed dynamics of states, a detailed experimental investigation of a flow in a triangular polygon state, and an analysis of symmetric flows. The bulk of the experiments discussed were performed by Raymond Bergmann. My main contribution to the paper is section 5 on symmetric states. We speculate that the rotating polygon flows occur as a result of an instability of such states, and we are therefore very interested in a detailed understanding. Section 5 gives an account of the projected Euler equations using basic vector analysis, and the results are succesfully employed in extracting the surface flow velocities from the free surface shape, a result which is confirmed by particle tracking experiments.

This is followed on pp. 51-52 by an erratum, published by Journal of Fluid Mechanics, cf. [Bergmann *et al.* (2012)], which corrects a couple of typos and expands the discussion on the feasibility of representing the polygon flow as induced by a few point vortices, as proposed in [Vatistas *et al.* (2008)]. In the erratum, we present new calculations on the experiments by Raymond Bergmann mentioned above, including a map of the vorticity distribution of the surface flow in a triangular polygon state. This material is proving useful to us when discussing possible models of the flow with George Vatistas and his collaborators.

Finally, on pp. 53-64 the draft paper, "A model of the rotating polygon experiment using conservation of angular momentum" is presented. As discussed above,

a detailed understanding of symmetric states is essential when trying to identify the instability mechanism leading to the observed polygon flows. I present an analysis on the influx of angular momentum to the fluid in the rotating polygon experiment. Using this analysis, one can use the control parameters of the experiment, the rotation rates of the control surfaces and the water volume, to predict the shape of the resulting *symmetric* state. Arguing that the properties of the observed polygon (e.g. the number of corners) depends on the geometry of the associated symmetric state, I propose a model that reproduces the phase diagram of observed states, cf. [Jansson *et al.* (2006)], reasonably well. It seems that we are now one step closer to understand and predict the flow and surface shape resulting from a given set of control parameters.

Stationary ideal flow on a free surface of a given shape

L. TOPHØJ and T. BOHR

Physics Department & Center for Fluid Dynamics,
The Technical University of Denmark, Kgs. Lyngby

(Received 14 March 2012)

We study the stationary, ideal flow on a fluid surface of a given shape. It is demonstrated that the flow is governed by a self-contained set of equations for the surface flow field without any reference to the bulk-flow. To write down these equations for arbitrary surfaces, we apply a covariant formulation using Riemannian geometry and we show how to include surface tension and velocity dependent forces such as the Coriolis force. We write down explicitly the equations for cases where the surface elevation can be written as function of either cartesian or polar coordinates in the plane, and we obtain solutions for the important case of rotational symmetry and the perturbed flow when this symmetry is slightly broken. To understand the general character and solubility of the equations, we introduce the associated dynamical system describing the motion along the streamlines. The existence of orbits with transversal intersections, as well as quasiperiodic and chaotic solutions, show that not all boundary value problems are well-posed. In the particular case of unforced motion the stream lines are geodesic curves and in this case the existence of a non-trivial surface velocity field requires that the surface can be foliated by a family of non-intersecting geodesic curves.

1. Introduction

The close connection between surface flow and surface deformation is well known from everyday experiences as well as from laboratory experiments in fluid dynamics. For example, the localised surface deformations behind an oar is closely linked to the swirling motion on the surface of the vortices in the wake. One might then ask how strong this link is: is it possible from knowledge of the shape of the surface to infer the surface flow? In this paper we shall show that the answer is to a large extent affirmative.

In section 2 we present a simple observation, which to our knowledge has not been stated clearly before: that the stationary flow of an ideal incompressible fluid on a stationary free surface is governed by self-contained dynamical equations that do not involve the flow outside the free surface. These equations are the projection of the Euler equation onto the local surface tangent plane.

To write these equations in a transparent way and connect them to the geometry of the surface, we use a covariant description where the free surface is described as a two-dimensional Riemannian manifold equipped with a metric tensor. With this formalism, which is reviewed in section 3, one can readily write the surface flow equations on an arbitrary smooth free surface. This is done in section 4. The equations can be made to account for surface

tension and velocity-dependent forces, such as the Coriolis acceleration in a non-inertial reference frame.

In section 5, we move on to describe a situation where the flow and surface shape possess invariance under rotations about a fixed axis, a case that has been discussed in Bergmann et al. (2011). In this case the equations simplify a great deal and it is straightforward to find solutions. The types of solutions demonstrate a crucial property of the surface flow equations: that they may be singular on lines separating regions with different behaviour of the flow. The ramifications for general surface flows with rotational invariance is discussed. We next study flows in which the circular symmetry is broken, and as an example we look at the perturbation expansion for a line vortex on a slightly asymmetric surface. We obtain expressions for the streamlines and discuss the conditions for the absence of drift.

In section 6 we show that the surface flow equations can be interpreted as a dynamical system, where particles of the dynamical system move along the characteristics for the field equations. With no external forcing (like gravity) the orbits are geodesics corresponding to the given surface deformation. We give general expressions for the Lagrangian and the Hamiltonian controlling the dynamics, and we relate the Beronoulli integral to the conserved energy along the orbit.

Finally, we discuss the general solubility of the surface flow equations. In the example treated in section 5, we gave explicit formulas for flow velocities and streamlines for a slightly perturbed line vortex. On the other hand, the dynamical orbits introduced in section 6, will, since they are projections from the energy surface of a 4-dimensional phase space, generally intersect, and the existence of a well-defined velocity field on the surface thus depends crucially on the structure of the domain and the boundary conditions imposed on it. As an example, we treat an anisotropic quadratic surface elevation and show that the perturbation expansion breaks down.

2. Decoupling of the free surface Euler equations from the bulk flow

Consider the stationary flow of an inviscid, incompressible fluid of constant density ρ_0. The velocity vector is denoted by $\mathbf{v}$ and the *vorticity* vector is $\boldsymbol{\omega} = \nabla \times \mathbf{v}$. Conservation of momentum for time-independent flow is expressed by the Euler equation,

$$(\mathbf{v} \cdot \nabla)\mathbf{v} = -\frac{1}{\rho_0}\nabla p + \mathbf{f}. \tag{2.1}$$

External body forces are represented by the acceleration vector $\mathbf{f}$. Note that p is the pressure divided by the constant fluid density.

On a smooth free surface, inviscid flow governed by (2.1) is subject to: 1) *the kinematic boundary condition,* that $\mathbf{v} \cdot \mathbf{n} = 0$, where $\mathbf{n}$ is a any normal vector to the surface, and 2) *the dynamic boundary condition,* that the pressure (neglecting an immaterial constant term) is $p = 2\gamma H$. This is the Young-Laplace pressure associated with constant surface tension γ on a surface of mean curvature H, which is well-defined at every point on the free surface and differentiable in terms of any smooth surface parametrization.

We use the identity $(\mathbf{v} \cdot \nabla)\mathbf{v} = \nabla\|\mathbf{v}\|^2/2 + \boldsymbol{\omega} \times \mathbf{v}$ and project (2.1) along

a tangent vector $\mathbf{t}$ to the surface by taking the dot product of $\mathbf{t}$ and the vector quantities on either side. The resulting equation,valid in the surface is

$$(\mathbf{t}\cdot\nabla)\frac{\|\mathbf{v}\|^2}{2}+\mathbf{t}\cdot(\boldsymbol{\omega}\times\mathbf{v})=-2\frac{\gamma}{\rho_0}(\mathbf{t}\cdot\nabla)H+\mathbf{t}\cdot\mathbf{f}. \tag{2.2}$$

Aside from the triple product term $\mathbf{t}\cdot(\boldsymbol{\omega}\times\mathbf{v})$, all the terms in (2.2) are explicitly in the tangent plane since $\mathbf{t}\cdot\nabla$ is the derivative along a tangent vector in the surface, and since the kinematic boundary condition ensures that the normal component of $\mathbf{v}$ vanishes in the surface. To show that the triple product is also in the tangent plane, we use the invariance of a triple product under cyclic permutations of the factors: $\mathbf{t}\cdot(\boldsymbol{\omega}\times\mathbf{v})=\boldsymbol{\omega}\cdot(\mathbf{v}\times\mathbf{t})$. Now, $\mathbf{v}\times\mathbf{t}$ (a cross product of tangent vectors) is clearly normal to the surface, so (2.2) refers only to the normal component of the vorticity field, which in turn is defined by velocity gradients only in the tangent plane.

We have then achieved a decoupling between the surface flow and the bulk flow in the sense that (2.2) involves only velocity components and derivatives *in* the surface. Note that the continuity equation, which involves the normal derivative of the normal component of $\mathbf{v}$ is left indeterminate, but since the pressure has disappeared as a variable, the surface flow equations, being basically two coupled equations for two independent surface velocity components, are sufficient for a solution. This will be discussed in greater detail later. Note at this point, that knowledge of the surface flow allows the determination of the normal derivative $\partial v_n/\partial n$ of the normal velocity by the continuity equation,

$$\nabla\cdot\mathbf{v}=\frac{\partial v_n}{\partial n}+\nabla_s\cdot\mathbf{v}=0, \tag{2.3}$$

where $\nabla_s\cdot\mathbf{v}$ is the divergence in the tangent plane.

Let us briefly discuss the case of a viscous flow. The dynamical boundary condition requires the viscous stress tensor to vanish on the free surface. However, the divergence of the stress tensor, which gives the viscous force density, needs not vanish. The uncoupling cannot take place for the viscous Navier-Stokes equation as one can immediately realize by considering the Poiseuille flow of a uniform film of liquid flowing steadily down an inclined plate. At the free surface, the force of gravity is balanced by the viscous force, a necessary condition for steady flow. In many cases, however, it is useful to approximate the dynamics of a given flow by neglecting viscous stresses. This would require that the Reynolds number be small, i.e. that the viscous force term is small compared to the terms included in (2.1). Even though the flow of a real flow is often dramatically different from a solution to the Euler equation, this difference is typically localized to strong vorticity in boundary layers near solid boundaries, and regions where such boundary layer vorticity is advected by the flow. For extended regions of the fluid, viscosity plays a negligible role in the local dynamics.

Note that we could easily have considered a time dependent velocity field. The inclusion of the term $\partial\mathbf{v}/\partial t$ in (2.2) would still allow us to proceed with the projection to the tangent plane. We have not pursued this further here since in applications this would typically imply that the surface shape is time dependent too, and this would introduce severe complications.

3. Covariant formulation of the 3D Euler equations

In the previous section we showed that the Euler equation, when projected along the free surface, decouples from the bulk flow. This was done locally, with reference to vectors defined in the tangent plane associated with a specific point on the free surface. Now, in order to assemble this point-wise information into a useful set of partial differential equations we shall proceed to develop a framework based on tensor notation and the description of the free surface as a two-dimensional Riemannian manifold. In many cases, the dynamical equations can be derived and analyzed without reference to the physical 3D space, into which this manifold is embedded. However, inclusion of magnetic or Coriolis forces, and the effect of surface tension, requires us to refer to the details of the embedding.

Conventionally, the equations of fluid mechanics are written in terms of orthogonal coordinates. When dealing with the flow on a (generally curved) surface, it is generally practical to use non-orthogonal coordinates. Even though orthogonal coordinate systems do exist for any two-dimensional smooth manifold, cf. Stoker (1969), their relation to typical laboratory coordinates can be complicated, and their very definition may involve the solution of differential equations. Riemannian geometry, on the other hand, provides a straightforward procedure for describing the flow on any smooth surface using non-orthogonal coordinates. For example, a wavy surface given in Cartesian coordinates $(x, y, h(x, y))$, where h is the surface height, can immediately be described as a manifold parameterized by the coordinates (x, y), which are non-orthogonal when the surface has a height gradient at an angle to the coordinate axes. In the following, we shall develop a procedure for writing the projected Euler equations governing free surface flows on such (and more general) surfaces. For a phycisists introduction to Riemannian geometry, cf. Carroll (2003). We start by writing the full 3-dimensional stationary Euler equation in covariant form. Covariance means that the equations keep their meaning when the coordinate system is transformed. The essential point is that we write our equations in terms of tensors, defined as objects that transform according to specific rules, implying covariance. If the equations hold in one coordinate system, they will hold in another, due to the tensor property. So we need simply write the Euler equation in tensor form, such that it reduces to the well-known expression in orthogonal coordinates.

First we introduce an orthogonal "laboratory" coordinate system $y^\alpha = (y^1, y^2, y^3)$. The corresponding metric tensor is $\delta_{\alpha\beta}$, the Kronecker delta. Let the fluid domain be described by a set of coordinates x^μ, $\mu = 1, 2, 3$, given a transformation

$$x^\mu \to y^\alpha(x^\mu), \tag{3.1}$$

and a metric tensor

$$g_{\mu\nu} = \frac{\partial y^\alpha}{\partial x^\mu}\frac{\partial y^\beta}{\partial x^\nu}\delta_{\alpha\beta}. \tag{3.2}$$

By convention, summation over repeated indices is implied. In the following, we shall use Greek letters to denote indices over 3D space and Latin letters to denote indices over the 2D manifold describing the free surface. The inverse metric $g^{\mu\nu}$ is defined as the matrix inverse of $g_{\mu\nu}$, i.e. $g_{\mu\lambda}g^{\lambda\nu} = \delta^\nu_\mu$.

A *vector* is a quantity with one upper index, e.g. the fluid flow velocity $V^\mu = \mathrm{d}x^\mu/\mathrm{d}t$, where x^μ are the coordinates of a fluid particle. A *dual vector* is a quantity with a lower indix, e.g. the gradient $\partial_\nu \Phi \equiv \partial\Phi/\partial x^\nu$. Both are tensors and transform accordingly, cf. Carroll (2003). The rules of tensor manipulation ensure that contractions, e.g. $a_\mu \equiv g_{\mu\nu}V^\nu$, or products, e.g. $b^\mu{}_\nu \equiv V^\mu \partial_\nu \Phi$, are tensors. We can raise and lower indices by the metric tensor, i.e. we can define a dual velocity vector by $V_\mu \equiv g_{\mu\nu}V^\nu$ or a vector gradient by $\partial^\mu \Phi \equiv g^{\mu\nu}\partial_\nu \Phi$. The physical velocity vector $\mathbf{v}$ is given in terms of V^μ by $\mathbf{v} = \mathbf{e}_\mu V^\mu$, where $\mathbf{e}_\mu = \partial \mathbf{y}/\partial x^\mu$ are the *dual basis vectors*. Note that $\mathbf{e}_\mu$ need not be either unit vectors nor mutually orthogonal.

The Euler equation in covariant form reads

$$V^\nu \nabla_\nu V^\mu = -g^{\mu\nu}\frac{\partial \Phi}{\partial x^\nu} + f^\mu. \tag{3.3}$$

The left-hand side of (3.3) is the covariant expression of the conventional advective derivative and contains the covariant derivative

$$\nabla_\nu V^\mu = \frac{\partial V^\mu}{\partial x^\nu} + \Gamma^\mu_{\nu\lambda} V^\lambda. \tag{3.4}$$

The last term of (3.4) is a curvature term that accounts for the change of coordinate directions over space. They contain the Christoffel connection coefficients, defined in terms of the metric by

$$\Gamma^\lambda_{\mu\nu}[g_{\alpha\beta}] = \frac{1}{2}g^{\lambda\sigma}\left(\frac{\partial g_{\nu\sigma}}{\partial x^\mu} + \frac{\partial g_{\mu\sigma}}{\partial x^\nu} - \frac{\partial g_{\mu\nu}}{\partial x^\sigma}\right), \tag{3.5}$$

where we have explicitly written the dependence on the metric $g_{\alpha\beta}$. The connection coefficients are not tensors, but the covariant derivative defined by (3.4) is. On the right hand side of (3.3) we have the scalar potential field Φ and the applied force f^μ. We can define Φ so as to include pressure (p/ρ_0), gravity forces and possibly a centrifugal force, and on the free surface, the effect of surface tension, which would correspond to Φ containing a term proportional to the surface mean curvature. The covariant formulation of the Euler and Navier-Stokes equations has been discussed earlier, e.g. by Ilin (1991).

To see that (3.3) are indeed the stationary Euler equations, we inspect their form in Cartesian coordinates, where $g_{\mu\nu} = \delta_{\mu\nu}$. Then $\Gamma^\lambda_{\mu\nu} = 0$, and the equations read $(\mathbf{v}\cdot\nabla)\mathbf{v} = -\nabla\Phi + \mathbf{f}$, which we recognize.

4. Covariant formulation of the surface flow equations

In order to project (3.3) onto the free surface, we shall now introduce a particular set of surface-adapted coordinates. We denote the free surface by $\mathcal{S}$. We assume that $\mathcal{S}$ is described by a smooth regular parameterized surface, i.e. a map $f_0 : x^i \to y^\alpha$

$$x^i \to y^\alpha \equiv f_0^\alpha(x^i). \tag{4.1}$$

Here and below we use Greek letters to denote indices over 3D space, so $x^\mu = (x^1, x^2, x^3)$, and Roman letters for indices over $\mathcal{S}$, so $x^i = (x^1, x^2)$. The regularity of the parameterization (4.1) means that at any point, the

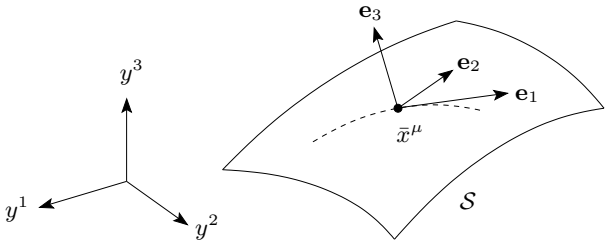

FIGURE 1. Sketch of the coordinates. y^α are the Cartesian laboratory coordinates. x^μ are non-orthogonal coordinates attached to the free surface $\mathcal{S}$ and defined by the map $y^\alpha = f^\alpha(x^\mu)$ given in (4.3). The basis dual vectors $\mathbf{e}_i$, (4.2), associated to a point $x^\mu = \bar{x}^\mu$ define the local coordinate directions, in the sense that $f^\alpha(\bar{x}^\mu + \mathrm{d}x^\mu) = f^\alpha(\bar{x}_0) + \mathrm{d}x^\mu \mathbf{e}_\mu(x_0^\mu)$. The dashed line tangent to $\mathbf{e}_1$ is obtained by varying x^1 while keeping x^2 and x^3 fixed. (4.3) defines a valid coordinate system close the $\mathcal{S}$, i.e. for small values of x^3.

vectors $\partial f_0^\alpha/\partial x^1$ and $\partial f_0^\alpha/\partial x^2$ are linearly independent, and so they span the local tangent plane. The smoothness condition means that the tangent plane varies smoothly with (x^1, x^2). We introduce the dual vectors

$$\mathbf{e}_1(x^i) = \frac{\partial f_0^\alpha}{\partial x^1}, \quad \mathbf{e}_2(x^i) = \frac{\partial f_0^\alpha}{\partial x^2}, \quad \mathbf{e}_3(x^i) = \frac{\mathbf{e}_1 \times \mathbf{e}_2}{\|\mathbf{e}_1 \times \mathbf{e}_2\|}, \tag{4.2}$$

all of which are defined on $\mathcal{S}$, and the map $f : x^\mu \to y^\alpha$,

$$f^\alpha(x^1, x^2, x^3) = f_0^\alpha(x^i) + x^3 \mathbf{e}_3(x^i). \tag{4.3}$$

Due to (4.2) and the regularity of (4.1), f is a smooth map at any point x^i in $\mathcal{S}$, with a nonsingular Jacobian matrix, i.e. $|\partial y^\alpha/\partial x^\mu| \neq 0$. So by the Inverse Function Theorem, the inverse map $f^{-1} : y^\alpha \to x^\mu$ exists in a small neighbourhood of space around any point $y^\alpha(x^i)$ in $\mathcal{S}$. So f defined by (4.3) is a smooth bijective map from an open set in $\mathbb{R}^3$ containing the plane $x^3 = 0$ to an open set of the physical space containing the free surface $\mathcal{S}$. In other words, x^μ together with (4.3) gives a valid coordinate system on space near the free surface $\mathcal{S}$. (4.2) are the corresponding dual basis vectors. Note that this argument extends directly to the case where $\mathcal{S}$ is described by two or more overlapping charts, whose overlap must satisfy certain conditions for $\mathcal{S}$ to be a manifold. These properties carry over the 3D manifold to linear order in x^3.

We move on to compute the metric from (4.3). We have $\partial y^\alpha/\partial x^i = \mathbf{e}_i + x^3 \partial \mathbf{e}_3/\partial x^i$ and $\partial y^\alpha/\partial x^3 = \mathbf{e}_3$. To first order in x^3, the metric tensor (3.2) is

$$g_{\mu\nu} = \mathbf{e}_\mu \cdot \mathbf{e}_\nu + x^3 \left(\mathbf{e}_\mu \cdot \frac{\partial \mathbf{e}_3}{\partial x^\nu} + \mathbf{e}_\nu \cdot \frac{\partial \mathbf{e}_3}{\partial x^\mu} \right). \tag{4.4}$$

Now, (4.4) allows us to compute the first derivatives of the metric on $\mathcal{S}$ and so the Christoffel symbols in (3.5).

The property $\mathbf{e}_i \cdot \mathbf{e}_3 = 0$ means that the metric (4.4) takes a special form on $\mathcal{S}$, essentially decomposing the part pertaining to x^1, x^2:

$$g_{\mu\nu} = \begin{pmatrix} \begin{bmatrix} g_{ij} \end{bmatrix} & \begin{matrix} 0 \\ 0 \end{matrix} \\ \begin{matrix} 0 & 0 \end{matrix} & 1 \end{pmatrix}, \tag{4.5}$$

where g_{ij} is the 2D metric tensor of the surface submanifold:

$$g_{ij} = \frac{\partial f_0^\alpha}{\partial x^i}\frac{\partial f_0^\beta}{\partial x^j}\delta_{\alpha\beta}, \quad i,j = 1,2. \tag{4.6}$$

where f_0 is defined in (4.1).

Similarly, we introduce submanifold connection coefficients $\Gamma^i_{jk}[g_{lm}]$ by restricting the summation indices in (3.5) to 1,2. We note that these new connection coefficients are identical to the corresponding ones defined from the full metric $\Gamma^i_{jk}[g_{lm}] = \Gamma^i_{jk}[g_{\mu\nu}]$, but we want to stress that they can be computed without reference to the x^3 coordinate. The block form of $g_{\mu\nu}$ in (4.5) implies that the inverse metric $g^{\mu\nu}$ takes a similar block form, with g_{ij} in (4.5) replaced by its inverse, g^{ij}.

We shall now show that, in accordance with section 2, the equations of (3.3) for $\mu = 1,2$, refer only to the physical fields directly on the free surface, and furthermore, that one can determine the coordinate form of these equations without bothering to even define the third coordinate, x^3. We assume for now that the force and potential fields f^i and Φ are known on the surface as functions of the parametrizing coordinates x^i.

The kinematic boundary condition, $\mathbf{v}\cdot\mathbf{n} = 0$, means that the physical velocity vector $\mathbf{v}$ lies in the plane spanned by $\mathbf{e}_1, \mathbf{e}_2$. Since the linearly independent dual basis vectors $\mathbf{e}_\mu$ admit a unique linear combination forming $\mathbf{v}$, this implies $V^3 = 0$.

Looking at the terms of (3.3) with $\mu = 1,2$, we note that the partial derivatives $\partial/\partial x^i$ refer only to surface quantities. (4.5) implies $g^{i\nu}\partial\Phi/\partial x^\nu = g^{ij}\partial\Phi/\partial x^j$ so the potential term depends only on the potential defined on the free surface. As for the convective derivative $V^\nu\nabla_\nu V^i = V^j\nabla_j V^i$, it contains only surface-directed velocity derivatives $\partial V^i/\partial x^j$ and the connection coefficients Γ^i_{jk}, which may be computed directly from the surface metric (4.6).

Let us return to the question of the potential and force fields, which must be defined using the full map $x^i \to y^\alpha$. A crucial feature of the surface equations is, in contrast to the 3D Euler equations (3.3), that the pressure drops out of the potential, since it is constant on the surface, except for the Laplace pressure due to surface tension. We thus assume that the potential has the form

$$\Phi = \phi(y^\alpha) + 2\gamma H, \tag{4.7}$$

where H is the surface mean curvature defined on the surface. H is positive when the surface curves in the direction of the normal vector $\mathbf{e}_3$. Physically, this corresponds to $\mathbf{e}_3$ pointing out of the fluid. For example $y^\alpha = (x^1, x^2, h(x^1, x^2))$ corresponds to the typical situation where the fluid is below the interface.

The mean curvature is given by

$$H(x^i) = -\frac{1}{2}g^{\mu\nu}\nabla_\nu n_\mu = -\frac{1}{4}g^{\mu\nu}\frac{\partial g_{\mu\nu}}{\partial x^3}, \tag{4.8}$$

where $n_\mu = \delta^3_\mu$ is the dual normal vector field. In (4.8), we have used the

extrinsic curvature tensor $\nabla_\mu n_\nu$ associated with the surface, a generalization of the second fundamental form of the surface, cf. Carroll (2003). The tensor $g^{\mu\lambda}\nabla_\lambda n_\nu$ generalizes the Weingarten matrix, the trace of which is associated to the mean curvature, cf. do Carmo (1976). Note that H is an extrinsic quantity, i.e. it depends on the metric outside the free surface by the tensor $\partial g_{\mu\nu}/\partial x^3$ given in (4.4). The definitions in (4.1-4.2,4.5) allow H to be computed as a function of x^i.

Now, using again (4.1), we can define the potential (4.7) as a function of the surface coordinates by

$$\Phi(x^i) = \phi(y^\alpha(x^i)) + 2\gamma H(x^i), \tag{4.9}$$

Similarly, we compute the Coriolis acceleration term, f^μ in (3.3). The cross product $\mathbf{A} = \mathbf{B} \times \mathbf{C}$ in terms of covariant coordinates is

$$A^\mu = g^{\mu\nu}\sqrt{g}\,\varepsilon_{\nu\rho\sigma}B^\rho C^\sigma, \tag{4.10}$$

where $\sqrt{g} = |g_{\mu\nu}|^{1/2}$ is the determinant of the Jacobian matrix $\partial y^\alpha/\partial x^\mu$, and $\varepsilon_{\nu\rho\sigma}$ is the Levi-Civita symbol, equal to the sign of the permutation of the numbers $\nu\rho\sigma$ and zero if any number is repeated. (4.10) can be derived using elementary techniques by considering a linear invertible map to Cartesian coordinates and comparing to the well-known formula. For a more conventional differential geometry derivation in terms of dyadics, cf. Lebedev et al. (2010). Note that A^μ is a pseudovector, i.e. it switches sign in a left-handed coordinate system. Using (4.5) and the kinematic boundary condition, we see that the components f^i of (4.10) applied to $\mathbf{f} = -2\boldsymbol{\Omega} \times \mathbf{v}$ refer only to the third component $\Omega^3 = \mathbf{e}_3 \cdot \boldsymbol{\Omega}$ of $\boldsymbol{\Omega}$, and we have

$$f^i(x^k) = 2|g_{ij}|^{1/2}\,\Omega^3(g^{i1}V^2 - g^{i2}V^1). \tag{4.11}$$

With all this in place, we are ready to define the flow equations in terms of the manifold coordinates x^i.

In summary, the ideal flow on a stationary free surface parametrized by $(x^1, x^2) \to (y^1, y^2, y^3)$ is governed by the momentum balance equations

$$V^j\nabla_j V^i = \\ V^j\frac{\partial V^i}{\partial x^j} + \Gamma^i_{jk}V^jV^k = -g^{ij}\frac{\partial \Phi}{\partial x^j} + f^i, \tag{4.12}$$

where $i, j = 1, 2$, and the metric is defined by (4.6). The left hand side can be computed from the metric alone, using (3.4) and $\Gamma^i_{jk}[g_{lm}]$ defined by (3.5). The terms on the right hand side depend on the embedding $x^i \to y^\alpha$ and the dual basis (4.2). Expressions for the potential $\Phi(x^i)$ and the Coriolis acceleration $f^i(x^j)$ and are given in (4.9) and (4.11). In appendix A we give the coordinate expression for (4.12) in two important cases, where the horizontal position is described by the coordinates (x^1, x^2), which are either Cartesian or polar, and the vertical height is given by $y^3 = h(x^1, x^2)$.

We shall later see that (4.12) has a first integral generalizing the Bernoulli field, cf. (6.7a) below.

As for the possibility of specifying the normal derivative $\partial v_n/\partial n$ of the

normal velocity by the continuity equation, cf. chapter 2, we note that the covariant formulation of the continuity equation (2.3) is

$$\nabla_\mu V^\mu = 0. \tag{4.13}$$

On the free surface, where $V^3 = 0$, the only quantities referring fields outside the surface (4.13) are $\partial V^3/\partial x^3$ and $\Gamma^3_{3i} = 0$, where the last equality follows from the coordinate definition (4.4). So we are left with the following expression for the normal derivative

$$\frac{\partial v_n}{\partial n} = \frac{\partial V^3}{\partial x^3} = -\frac{\partial V^i}{\partial x^i} - \Gamma^i_{ij} V^j, \tag{4.14}$$

where the last term is the curvature correction to (2.3).

5. Solutions to the surface flow equations in symmetric and nearly symmetric situations

We have seen how to write the surface flow equations (4.12) on a general curved surface with a general potential field, but to solve these equations, or even write them in coordinate form, is not an easy task. We shall therefore start out by looking at a couple of simple special cases.

First we consider the special case when both the free surface height and the flow field are invariant under rotations about the y^3 axis. In this case, (4.12) reduces to a simple set of two ordinary differential equations, and the solution is straightforward. The free surface is parameterized by the coordinates $(x^1, x^2) = (\rho, \theta)$. The corresponding (contravariant) velocity vector components are $(V^1, V^2) \equiv (U, V)$. Note that the vector component V has the dimensions of an angular velocity. The position in space is given in terms of Cartesian coordinates y^α by

$$(y^1, y^2, y^3) = (\rho\cos\theta, \rho\sin\theta, h(\rho)). \tag{5.1}$$

The potential field is $\Phi = \Phi(\rho)$. We do not include the possibility of a rotating reference frame at this stage, since any steady rotation about the symmetry axis may be included in the flow field. Now, (4.12) written for polar base coordinates, cf. (A 10), yields

$$UU_\rho + \frac{1}{1+h_\rho^2}\Big(h_\rho h_{\rho\rho} U^2 - \rho V^2\Big) = -\frac{1}{1+h_\rho^2}\Phi_\rho, \tag{5.2a}$$

$$UV_\rho + 2\frac{1}{\rho}UV = 0, \tag{5.2b}$$

for the ρ and θ directions, respectively. We use a subscript to denote differentiation, i.e. $U_\rho = \mathrm{d}U/\mathrm{d}\rho$. We can make sense of (5.2) by introducing the "physical" velocity components u, v, along the dual basis $\mathbf{e}_\rho$, $\mathbf{e}_\theta$, so that the velocity vector is $\mathbf{v} = u\mathbf{e}_\rho/\|\mathbf{e}_\rho\| + v\mathbf{e}_\theta/\|\mathbf{e}_\theta\|$. In the symmetric situation, the coordinates are orthogonal, $\mathbf{e}_\rho \cdot \mathbf{e}_\theta = 0$, so we have

$$u = \|\mathbf{e}_\rho\| U = \sqrt{g_{\rho\rho}}\, U = \sqrt{1+h_\rho^2}\, U, \tag{5.3a}$$

$$v = \|\mathbf{e}_\theta\| V = \sqrt{g_{\theta\theta}}\, V = \rho V, \tag{5.3b}$$

in terms of which (5.2) are equivalent to

$$\frac{\mathrm{d}}{\mathrm{d}\rho}\left(\frac{u^2}{2}+\Phi\right)-\frac{v^2}{\rho}=0, \tag{5.4a}$$

$$\frac{u}{\rho^2}\frac{\mathrm{d}}{\mathrm{d}\rho}(\rho v)=0. \tag{5.4b}$$

An equivalent set of equations was derived in Bergmann et al. (2011) using a more pedestrian approach in line with our section 2.

We will now briefly reiterate some analysis of Bergmann et al. (2011) and move on to some general considerations about the possible solutions to (5.4). First we note that (5.4*b*) is singular when $u = 0$. Hence, the solutions to (5.4) fall in two categories:

a) A regime where $u = 0$, so (5.4*b*) is satisfied independently of v, and (5.4*a*) reduces to

$$\frac{v^2}{\rho}=\Phi_\rho. \tag{5.5}$$

If the function $\Phi(\rho)$ is known, (5.5) directly expresses the possible forms $v(\rho)$. If on the other hand $v(\rho)$ is known, an expression for $\Phi(\rho)$ can easily be established by integrating (5.5).

b) A regime where $u \neq 0$, and (5.4*b*) leads to

$$v=\frac{\Gamma}{\rho}, \tag{5.6a}$$

where Γ is a constant, and the circulation along a streamline ρ =constant is $2\pi\Gamma$. Using (5.6*a*), (5.4*a*) integrates to

$$\frac{1}{2}(u^2+v^2)+\Phi=\text{constant}, \tag{5.6b}$$

the well-known Bernoulli equation connecting points along the same streamline in Euler flows, cf. (6.7*a*) below. This was to be expected, because in the symmetric case any finite region with $u \neq 0$ is connected by streamlines.

The splitting of the solutions to (5.4) presented above can be interpreted as follows. In regime *a*, different radii are not connected by streamlines, and (5.4*b*) is exhausted by $u = 0$. That condition, however, allows us to directly solve (5.4*a*) either in terms of the velocity field or the potential field. In regime *b*, different radii *are* connected by streamlines, and (5.4) lead to conditions for the conservation of angular momentum (5.6*a*) and energy (5.6*b*).

Similar considerations were used in Bergmann et al. (2011) to give the surface flow field based on a measurement of the surface profile, a result confirmed by a direct measurement of the velocities. Furthermore, the symmetric flow equations were used to infer information about the surface elevation from requiring continuity of the flow field, cf. Bergmann et al. (2011).

5.1. *Nearly symmetric flows*

We now consider a situation where the free surface and the potential are nearly symmetric under rotations. In particular, we look at perturbations of

the flow problem discussed in the preceding section. We do the computation in a rotating reference frame to account for the possibility of an assymmetric disturbance that rotates as a rigid body. Examples of such flows are bathtub vortices disturbed by waves traveling in the azimuthal direction, or other symmetry-breaking flows such as the rotating polygons discussed by Bergmann et al. (2011).

One can proceed from (A 10) with the substitutions

$$h \to H(\rho) + \varepsilon h(\rho, \theta), \tag{5.7a}$$

$$\Phi \to \Phi(\rho) + \varepsilon \phi(\rho, \theta), \tag{5.7b}$$

$$U \to U(\rho) + \varepsilon u(\rho, \theta) + \mathcal{O}(\varepsilon^2), \tag{5.7c}$$

$$V \to V(\rho) + \varepsilon v(\rho, \theta) + \mathcal{O}(\varepsilon^2), \tag{5.7d}$$

and expand (A 10) to first order in ε. Note that the validity of the expansion (5.7) rests upon the unperturbed velocity being large compared to the perturbation, so we can expect problems if U and V vanish in some region.

For simplicity, we assume $U = 0$. The reference frame rotates in the positive θ direction at the angular velocity Ω. We take $\Phi = g_0 h - \frac{1}{2}\Omega^2 \rho^2$, where g_0 is the gravity acceleration constant.

The zeroth order equation of (A 10) in the ρ direction gives

$$(V + \Omega)^2 = \frac{g_0 H'}{\rho}, \tag{5.8}$$

which can be seen by substituting $U \to 0$ and $V \to V + \Omega$ in (5.2a).

Now, using (5.8), the first order part of (A 10) is

$$V \frac{\partial u}{\partial \theta} - 2\rho \frac{V + \Omega}{1 + H'^2} v = -\frac{1}{1 + H'^2} \left[V^2 H' \frac{\partial^2 h}{\partial \theta^2} + g_0 \frac{\partial h}{\partial \rho} \right], \tag{5.9a}$$

$$\frac{2V + \rho V' + 2\Omega}{\rho} u + V \frac{\partial v}{\partial \theta} = -\frac{g_0}{\rho^2} \frac{\partial h}{\partial \theta}, \tag{5.9b}$$

a set of linear partial differential equations in u and v. We Fourier expand the perturbation and the first order velocities, i.e. $h(\rho, \theta) = \mathrm{Re}[\sum_n h_n(\rho) e^{in\theta}]$, $u(\rho, \theta) = \mathrm{Re}[\sum_n u_n(\rho) e^{in\theta}]$ and $v(\rho, \theta) = \mathrm{Re}[\sum_n v_n(\rho) e^{in\theta}]$. The Fourier coefficients are in general complex functions of ρ, allowing the phase of the perturbation to depend on ρ. The linearity of (5.9) ensures that the terms pertaining to different n are independent. On a Fourier component of wavenumber n, the derivative $\partial/\partial\theta$ simply acts to multiply by in, so (5.9) yields a linear system of algebraic equations for u_n and v_n in terms of h_n and h_n', which we can easily solve by inverting the coefficient matrix found from the left hand side of (5.9).

As a useful example, we consider a line vortex, with a slight perturbation revolving at the rate Ω. For now, we restrict our attention to the case $\Omega \neq 0$ and take $V = \Gamma/\rho^2 - \Omega$. From (5.8), $H' = \rho V^2 / g_0$. In this case, the coefficient to u in (5.9b) vanishes, so the coefficient matrix associated with (5.9) has the determinant $-n^2 V^2$, which is nonzero except at a particular characteristic radius $\rho = \lambda$ defined below. We now non-dimensionalize all quantities by

the characteristic length λ and time τ,

$$\lambda \equiv \sqrt{\Gamma/\Omega}, \qquad \tau \equiv \Omega^{-1}. \tag{5.10}$$

For example, we rescale ρ to the non-dimensional $\hat{\rho} = \rho/\lambda$ and V to the non-dimensional

$$\hat{V} = V\left(\frac{1}{\tau}\right)^{-1} = \frac{1}{\hat{\rho}^2} - 1. \tag{5.11}$$

By inserting the expressions for V and H' into (5.9) and rescaling, we get expressions for the non-dimensional first order velocities in terms of the non-dimensionalized perturbation and the non-dimensional parameters $\hat{\rho}$ and $\hat{g}_0$. The non-dimensional gravity constant is $\hat{g}_0 = g_0(\lambda/\tau^2)^{-1} = g_0(\lambda\Omega^2)^{-1}$, i.e. the ratio of the magnitudes of the accelerations due to gravity and the centripetal unperturbed flow at the characteristic radius. For the remainder of this section, we shall drop the hats and always refer to non-dimensional quantities. Now, (5.9) yield

$$u_n = i[A_n(\rho)h_n + B_n(\rho)h_n'] \tag{5.12a}$$

$$v_n = C(\rho)h_n, \tag{5.12b}$$

with

$$A_n(\rho) = \frac{1}{(1+g_0^2\rho^6)}\left[\frac{1}{n}\frac{2g_0^3\rho^7}{(1-\rho^2)^2} - ng_0\rho(1-\rho^2)\right], \tag{5.12c}$$

$$B_n(\rho) = \frac{1}{n}\frac{g_0^3\rho^8}{(1-\rho^2)(1+g_0^2\rho^6)}, \tag{5.12d}$$

$$C(\rho) = -\frac{g_0}{1-\rho^2}. \tag{5.12e}$$

The coefficients in (5.12) are shown in figure 2 as functions of ρ. The coefficients are well-defined expect for the characteristic radius $\rho = 1$, where they diverge, cf. (5.12). Because the unperturbed flow velocity vanishes at this radius, the coefficient matrix of (5.9) vanishes, implying that the perturbation expansion (5.7) is ill-defined here. We shall proceed to consider perturbations in regions for $\rho \neq 1$, concentrating on the region $\rho < 1$, where the flow speed exceeds the rotation speed of the perturbation. The coefficient $A_n(\rho)$ changes sign once in the interval $0 < \rho < 1$, at a radius which we designate ρ_*, the single positive real root of

$$g_0^2\rho_*^6 - n^2(1-\rho_*^2)^3. \tag{5.13}$$

This gives rise to some interesting behaviour of the perturbed streamlines, as we shall see below, cf. figure 3.

Pausing briefly to comment on stationary perturbations with $\Omega = 0$, we note that this case can be accessed by changing to another scaling, by the length $\Gamma^{2/3}g_0^{-1/3}$ and time $\Gamma^{1/3}g_0^{-2/3}$. The expressions for u_n and v_n are then obtained by substituting $(1-\rho^2) \to 1$ and $g_0 \to 1$ in (5.12) and (5.13). The qualitative behaviour of the coefficients resemble the interval $0 < \rho < 1$ in

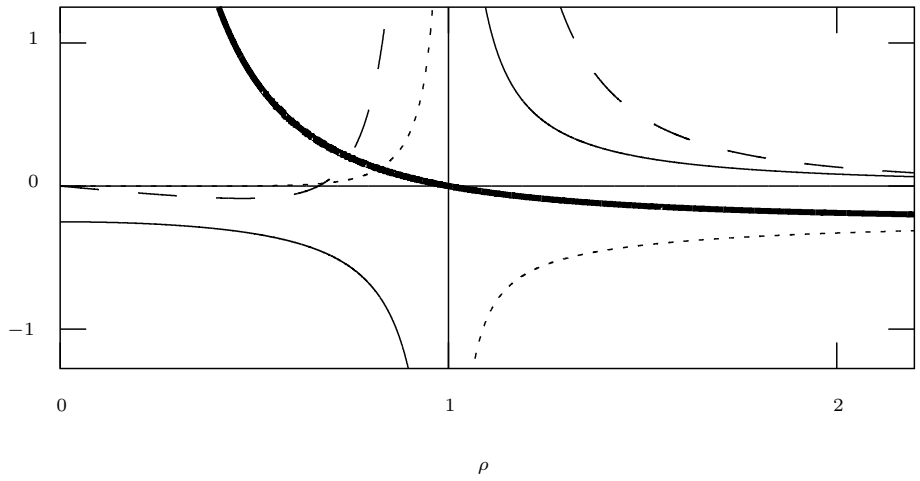

FIGURE 2. The dependence of the coefficients in (5.12) as a function of the nondimensional radius ρ for $g_0 = 1$. The thick black curve shows the zeroth order azimuthal velocity V as a reference, cf. (5.10). Note that V changes sign at the characteristic radius $\rho = 1$. The thin black line is $C(\rho)$. The dashed line is $A_1(\rho)$. Note the sign change at $\rho_* = 1/\sqrt{2}$, cf. (5.13). The dotted line is $B_n(\rho)$. We note that A_n and B_n for different values of n are qualitatively similar to the curves shown, with ρ_* approaching 1 as n increases.

figure 2, in particular the coefficient A_n is negative for $\rho < \rho_*$ and positive for $\rho_* < \rho$. We now turn to the question of the streamlines of the perturbed flow. We consider a perturbation consisting of a single Fourier mode of wavenumber n. To linear order in ε and in terms of nondimensional quantities, the position of a fluid particle is governed by the linear dynamical system

$$\dot{\theta} = V + \varepsilon v, \tag{5.14a}$$

$$\dot{\rho} = \varepsilon u, \tag{5.14b}$$

where a dot indicates the derivative with respect to the non-dimensional time t. By u we mean $\mathrm{Re}[u_n(\rho)e^{in\theta}]$ and similarly for v. In the following, we shall take $u_\rho \equiv \mathrm{Re}[u_n'(\rho)e^{in\theta}]$.

Assuming θ to be a monotonic function of t (valid as long as εv_n is small), we substitute θ for our dependent variable. Dividing (5.14b) by (5.14a), we then get an ordinary differential equation for the streamline,

$$\frac{\mathrm{d}\rho}{\mathrm{d}\theta} = \varepsilon \frac{u(\rho,\theta)}{V(\rho) + \varepsilon v(\rho,\theta)}. \tag{5.15}$$

Now, (5.15) is a strongly nonlinear nonautonomous ordinary differential equation, and we have no hope of solving it exactly. Instead, we expand the solution

$$\rho(\theta) = \rho_0 + \varepsilon\rho_1(\theta) + \varepsilon^2\rho_2(\theta) + \mathcal{O}(\varepsilon^3), \tag{5.16}$$

where ρ_0 is the constant unperturbed radius. Expanding (5.15), we get to

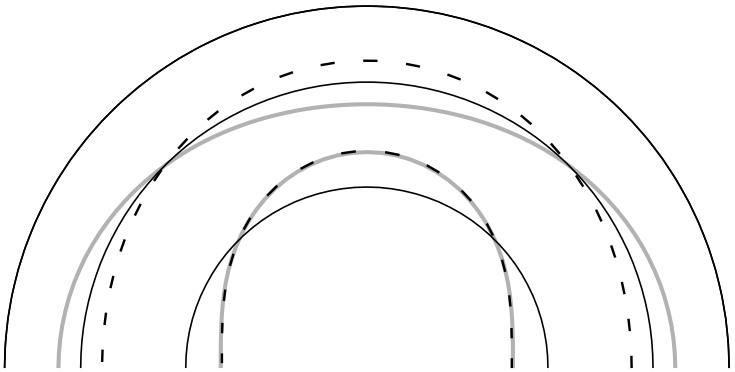

FIGURE 3. Plot of the perturbed streamlines (5.18) for $n = 2$ and $g_0 = 1$. The top half of the unit disc is shown. The bottom half is the mirror image. The characteristic radius $\rho = 1$ is shown as the outer black circle.
Streamlines are shown in grey around two values of ρ_0, and for each a reference circle of radius ρ_0 is shown in black. In both cases we select $h > 0$ for best visibility. We take $h' = 0$. The smallest radius has $\rho_0 = 0.50 < \rho_* = 1/\sqrt{2}$, cf. (5.13), so $A_2 < 0$ and the streamline is deflected in the same direction as the isoheight line by the perturbation, though slightly less. The larger radius has $\rho_0 = 0.79 > \rho_*$, where $A_2 > 0$ and the streamline is deflected away from the isoheight line. The same opposite deflection would be present also for streamlines at $\rho_0 > 1$, cf. the behaviour of A_n in figure 2. The dashed lines show isoheight lines for the same two radii. The isopotential lines (not shown) are close to the isoheight lines, but slightly further deflected from ρ_0.

second order:

$$\varepsilon\frac{\mathrm{d}\rho_1}{\mathrm{d}\theta} + \varepsilon^2\frac{\mathrm{d}\rho_2}{\mathrm{d}\theta} + \ldots = \varepsilon\frac{u}{V} + \varepsilon^2\left(\frac{\rho_1}{V}\frac{\partial u}{\partial\rho} - \frac{u(v+\rho_1 V')}{V^2}\right) + \ldots, \qquad (5.17)$$

where all functions of ρ are evaluated at ρ_0.

We now specify a perturbation. The complex phase of $h_n(\rho_0)$ simply denotes the orientation of the perturbation, so we can take $h_n(\rho_0)$ to be real. For simplicity, and because we typically have $|B_n| < |A_n|$, cf. (5.12) and figure 2, we take $h_n'(\rho_0) = 0$.

We integrate the first order part of (5.17):

$$\rho_1(\theta) = \int_{\theta_i}^{\theta}\mathrm{d}\theta'\frac{u(\rho_0,\theta)}{V(\rho_0)} = -\int_{\theta_i}^{\theta}\mathrm{d}\theta'\,\frac{A_n h_n}{V}\sin n\theta' = \frac{A_n h_n}{nV}\cos n\theta, \qquad (5.18)$$

where we have chosen the starting angle θ_i so as to eliminate a constant from ρ_1. A plot of a few streamlines given by (5.18) is shown in figure 3. For comparison, we show also the isoheight lines around the same ρ_0, found by keeping the nondimensional height $H + \varepsilon h$ fixed to first order in ε. Clearly, the sign of A_n determines the leading deflection of the streamlines induced by the perturbation. In particular, for $\rho < \rho_*$ where $A_n < 0$, cf. (5.13), the deflection ρ_1 has the opposite sign of h_n. This means that the streamlines are deflected in the same sense as the isoheight lines, cf. figure 3. The converse happens for $\rho_* < \rho$.

Could there be *drift* in the solutions to (5.15)? This would mean that ρ would not be an exactly periodic function of θ, but contain a "secular" term allowing a slow change in each revolution. We first consider the case where

h_n' has the same complex phase as h_n. As discussed above, we can take h_n to be real. Then, (5.15) can be written

$$\frac{d\rho}{d\theta} = \frac{A(\rho)\sin n\theta}{B(\rho) + C(\rho)\cos n\theta}, \tag{5.19}$$

where A, B, C are some functions of ρ. In terms of the the variable $x = -\cos n\theta$, this equation becomes

$$\frac{d\rho}{dx} = \frac{1}{n}\frac{A(\rho)}{B(\rho) + C(\rho)x}. \tag{5.20}$$

The variable $x(\theta)$ is monotonically increasing on $[0, \pi/n]$ and monotonically decreasing on $[\pi/n, 2\pi/n]$. Both of these intervals are mapped onto the x-interval $[-1, 1]$.

If we assume that $|C(\rho)| < |B(\rho)|$ for all relevant values of ρ, we can integrate (5.20) with the initial condition $\rho(-1) = \rho_1$ and we shall obtain a value at $x = 1$, say $\rho = \rho_2$. This corresponds to one half-period in θ. In the second half-period, x traverses exactly the same interval $[-1, 1]$, but in the reverse order. This time we start at $\theta = \pi/n$, i.e., at $x = 1$ with the value ρ_2 and move down toward $x = -1$. Since there cannot be more than one solution $\rho(x)$ with $\rho = \rho_2$ at $x = 1$, we are going to exactly reproduce the solution curve from the first half-period and get $\rho = \rho_1$ at $x = -1$. Thus the solution is periodic in θ and there is no drift. In addition, we see that the solution $\rho(\theta)$ will be symmetric under $\theta \to 2\pi - \theta$, since this leaves x invariant. Note that if additional terms containing odd powers of $\sin n\theta$ had been present the above argument would not work because the expression $\sin n\theta = \sqrt{1 - x^2}$ valid for $\theta \in [0, \pi/n]$ would change to $\sin n\theta = -\sqrt{1 - x^2}$ valid for $\theta \in [\pi/n, 2\pi/n]$ and thus the two half-periods would not be identical.

Thus, in the case where h_n' has a different complex phase than h_n, i.e. when the perturbation has a ρ-dependent orientation (for example describing a spiral), we do obtain a drift. Keeping h_n real, a finite h_n' will introduce a term $-\mathrm{Im}[(h_n')\sin n\theta]$ in (5.18). When multiplied by $u_\rho - V'/V$ in (5.15), which also contain a sine part, this term indeed gives rise to a drift of order ε^2. The magnitude and direction of the drift depends on both h_n' and h_n''.

6. The surface flow equations as a dynamical system

We now discuss the possibility of solving the surface flow equations (4.12) and the difficulties that may arise. Unlike the ordinary Euler flow equation, (4.12) form a closed system, with no need for a continuity equation relating to either a condition of incompressibility or knowledge of the pressure field response to fluid compression, e.g. by an equation of state.

For a particle, whose position on the surface x^i and velocity V^i are functions of the time t, (4.12) can be viewed as a dynamical system, since by the chain rule

$$\dot{x}^i \equiv \frac{\mathrm{d}x^i}{\mathrm{d}t} = \frac{\partial V^i}{\partial t} + V^j\frac{\partial V^i}{\partial x^j}, \tag{6.1}$$

and V^i does not depend explicitly on time, i.e. $\partial V^i/\partial t = 0$. So (4.12) implies

that on the streamlines, the motion is governed by the two degree-of-freedom dynamical system,

$$\dot{V}^i = -\Gamma^i_{jk} V^j V^k - g^{ij} \frac{\partial \Phi}{\partial x^j} + f^i, \tag{6.2a}$$

$$\dot{x}^i = V^i. \tag{6.2b}$$

The dynamical system (6.2) is fundamentally different from the field equation (4.12). Given a solution to (4.12), i.e. a field $V^i(x^j)$, we could solve the two-dimensional ODE

$$\dot{x}^i = V^i(x^j), \tag{6.3}$$

where the unique velocity at a given point implies that there is a unique streamline passing through the point. On the contrary, (6.2) is a two degree of freedom Hamiltonian system (a 4D ODE), which has a much richer dynamics than (6.3), and it can for example have chaotic solutions. The trajectories $x^i = x^i(t)$ to (6.2) may intersect each other or even themselves, in violation of the condition that each point specifies a unique velocity. So it is not straightforward to construct solutions to (4.12) from (6.2), and in some cases it is even impossible. We shall return to this discussion below, in section 6.2.

Note that (6.2) corresponds to the Lagrangian

$$L = \frac{1}{2} V_j V^j + V_j A^j - \Phi \tag{6.4}$$

The field $A^j = A^j(x^i)$ is analogous to the electromagnetic vector potential. Since the rotation vector is defined as a fixed direction in physical space, we must refer to the laboratory coordinates $y^{\alpha'}$ defined just before (3.1). Here we indicate these coordinates by primed indices. In $y^{\alpha'}$ coordinates, the vector potential is represented by the physical vector $\mathbf{A} = \mathbf{\Omega} \times \mathbf{y}$, whose components are $A^{\alpha'}$. A^α is obtained through the vector transformation rule $A^\alpha = A^{\alpha'} \partial x^\alpha / \partial y^{\alpha'}$, where $\partial x^\alpha / \partial y^{\alpha'}$ can be found by inverting $\partial y^{\alpha'} / \partial x^\alpha$ given in (4.3). The Coriolis acceleration vector is related to A_j by

$$f^i = g^{ik} V^j \left(\frac{\partial A_j}{\partial x^k} - \frac{\partial A_k}{\partial x^j} \right). \tag{6.5}$$

The Lagrangian, (6.4), corresponds to the generalized momenta

$$p_i \equiv \frac{\partial L}{\partial V^i} = V_i + A_i, \tag{6.6}$$

and the Hamiltonian

$$\begin{aligned} H &= p_j V^j - L \\ &= \frac{1}{2} V_j V^j + \Phi \qquad (6.7a) \\ &= \frac{1}{2} p_j p^j + \frac{1}{2} A_j A^j - p_j A^j + \Phi, \qquad (6.7b) \end{aligned}$$

where $p^i \equiv g^{ij}p_i$. Hamiltons equations of motion are then $\mathrm{d}x^i/\mathrm{d}t = \partial H/\partial p_i$ and $\mathrm{d}p_i/\mathrm{d}t = -\partial H/\partial x^i$.

Note that (6.7*a*) corresponds to the standard Bernoulli equation, which states that H is constant along a streamline. This could also be seen from (4.12), which gives the directional derivative of H along a streamline,

$$V^j \frac{\partial H}{\partial x^j} = V^j \nabla_j H = V_j f^j = 0, \tag{6.8}$$

where the last equality follows from the Coriolis acceleration being orthogonal to V^i, cf. (4.11).

6.1. *The unforced case - Geodesic flows*

Consider the nonlinear surface flow equation, (4.12), in the coordinate-independent form. We shall see that we can in some cases obtain knowledge of the general solution without even bothering to introduce a coordinate system. A special case occurs, when Φ and f vanish, and (6.2) simplifies to

$$\frac{\mathrm{d}^2 x^i}{\mathrm{d}t^2} + \Gamma^i_{jk} \frac{\mathrm{d}x^j}{\mathrm{d}t} \frac{\mathrm{d}x^k}{\mathrm{d}t} = 0. \tag{6.9}$$

This is the equation for a *geodesic* curve on the surface manifold, cf. Carroll (2003). So the solutions to (4.12) on a manifold is a family of non-intersecting geodesic curves.

6.2. *The nearly planar case*

Consider the case when the physical coordinates describing the free surface are $(x, y, h(x, y))$ for small heights h. Then the metric tensor for the surface manifold is given by (A 2), and

$$g_{ij} = \delta_{ij} + \mathcal{O}(h^2). \tag{6.10}$$

The correction term is of second order in h and its gradient, and so are the connection coefficients Γ^i_{jk}. To lowest order in h and expressed in terms of the physical velocity components $\mathbf{v} = (u, v)$, (4.12) becomes

$$(\mathbf{v} \cdot \nabla)\mathbf{v} = -\mathbf{f} \times \mathbf{v} - \nabla\Phi, \tag{6.11}$$

where the potential takes the form $\Phi = g_0 h$ in a uniform gravity field of magnitude g_0. In traditional geophysical notation, we define the Coriolis Parameter $\mathbf{f}$ as a vector pointing upwards out of the plane with $\|\mathbf{f}\| = 2\Omega \sin\phi$ on the geographical latitude ϕ.

Now, (6.2) become

$$\dot{\mathbf{v}} = -\mathbf{f} \times \mathbf{v} - \nabla\Phi, \tag{6.12a}$$

$$\dot{\mathbf{x}} = \mathbf{v}. \tag{6.12b}$$

These equations of motion correspond to the Lagrangian L and Hamiltonian H,

$$L = \frac{1}{2}\|\dot{\mathbf{x}}\|^2 + \frac{1}{2}\dot{\mathbf{x}} \cdot (\mathbf{f} \times \mathbf{x}) - \Phi, \tag{6.13}$$

$$H = \frac{1}{2}\|\mathbf{p}\|^2 + \frac{1}{8}\|\mathbf{f}\|^2\|\mathbf{x}\|^2 - \frac{1}{2}\mathbf{p} \cdot (\mathbf{f} \times \mathbf{x}) + \Phi, \tag{6.14}$$

where the conjugate momenta are $p_i \equiv \partial L/\partial \dot{x}_i = \dot{x}_i + \varepsilon_{i3k} f\, x_k$. Hamilton's equations of motion are $\dot{p}_i = -\partial H/\partial x_i$, $\dot{x}_i = \partial H/\partial p_i$.

7. Existence of solutions to the surface flow problem

As we have seen, it is possible to solve the surface flow equations (4.12) for important special cases with symmetry and - at least perturbatively - when the symmetry is broken. As we shall now see, however, it is not guaranteed that a solution of (4.12) for a given surface shape and given boundary conditions exists at all. To analyse this question for various cases, we shall make frequent use of the dynamical systems description of last section.

As an example, consider a planar horizontal free surface with no vertical forcing. The particle orbits are geodesics, which according to (6.9) are straight lines. They must also be streamlines, so the only solution in a connected open subset of the plane is a parallel flow. The flow speeds on distinct streamlines are not related through (6.9), which contain only the acceleration of fluid particles along their path of motion, and obviously we can specify any parallel flow on (part of) the boundary.

Another example is a spherical drop of liquid. Without an external potential, and even in the presence of surface tension, the right hand side of (4.12) vanishes, and we are again left with geodesic flows(6.9). The geodesics on the sphere are great circles. Any two non-identical great circles intersect each other at two points, and (4.12) has only one global solution, $V^i = 0$. So the only equilibrium state for a spherical drop of inviscid liquid without external forcing is a state where the particles on the surface are at rest.

Ellipsoids can be analyzed using a similar argument. A general triaxial ellipsoid has more complicated geodesics, cf. Arnold (1978), §47. A single geodesic is either a closed curve, or it is dense in an area between two confocal one-sheet hyperboloids. This behaviour is incompatible with the idea of a geodesic flow with $V^i = V^i(x^j)$. An analysis of surface conditions on equilibrium shapes of self-gravitating fluid bodies, e.g. Dedekind ellipsoids, could be pursued from (4.12) including a non-zero forcing.

The existence of solutions is an issue even for the nearly planar case studied in section 6.2. As a prelude to considering boundary value problems involving (6.11), let us make a few remarks on boundary value problem for "ordinary" stationary inviscid incompressible flows. Consider the Euler equation and the continuity equation in a compact domain in the plane with boundary conditions giving the normal flow velocity through the boundary. Assuming irrotational flow, the problem reduces to solving the Laplace equation on the domain with Neumann boundary conditions, which is possible under rather general conditions, for example the total influx to the domain must be zero. For a mathematical discussion, cf. Courant and Hilbert (1989), vol. II ch. IV. While this irrotational flow may not be the only solution to the flow problem, we know at least that a solution exist.

Boundary value problems in (6.11) are somewhat different. We now give an example of a boundary value problem which apparently has no solution at all. Consider (6.11) on the half-plane $x > -1$ with the boundary condition $u = 0$ at $x = -1$, cf. figure 4(a). We take the potential to describe a circular

harmonic well centered at the origin,

$$\mathbf{f} = 0, \qquad \Phi = \frac{1}{2}(x^2 + y^2), \tag{7.1}$$

Each component of (6.12) is simply an unforced harmonic oscillator of unit angular velocity, i.e $\ddot{x}_i + x_i = 0$. So any solution to (6.12) describes a particle moving about on an ellipse centered at the origin. As shown in figure 4, the trajectories of any two particles starting out at distinct points on the boundary will intersect and have different velocities at the points of intersection, in conflict with the condition that the velocity depends on the position alone. So it appears that this boundary value problem has no solutions at all. Note that other choices of boundaries of prescribed normal velocities may yield a well-posed boundary value problem. For example, applying no-penetration boundary conditions to one of the elliptic trajectories to (6.12), we can find a solution, with streamlines consisting of downsized versions of the boundary curve.

A further complication becomes apparent if we break the symmetry of (7.1) slightly and take

$$\mathbf{f} = 0, \qquad \Phi = \frac{1}{2}(x^2 + \omega^2 y^2), \tag{7.2}$$

where $x = x_1$ and $y = x_2$, and $\omega = 1+\delta$, $\delta \ll 1$. With (7.2), (6.12) separates into two harmonic oscillators

$$\ddot{x} = -x, \tag{7.3a}$$

$$\ddot{y} = -\omega^2 y, \tag{7.3b}$$

and the exact solution is straightforward. With the initial condition $x(0) = x_0$, $y(0) = y_0$, $\dot{x}(0) = u_0$ and $\dot{y}(0) = v_0$ in terms of real numbers x_0, y_0, u_0, v_0, the solution is

$$x(t) = \Big(x_0 + iu_0\Big)e^{-it}, \tag{7.4a}$$

$$y(t) = \Big(y_0 + i\frac{v_0}{\omega}\Big)e^{-i\omega t}, \tag{7.4b}$$

where the real part of (7.4) is understood as the position. The motion is clearly bounded to a rectangle $\mathcal{D} = \{(x, y) : |x| \leq x_M \wedge |y| \leq y_M\}$ with $x_M = \sqrt{x_0^2 + u_0^2}$ and $y_M = \sqrt{y_0^2 + v_0^2/\omega^2}$. If ω is rational and expressed as an irreducible fraction p/q, the motion (7.4) will be periodic with period $2\pi q$. During one such period, x will oscillate q times while y will oscillate p times. In the process, the orbit will necessary self-intersect several times, if q is large. In the case, when ω is irrational, the system will never return to the initial condition, and the motion is quasiperiodic. The orbit will then eventually cover $\mathcal{D}$ densely.

A set of orbits to (7.3) is shown in 4. As the trajectory meanders around in the rectangle $\mathcal{D}$, it suffers several self-intersections. Such an orbit is clearly not a permissible streamline of a time-independent flow. Introducing non-harmonic terms in Φ in (7.2) only makes the situation worse, since we shall find chaotic orbits with self-intersections irregularly distributed, and thus

it becomes even harder to find a domain, where the streamlines do not intersect.

Apparently, the linearized version of (4.12) with (7.2) has no solution with anything even resembling closed streamlines. On the other hand, given a potential and a domain with a given boundary curve, we can construct a well-posed boundary value problem, if we choose just the right boundary condition. For if we inject a particle at the boundary with a sufficiently large initial speed $\mathbf{v}_0$, the potential gradient forcing becomes a small perturbation, and the trajectories will approach straight lines in the case $\mathbf{f} = 0$ and segments of circles with radius $\|\mathbf{v}_0\|/\|\mathbf{f}\|$ otherwise. Clearly, we can always foliate the domain with trajectories of this form. So, while some boundary value problems cannot be solved, any particular bounded region does have an associated well-posed boundary value problem.

This situation seems at odds with the results of section 5.1, where we used perturbation theory directly on the surface flow equation without any reference to particle orbits. Could the same procedure work in this case as well? To answer this question, we proceed from (A 10) in the limit of small surface deformations where the nonlinear terms in the surface elevation gradient appearing in the connection coefficients can be neglected. Thus we get

$$UU_\rho + VU_\theta - \rho V^2 = -\Phi_\rho, \tag{7.5a}$$

$$UV_\rho + VV\theta + \frac{2}{\rho}UV = -\frac{1}{\rho^2}\Phi_\theta. \tag{7.5b}$$

Following section 5.1, we take $U \to U + \varepsilon u$, $V \to V + \varepsilon v$ and $\Phi \to \Phi + \varepsilon\phi$. We take as the unperturbed state a flow describing a rigid rotation at the constant angular velocity V, the so-called "Newton's bucket". The zero order part of (7.5) yields the well-known parabolic potential $\Phi = \frac{1}{2}V^2\rho^2$. To first order, we get the linear system

$$u_\theta - 2\rho v = -\frac{1}{V}\phi_\rho, \tag{7.6a}$$

$$\frac{2}{\rho}u + v_\theta = -\frac{1}{\rho^2 V}\phi_\theta. \tag{7.6b}$$

For a Fourier mode of wavenumber n, we can replace the θ derivative by the factor $i\,n$, and (7.6) yields an algebraic linear system of equations in the Fourier modes u_n and v_n. From (7.6), we observe that the system determinant has the value

$$4 - n^2$$

Evidently, (7.6) cannot be solved for the $n = 2$ Fourier mode. The potential given in (7.2) describes a perturbation of just that sort, with $\phi = \frac{1}{2}y^2 = \frac{1}{2}\rho^2(\cos 2\theta - 1)$. So we are unable to find nearly circular streamlines to (7.5), in agreement with our analysis of (7.3), whose exact solution shows that such streamlines do not exist.

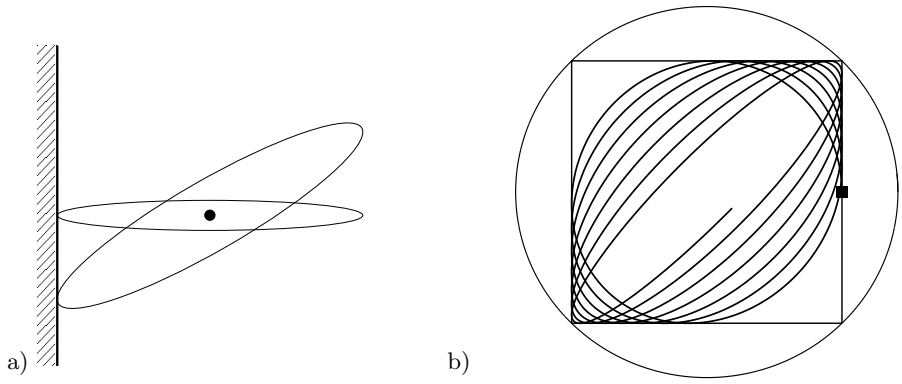

FIGURE 4. a) Example of a boundary value problem in (6.11) with no solution. The parameters are given in (7.1). Any solutions to (6.12) trace ellipses centered at the origin (shown by the black dot). Impenetrable boundary conditions are applied at the line $x = -1$. A particle at a point $\mathbf{x}_0 = (-1, y)$ at the boundary with velocity $\mathbf{v} = (0, v)$ will be advected according to (6.12) along an ellipse connecting the points $\mathbf{x}_0$ and $-\mathbf{x}_0$. Clearly, any two such trajectories emanating from distinct points on the boundary will intersect, and their velocities at the intersection points will not be identical. This is incompatible with the uniqueness of streamlines at each point of a stationary flow, and it seems that this boundary value problem has no solution at all.
b) Position view (x, y) of a trajectory of the dynamical system (6.12) with the potential given by (7.2) with $\omega^2 = 1.06$. The particle is starts at the point marked by the black dot, $(x_0, y_0) = (1, 0)$ with an initial velocity $(u_0, v_0) = (0, 1)$. The very slightly eccentric ellipse surrounding the orbit is the region $\Phi \leq E_0 \equiv \frac{1}{2}(u_0^2 + v_0^2) + \Phi(t_0)$, where the particle has sufficient energy to go. In fact, due to the decoupling of (7.3), energy is conserved separately for the motion in x and y, so the orbit is contained within the rectangle $\mathcal{D}$. Here ω is irrational, so the orbit will eventually cover $\mathcal{D}$ densely. With self-intersections this orbit clearly cannot be a streamline of a stationary flow.

8. Conclusion

We have shown that it is possible to write down a self-contained set of equations for the flow on a stationary, free surface of an ideal fluid. It is given by Eq. (4.12), which is the main result of the paper. We have shown how to include surface tension and velocity dependent forces such as the Coriolis force, and demonstrated that the formalism provides a practical tool for determining actual flows on surfaces of simple shapes. We also showed that it can be used to predict that given surface shapes, boundary conditions or domains preclude the existence of a single-valued surface velocity field. Here the analogy to Hamiltonian particle dynamics with two-degree of freedom is very useful. The latter problem can always be solved with given initial conditions, and hence the question of existence of a velocity field on the surface becomes a question of projecting from the energy surface of the four-dimensional phase space of the dynamical system to the two-dimensional space of the surface - without intersections. In the present paper, we have given a preliminary analysis of this problem, and we believe that there are ample possibilities for developing this approach further in future work.

Finally, we might mention that in modelling sea currents one is faced with a problem very similar to ours. Here satellite measurements of the free surface elevation (altimetry) on a grid of points around the globe is used to predict the ocean currents. It is customary (see e.g. Ray (2001)) to work in the linear, geostrophic approximation, where the inertial term (the left hand side of (6.11)) is ignored, and the Coriolis term balances the

forcing on the surface flow. If one were to include the nonlinear terms, one might in principle find that the surface shapes assumed cannot actually support the predicted flows! In the present state of our theory, however, we cannot perform such an analysis since we would first have to build in effects like time dependence and wind stresses, which are important for the ocean currents.

Appendix A. The form of the surface flow equations in simple situations

A.1. *Cartesian base coordinates*

We shall now give an example of the general equations, (4.12) for the surface flow derived in the previous section. Consider a free surface parameterized by $(x^1, x^2) \equiv (x, y)$ so the Cartesian laboratory coordinates y^α are

$$(y^1, y^2, y^3) = (x, y, h(x, y)). \tag{A 1}$$

The 2D metric tensor and its determinant for the surface manifold are then, by (4.6),

$$g_{ij} = \begin{pmatrix} 1 + h_x^2 & h_x h_y \\ h_x h_y & 1 + h_y^2 \end{pmatrix}, \tag{A 2}$$

$$g \equiv |g| = 1 + h_x^2 + h_y^2, \tag{A 3}$$

where subscript i denotes differentiation by x^i. The y^α coordinate expression of the dual basis vectors (recall that the velocity vector is $V^i \mathbf{e}_i$) is $\mathbf{e}_x = (1, 0, h_x)$, $\mathbf{e}_y = (0, 1, h_y)$. We denote the velocity vector components by $(V^1, V^2) \equiv (U, V)$.

The coordinate system is assumed to rotate in the counterclockwise direction about the y^3 axis with a constant angular velocity Ω. In order to compute the Coriolis force term, we shall need Ω^3 in terms of the surface-adapted coordinates defined in the beginning of section 4, where $\mathbf{e}_3 = 1/\sqrt{g} \cdot (-h_x, -h_y, 1)$ in y^α-coordinates. Thus, $\Omega^3 = \Omega\, \mathbf{e}_3 \cdot (0, 0, 1) = \Omega/\sqrt{g}$. Now, (4.12) becomes, for the x and y directions, respectively:

$$\begin{aligned}(UU_x + VU_y) + h_x M = \frac{1}{g}\left(-(1 + h_y^2)\Phi_x + h_x h_y \Phi_y\right) \\ + 2\Omega \frac{1}{g}\left(h_x h_y U + (1 + h_y^2)V\right),\end{aligned} \tag{A 4a}$$

$$\begin{aligned}(UV_x + VV_y) + h_y M = \frac{1}{g}\left(\ \ h_x h_y \Phi_x - (1 + h_x^2)\Phi_y\right) \\ - 2\Omega \frac{1}{g}\left((1 + h_x^2)U + h_x h_y V\right),\end{aligned} \tag{A 4b}$$

where

$$M = \frac{1}{g}(h_{xx}U^2 + 2h_{xy}UV + h_{yy}V^2). \tag{A 5}$$

If we include a centrifugal force, a gravitational potential $g_0 h(x, y)$ and a

surface tension γ with the associated Young-Laplace pressure on the free surface, and denote the constant liquid mass density by ρ_0, we have

$$\Phi(x,y) = -\frac{1}{2}\Omega^2\left(x^2+y^2\right) + g_0 h(x,y) - 2\frac{\gamma}{\rho_0} H(x,y), \tag{A 6}$$

where H is the mean curvature (positive in the y^3 direction) of the free surface and must be computed from (A 1), for example using (4.8).

A.2. *Polar base coordinates*

We do the same for polar (ρ,θ) base coordinates, i.e.

$$(y^1,y^2,y^3) = (\rho\cos\theta, \rho\sin\theta, h(\rho,\theta)), \tag{A 7}$$

with the metric

$$g_{ij} = \begin{pmatrix} 1+h_\rho^2 & h_\rho h_\theta \\ h_\rho h_\theta & \rho^2+h_\theta^2 \end{pmatrix}, \tag{A 8}$$

$$g = \rho^2 + \rho^2 h_\rho^2 + h_\theta^2. \tag{A 9}$$

The dual basis expressed in y^α coordinates is $\mathbf{e}_\rho = (\cos\theta, \sin\theta, h_\rho)$, $\mathbf{e}_\theta = (-\rho\sin\theta, \rho\cos\theta, h_\theta)$. The relevant component of Ω^μ, corresponding to a rotation vector of magnitude Ω in the positive y^3 direction, is $\Omega^3 = \rho\Omega/\sqrt{g}$. Now, (4.12) becomes, for ρ and θ, respectively:

$$\begin{aligned}
&(UU_\rho + VU_\theta) + \\
&\frac{1}{g}\Big[\rho^2 h_\rho h_{\rho\rho} U^2 + 2\rho h_\rho(\rho h_{\rho\theta} - h_\theta)UV + \rho(\rho h_\rho h_{\theta\theta} - \rho^2 - h_\theta^2)V^2\Big] \\
&\qquad = \frac{1}{g}\left[-(h_\theta^2+\rho^2)\Phi_\rho + h_\rho h_\theta \Phi_\theta\right] \\
&\qquad\quad + 2\Omega\frac{\rho}{g}\Big[h_\rho h_\theta U + (\rho^2+h_\theta^2)V\Big],
\end{aligned} \tag{A 10a}$$

$$\begin{aligned}
&(UV_\rho + VV_\theta) + \\
&\quad\frac{1}{g}\Big[h_\theta h_{\rho\rho} U^2 + 2\big(\rho(1+h_\rho^2) + h_\theta h_{\rho\theta}\big)UV + h_\theta(\rho h_\rho + h_{\theta\theta})V^2\Big] \\
&\qquad = \frac{1}{g}\left[\ \ h_\rho h_\theta \Phi_\rho - (1+h_\rho^2)\Phi_\theta\right] \\
&\qquad\quad - 2\Omega\frac{\rho}{g}\Big[(1+h_\rho^2)U + h_\rho h_\theta V\Big].
\end{aligned} \tag{A 10b}$$

Including the same physical effects as in the previous section, cf. (A 6), we have the potential

$$\Phi(\rho,\theta) = -\frac{1}{2}\Omega^2\rho^2 + g_0 h(\rho,\theta) - 2\frac{\gamma}{\rho_0} H(\rho,\theta). \tag{A 11}$$

REFERENCES

V.I. Arnold. *Mathematical methods of classical mechanics*. Springer-Verlag, 1978.

R. Bergmann, L. Tophøj, T. Homan, P. Hersen, A. Andersen, and T. Bohr. Polygon formation and surface flow on a rotating fluid surface. *J. Fluid Mech.*, 679:415–431, 2011.

Sean Carroll. *Spacetime and Geometry: An Introduction to General Relativity*. Pearson, 2003.

R. Courant and D. Hilbert. *Methods of Mathematical Physics*. Wiley, 1989.

Manfredo P. do Carmo. *Differential Geometry of Curves and Surfaces*. Prentice-Hall, 1976.

A. A. Ilin. The navier-stokes and euler equations of two-dimensional closed manifolds. *Math. USSR Sbornik*, 69:559–579, 1991.

L. P. Lebedev, M. J. Cloud, and V. A. Eremeyev. *Tensor analysis with applications in mechanics*. World Scientific, 2010.

R.D. Ray. Inversion of oceanic tidal currents from measured elevations. *Journal of Marine Systems*, 28(12):1 – 18, 2001.

J.J. Stoker. *Differential Geometry*. Wiley, 1969.

J. Fluid Mech. (2011), *vol.* 679, *pp.* 415–431.
doi:10.1017/jfm.2011.152

Polygon formation and surface flow on a rotating fluid surface

R. BERGMANN[1]†, L. TOPHØJ[1], T. A. M. HOMAN[1,2], P. HERSEN[3], A. ANDERSEN[1] AND T. BOHR[1]

[1]Department of Physics and Center for Fluid Dynamics, Technical University of Denmark, DK-2800 Kgs Lyngby, Denmark

[2]Physics of Fluids Group and J. M. Burgers Centre for Fluid Dynamics, University of Twente, 7500 AE Enschede, The Netherlands

[3]Laboratoire Matière et Systèmes Complexes, CNRS and Université Paris Diderot, Paris 75013, France

(Received 10 June 2010; revised 17 December 2010; accepted 24 March 2011; first published online 24 May 2011)

We present a study of polygons forming on the free surface of a water flow confined to a stationary cylinder and driven by a rotating bottom plate as described by Jansson *et al.* (*Phys. Rev. Lett.*, vol. 96, 2006, 174502). In particular, we study the case of a triangular structure, either completely 'wet' or with a 'dry' centre. For the dry structures, we present measurements of the surface shapes and the process of formation. We show experimental evidence that the formation can take place as a two-stage process: first the system approaches an almost stable rotationally symmetric state and from there the symmetry breaking proceeds like a low-dimensional linear instability. We show that the circular state and the unstable manifold connecting it with the polygon solution are universal in the sense that very different initial conditions lead to the same circular state and unstable manifold. For a wet triangle, we measure the surface flows by particle image velocimetry (PIV) and show that there are three vortices present, but that the strength of these vortices is far too weak to account for the rotation velocity of the polygon. We show that partial blocking of the surface flow destroys the polygons and re-establishes the rotational symmetry. For the rotationally symmetric state our theoretical analysis of the surface flow shows that it consists of two distinct regions: an inner, rigidly rotating centre and an outer annulus, where the surface flow is that of a point vortex with a weak secondary flow. This prediction is consistent with the experimentally determined surface flow.

Key words: rotating flows, vortex flows, waves/free-surface flows

1. Introduction

The free surface of a fluid in a circular container with a rotating bottom plate can undergo a surprising instability by which the surface shape spontaneously breaks rotational symmetry and turns into a rotating polygon. These shapes were first noticed by Vatistas (1990) and the polygon rotation was subsequently analysed in terms of waves rotating around a vortex core by Vatistas, Wang & Lin (1992, 1994). The

† Present address: Instrumentation and Controls Department, German–Dutch Wind Tunnels, Emmeloord, The Netherlands. Email address for correspondence: tbohr@fysik.dtu.dk

surface polygons are nearly invariant in a frame rotating with a rate considerably less than that of the bottom plate and also less than that of the mean azimuthal flow of the water around the polygon.

The fact that the instability leads to spontaneous symmetry breaking was emphasized by Jansson *et al.* (2006), who pointed out that vortices, presumably formed due to the strong shear-flow, seem to play a large role. It is well known that steady patterns of vortices can form in two-dimensional and circular shear-flows due to Kelvin–Helmholtz instability, as shown by Rabaud & Couder (1983). The instability in the present system is less well understood, since the shear-flow in this case is fully three-dimensional and the strength and width of the shear zone are not easily determined as a function of the control parameters. It is intriguing to note in passing that a hexagonal cloud system, which resembles the structures described here, was seen on the north pole of Saturn from the spacecrafts Voyager (Godfrey 1988) and Cassini. Indeed the basic ingredients are present in both cases: the rotation from the bottom and a strong change in the rotation rate from a rapidly rotating centre to an almost stagnant outer layer.

The experimental set-up consists of a stationary cylindrical container in which the (bottom) circular plate is rotated. Water is filled to a certain level above the rotating plate, and when the plate is set into rotation, the centrifugal force presses the fluid outwards, deforming the free surface. When the rotation rate becomes sufficiently large, the axial symmetry of the free surface is spontaneously broken and large, time-dependent deformations appear. This can result in stable, rigidly rotating surface shapes in the form of regular polygons with N corners.

The number of corners of the polygons depends on the amount of water in the tank and the rotation rate of the bottom plate. A larger amount of water leads to fewer corners and a larger rotation rate leads to more corners, as first pointed out by Vatistas (1990). In a phase diagram using the initial filling height and the rotational frequency of the bottom plate, the transition lines between different polygons are almost straight lines with positive slopes (Jansson *et al.* 2006). The phase diagram contains both 'dry' polygons, where the surface becomes so strongly deformed that the central part becomes dry, and 'wet' polygons which remain entirely above the bottom plate. It is interesting to note that spontaneous symmetry breaking of the internal flow of our system (i.e. a cylinder with a rotating bottom) occurs for a much lower Reynolds number. Thus periodic internal waves, breaking the rotational symmetry, appear at rotation rates that are so low that the free surface remains virtually flat, and the bifurcations go in the opposite direction than the one for the surface deformations: higher rotation rates lead to smaller wavelengths (Hirsa, Lopez & Miraghaie 2002; Miraghaie, Lopez & Hirsa 2003; Lopez *et al.* 2004; Poncet & Chauve 2007).

The existence of the surface polygons seems connected with the fact that the flow is turbulent. In fact, switching transitions are observed in similar but smaller systems, where the flow irregularly switches between a weakly deformed, rotationally symmetric state and a strongly deformed state with two corners. Here, the free surface touches the bottom, and this transition is linked with a transition to turbulence (Suzuki, Iima & Hayase 2006; Tasaka & Iima 2009). Thus the strong mixing present in the turbulent flow seems to be necessary for the formation of surface polygons.

The simple structure of the phase diagram and the instability leading to polygon formation remain unexplained despite previous studies. The goal of the present work is to describe the polygon formation process and the surface flow. After briefly describing the experimental set-up, we shall discuss the development of the various modes during the onset of a dry triangular polygon, based on video recordings

of the surface. We shall see that the triangle apparently emerges through a low-dimensional linear instability from a well-defined almost stable rotationally symmetric state. Further, we shall discuss the measured surface flow. For the wet polygons, we find clear evidence for a number of localized vortices forming a ring, as conjectured by Vatistas, Abderrahmane & Kamran Siddiqui (2008), but we note that this ring of line vortices is far from giving an exhaustive description of the flow. We shall see that disturbing the surface flow by adding floating particles can lead to a destabilization of the polygon and a return to a rotationally symmetric state. Finally, we shall discuss the rotationally symmetric state based on the combined information on surface shape and surface flow. Based upon decoupling of the surface flow and the bulk flow in the inviscid limit, the surprisingly simple theoretical prediction, supported by the measurements, is that the surface flow has the profile of a Rankine vortex with a well-defined transition line separating the external line-vortex flow from the central rigidly rotating core.

2. Experimental set-up

The experimental set-up is equivalent to the one used by Jansson *et al.* (2006). A cylindrical, stationary tank made of Plexiglas is provided with a rotating 'bottom' plate (figure 1). In this set-up, the plate is not really at the bottom for practical reasons, but since we make the gap between the rotating plate and the cylinder wall as small as possible (less than 1 mm), the fluid below the plate should not influence the observed structures. In this respect our set-up differs from the one used by Vatistas (1990), where this gap can be quite large and thereby introduces a new length scale into the problem. Our control parameters are as follows: the radius R of the cylindrical container, the height H of the (quiescent) fluid layer and the frequency f of the rotating plate.

The only modification of the set-up used by Jansson *et al.* (2006) is the addition of an 'outer tank'. A stationary, water-filled tank of square cross-section allows us to observe surface shapes from the sides undistorted by refraction. The full three-dimensional information of the surfaces can in principle be obtained by the method illustrated in figure 1(*e*). A vertical laser sheet impinging orthogonally on the outer tank walls illuminates a slice of the surface. Capturing these slices from a full cycle of the rotation allows us then to re-create the full three-dimensional surface shape. A slight complication comes from the fact that the slices might, for certain angles, be behind other parts of the surface, as seen from our camera, but this problem can be solved by rotating the figure also in the opposite way. It has been hard to get high accuracy with this method, so we have used it only to verify shapes obtained more directly. Most experiments were made with the camera mounted vertically above the tank at a distance of approximately 1.5 m above the surface. This allowed us to measure surface flows (i.e. the projection on the horizontal plane of the surface velocities) by particle image velocimetry (PIV) and to see the appearance of polygons. To experimentally determine the surface flows, we have used polystyrene particles of size around 1 mm that are lighter than water.

3. Creation of polygons

3.1. *Structure of dry polygons*

To study the creation of the polygons, we have restricted our attention to the case of dry polygons in which the surface distortion becomes so large that part of the

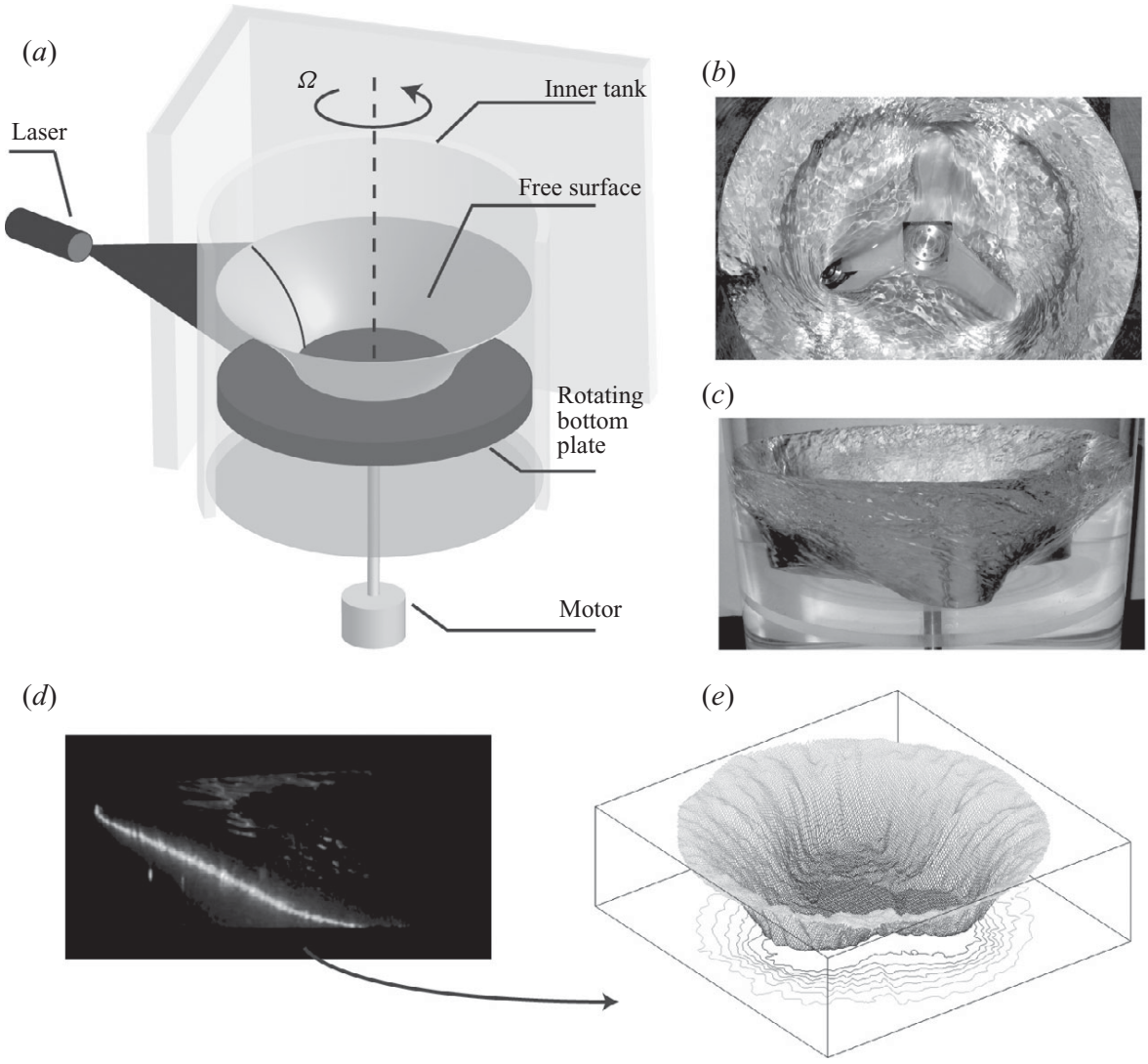

FIGURE 1. (*a*) Sketch of the experimental set-up. The circular tank has a radius of $R = 19.4$ cm. The rotation rate of the bottom plate and the total amount of water are the control parameters. (*b*) and (*c*) A video camera can be placed either on the sides or above the cylinder to obtain live recording of the polygon formation. It is also possible to use a vertical laser sheet to reconstruct the three-dimensional surface shapes. (*d*) Typical picture showing the scattered light from the laser sheet. (*e*) Three-dimensional surface shape reconstructed from multiple side views such as the one shown in (*d*). It shows a triangle with a dry centre.

free surface touches the rotating bottom. In these states a picture from above clearly shows a contour defining the polygon as shown in figure 2. This is not really a contact line because, due to the different rotation rates of the plate and the polygon, part of the bottom is covered by a thin water film. The contour is quite well defined and can easily be identified in top-down photographs as shown in figure 2. We shall take this contour as a simple characteristic of the shape and use it to identify the presence of the discrete rotational symmetry through Fourier decomposition.

3.2. *Formation of polygons*

When the bottom plate is set into rotation, it takes some time for the fluid to spin up. During this process the central part of the surface is lowered, developing into a near parabolic shape. When the centre reaches the bottom, a fluctuating contour emerges which grows rapidly while becoming increasingly circular. Figure 3 shows a sequence

FIGURE 2. Dry triangle with $H = 4$ cm and $f = 2.4$ Hz. Inside the faint circle the bottom plate is dry. Between the faint circle and the rotating polygonal contour there is a thin fluid layer.

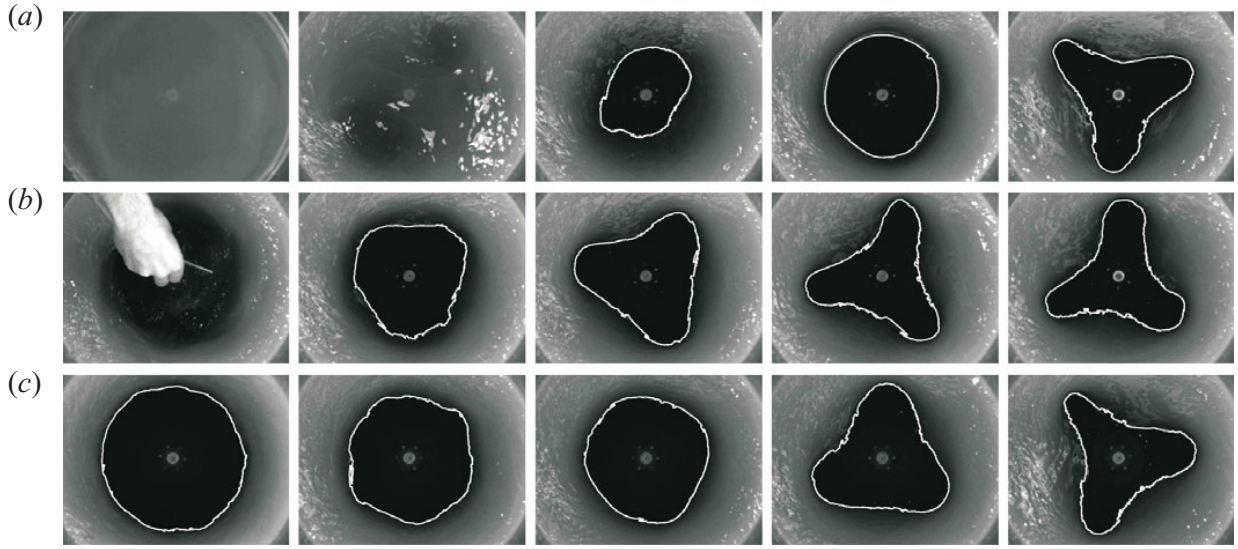

FIGURE 3. The formation process for a dry triangle with $H = 4$ cm and $f = 2.4$ Hz and three different initial conditions. (*a*) Starting from rest. (*b*) Starting by manually destroying a fully developed triangle. (*c*) Starting from a high initial rotation rate $f = 3.3$ Hz where the shape is circular. The time between consecutive frames is 9.3 s in (*a*), 4.0 s in (*b*) and 8.0 s in (*c*). A bit of dye was added to the water to increase the contrast. In all three cases a rotationally symmetric state is formed before the triangle bifurcates out.

of pictures together with examples of extracted contours from videos showing the development of a triangle. In these sequences the triangle is formed in three different ways in order to check the robustness. One way is to start from rest and spin up the

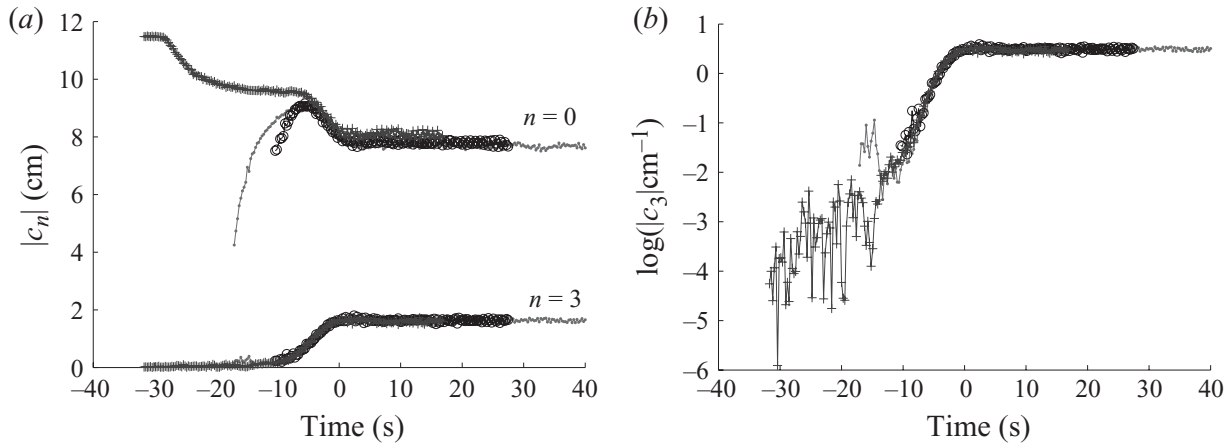

FIGURE 4. (*a*) The time evolution for the circular ($n=0$) and triangular ($n=3$) Fourier components for different initial conditions of figure 3. The top three lines are the $n=0$ mode and the bottom three lines are the $n=3$ mode. The lines with the dotted, crossed and open symbols are obtained from the image sequence in figure 3(*a*,–*c*) respectively. For all three cases, the zero of time has been chosen at the point where the $n=3$ mode reaches its constant value. (*b*) Semi-logarithmic plot of the $n=3$ modes of (*a*) which is indicative of exponential growth.

system. The second way is to first let the triangle develop, but then perturb it strongly by inserting a plate deep into the fluid and then follow the re-creation of the triangle. Finally, the third way is to use the circular state found at higher rotation rates as an initial condition and then suddenly quench down the rotation rate.

3.3. *Quantitative analysis of the formation process*

To analyse the contours, we compute the Fourier coefficients $c_n = (2\pi)^{-1}\int_0^{2\pi} r(\theta)\,\mathrm{e}^{\mathrm{i}n\theta}\,\mathrm{d}\,\theta$, where $r=r(\theta)$ denotes the contour and θ the azimuthal angle. The low-order Fourier modes are particularly interesting. Thus, the $n=0$ mode gives the average size, the $n=1$ mode gives the off-centre displacement and the $n=2$ mode gives an elliptical distortion. Of particular interest for the formation of a triangle is the $n=3$ mode. Figure 4 shows the time evolution of the $n=0$ mode and the $n=3$ mode for the initial conditions shown in figure 3. It is seen that the development in all three cases occurs in two stages: first a nearly circular state is formed and only after that does the triangle bifurcate out. To see this more clearly, a slice is shown in figure 5 through the 'phase space' formed by the different Fourier modes or, more precisely, their absolute values $|c_n|$. The particular slice (phase plane) has the $n=0$ mode on the x-axis and the $n=3$ mode on the y-axis. The lines track the development from the different initial conditions, and it is seen that there is a 'near fixed point' on the x-axis, i.e. a circle, from where the trajectory diverges out towards the triangular fixed point, where both the $n=0$ and $n=3$ modes have finite values. As shown in figure 4(*b*), the divergence along the 'unstable manifold' emerging from it is indicative of exponential growth within the available accuracy. Thus, this very high-dimensional dynamical system behaves as if the circular state – which is stable for both high and low rotation rates – actually remains nearly stable for all rotation rates. When the polygons form, apparently most directions in this large phase space will still be attracted towards the circular state, and only one or a few become unstable, moving the system away in the direction of the polygon state. Thus the system behaves like pattern-forming systems in confined geometries, where the modes are discrete, i.e. like a low-dimensional

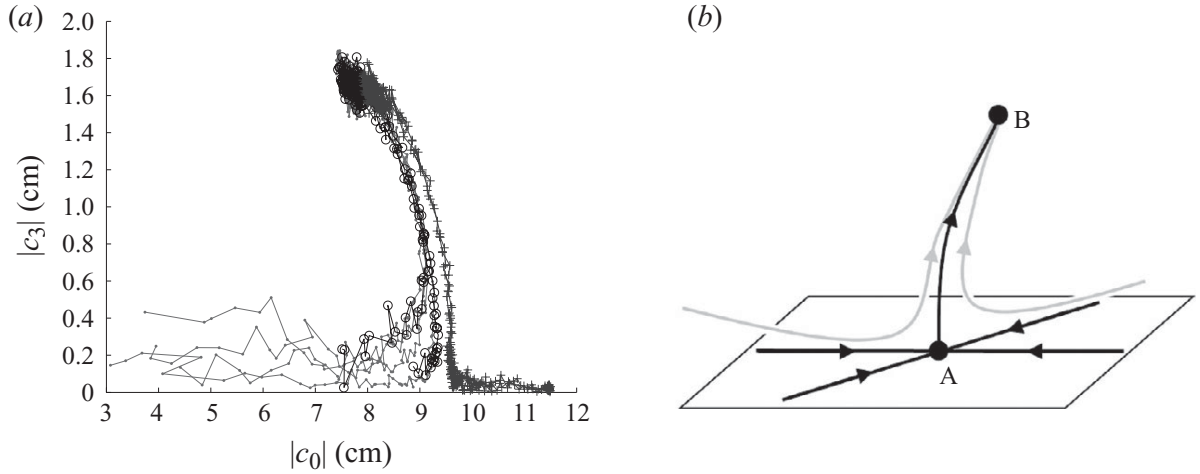

FIGURE 5. Phase-space plot for the onset of a dry triangle showing the time evolution of the shape of the contour. (*a*) Amplitude of the $n=3$ mode versus the $n=0$ mode. The lines with dotted, crossed and open symbols are obtained using nine measurements of the three different initial conditions discussed in the text, i.e. spin-up from rest (dots), perturbing the triangle with a plate (crosses) and quenching the rotation rate from a large value (open circles). (*b*) Qualitative structure of the phase space showing the nearly stable circular fixed point A and the stable triangular fixed point B. The essential feature is that all initial conditions come near to A before they proceed along the well-defined unstable manifold leading from A to B.

dynamical system as sketched in figure 5(*b*). We have observed the same qualitative behaviour for other polygons, but we cannot claim that the above scenario is universal for the entire phase diagram. The richness of possible states, including multistability (Jansson *et al.* 2006), probably also means that the transition mechanism can be more complicated.

4. Surface shapes and flows for polygons

In the remainder of the paper we shall concentrate on the surface flows – first experimentally and then theoretically. Due to the secondary flow, the particles have a strong tendency to move towards the centre, and it is thus experimentally more difficult to get a well-resolved velocity field near the edges. As an important example, where the vortical structure of the surface flow can be seen clearly, we study a 'wet' triangle. The tendency to gather near the centre is clearly seen from figure 6 showing the final state of a wet triangle with particles initially evenly spread on the surface. Performing the recording at intermediate times, when the particles have not yet moved to the centre, we can measure flows over most of the surface as shown in figure 7. The particles were used as sparsely as possible and the results of 100 frames were combined to deal with any gaps in the measured flow field. Figure 7 is complemented by figure 8 where the rotation speed of the figure is subtracted, thus showing the surface flow in the co-rotating ('figure') frame, where the figure remains stationary. As shown in the blow-up figure 8(*b*) one clearly sees a vortex in each of the arms.

From the PIV data, it is possible to compute streamlines, some of which are shown in figure 9. It is clearly seen that the particles spiral in towards the vortices from the outside but away from the vortex cores.

It has been speculated that the flow may be described by a simple point vortex model; see Vatistas *et al.* (2008). We can test this idea by using the data shown

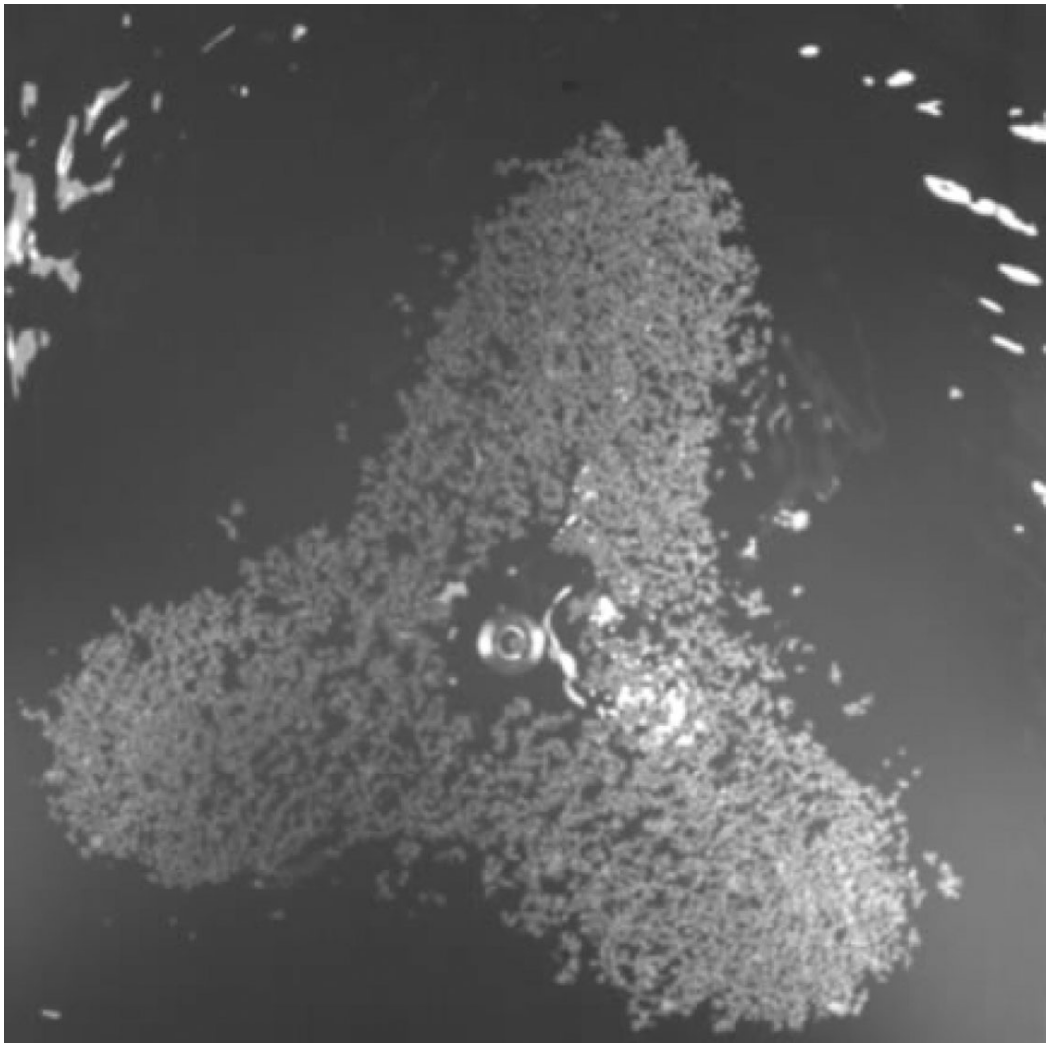

FIGURE 6. Polystyrene particles of size around 1 mm that are lighter than water were used to measure the surface flows. The picture shows the final distribution of particles, initially evenly distributed on the surface, for a wet triangle ($f = 1.9$ Hz and $H = 4$ cm). The particles are attracted to a region near the centre, where the vortices form (see figure 9). Note that, despite the similarity with the contour in figure 3, the surface does not touch the bottom.

in figures 7 and 8. From the figure-frame flow (figure 8), we note that the vortex has an apparent width of $\Delta r \approx 45\,\mathrm{mm}$ and is centred at a distance $R_v \approx 110\,\mathrm{mm}$ from the rotation axis. From figure 7, we note that the velocity difference across the vortex width, as measured in the laboratory frame, is $\Delta v \approx 350\,\mathrm{mm\,s^{-1}}$. This gives an estimated vortex strength (i.e. total circulation) $\Gamma \approx 2\pi(\Delta v/2)(\Delta r/2) \approx 0.02\,\mathrm{m^2\,s^{-1}}$. Considering a simple point vortex model of the flow in the unbounded plane, a configuration of three vortices of equal strength Γ forming the corners of an equilateral triangle on a circle of radius r_v will be stationary in a reference frame rotating about the origin with the angular velocity (see e.g. Aref *et al.* 2003)

$$\Omega = \frac{\Gamma}{2\pi R\, r_v^2} \approx 0.26\,\mathrm{rad\,s^{-1}}. \tag{4.1}$$

The actual polygon is observed to revolve with the much higher angular velocity $\Omega = 2.4$ rad $\mathrm{s^{-1}}$, i.e. almost 10 times faster. Refining the model by introducing image counter-rotating vortices outside the cylinder so as to satisfy the no-penetration boundary condition at the cylinder wall does not improve matters much. The inclusion

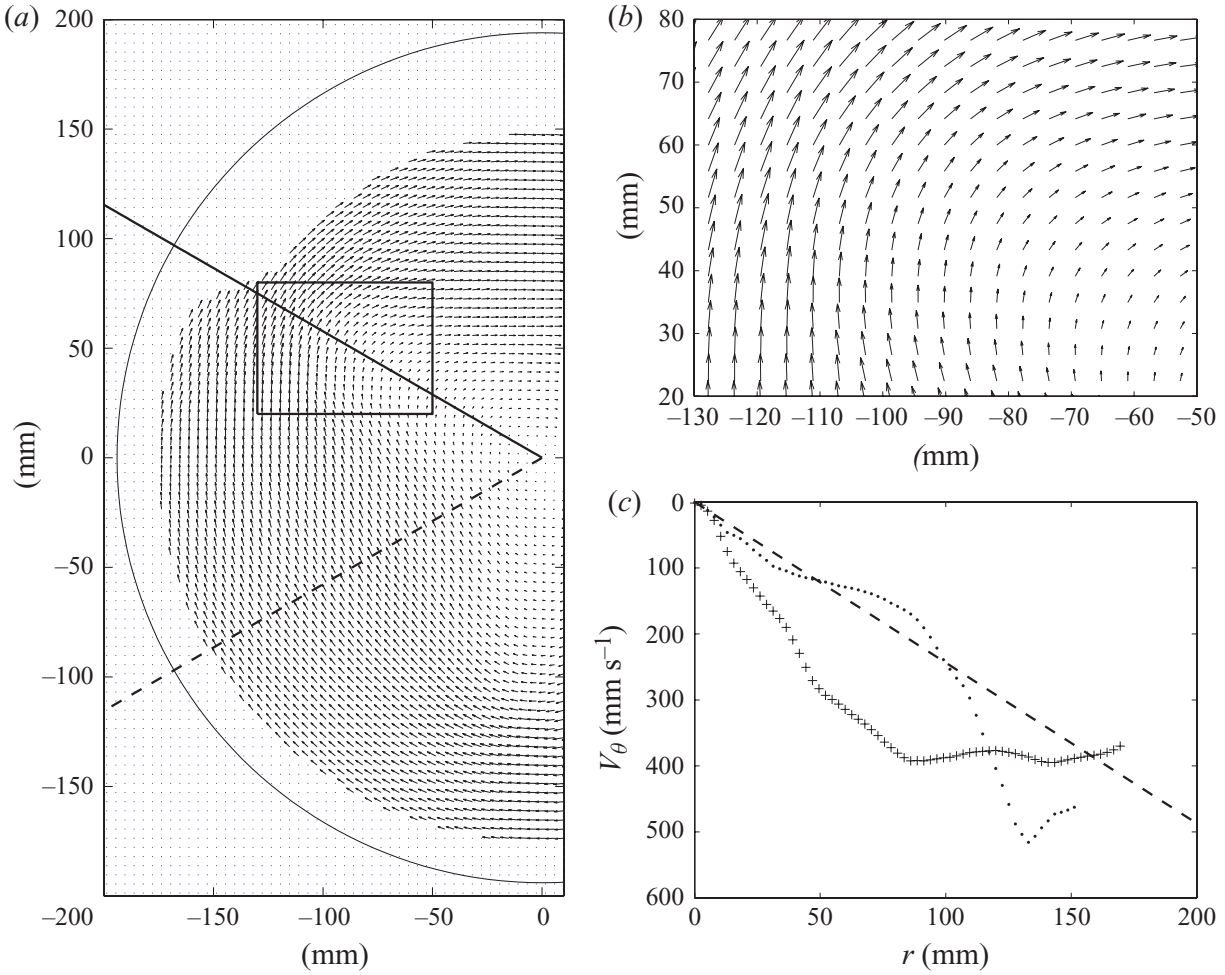

FIGURE 7. (*a*) The surface flow measured by PIV for $f = 1.9$ Hz and $H = 4$ cm. The flow is recorded at 1000 frames per second and the PIV results are averaged over 100 frames. The centre of the tank is located at (0,0) and the wall of the container is indicated by the black circle. Close to the wall, reflections prohibit the recording of meaningful velocity measurements. One of the arms of the figure is indicated by the solid line, while the dashed line goes through the middle of an edge. (*b*) Zoom of the region of one of the polygon arms (indicated by a box in (*a*)). (*c*) The azimuthal flow as measured in frame (*a*) along the solid line (dots) and the dashed line (crosses). The dashed line in (*c*) gives the solid body rotation velocity of the figure $\Omega \approx 2.44$ rad s^{-1}.

of image vortices leads to a relative increase of the predicted angular velocity (4.1) by about 30 %, which is still far too low. Thus the motion of the vortices is only to a small degree influenced by the advection from the other vortices and must be subjected, in addition, to a strong background velocity field. A Hamiltonian model of point vortices in an otherwise potential flow would capture neither the observed rotation velocities nor the spiralling effects seen in figure 9.

The fact that the surface flow plays a great role for the polygon states can be seen from the following simple experiment in which particles are progressively added to the surface of a dry square as shown in figure 10. Starting with a square, the addition of particles first straightens out the corners and finally forces the system back to the circular state. The tendency of the particles to gather near the centre gives them a strong influence on the surface flow near the contact line and through the thin films in the corners of the polygon. By blocking this flow, the polygon is destroyed. A similar

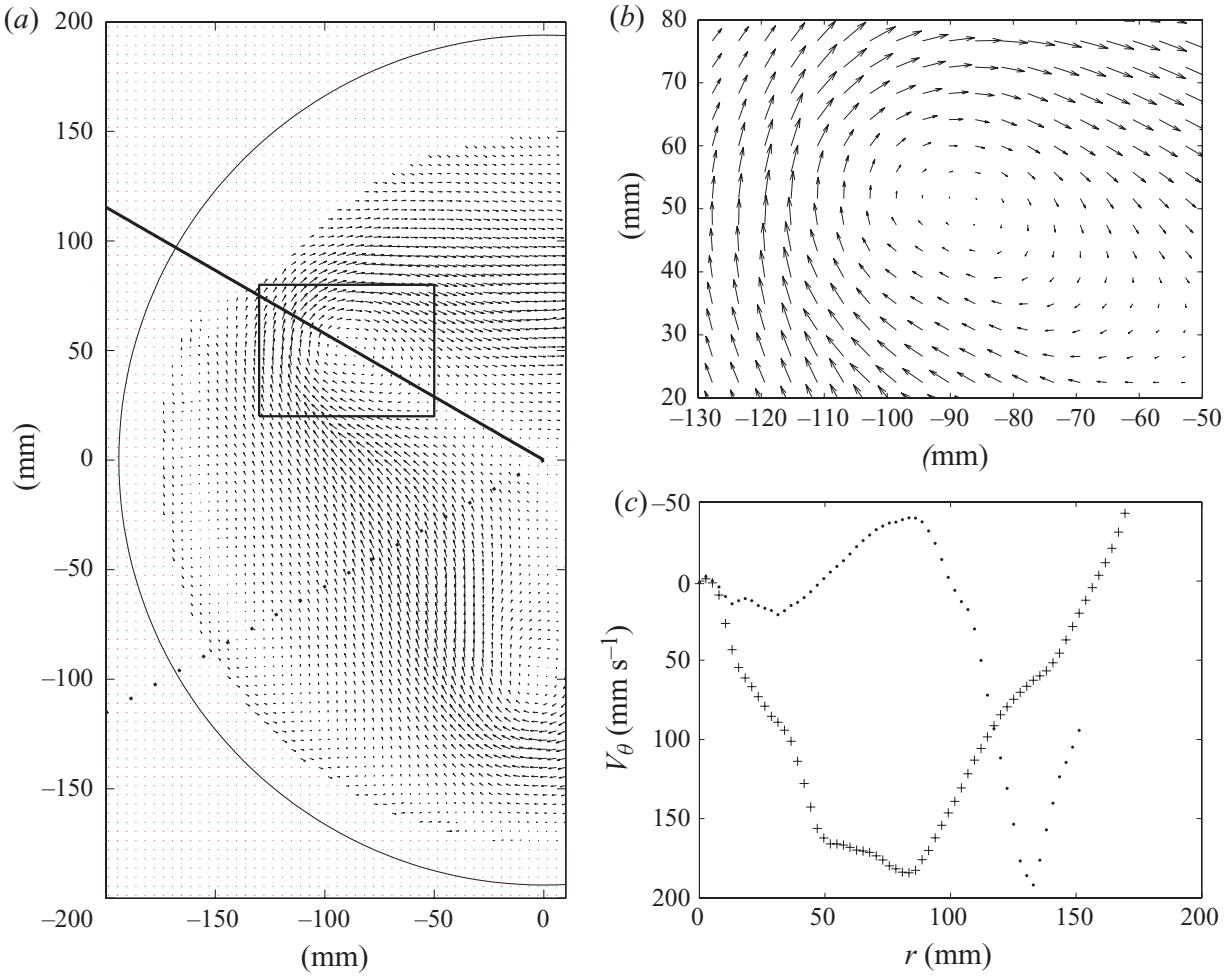

FIGURE 8. (*a*) The surface flow in the frame co-rotating with the polygon. The rotation rate of the polygon is measured from the movie and subtracted as a solid body rotation from the flow field of figure 7(*a*). (*b*) Zoom of the region of one of the polygon arms. The vortices in the arms are now apparent. (*c*) The azimuthal flow as given in (*a*) along the solid line (dots) and the dashed line (crosses). The subtracted figure rotation rate is 2.44 rad s^{-1} (0.39 Hz).

result can be obtained by adding oil near the contact line. Oil added in the bulk has no effect, so the destruction of the polygon is not a surface tension effect.

To summarize our understanding of the polygon formation process, we have shown that a common route to their formation is via an almost stable circular state, which is universal (i.e. independent of initial conditions) and from which a linear instability leads towards the polygon state in analogy with low-dimensional dynamical systems. A better understanding of the circular states is therefore crucial, and we give a theoretical description of these states in the following section. For the polygons, at least as long as they are 'wet', we have found that concentrated vorticity (or 'vortices') do occur in agreement with expectations (Jansson *et al.* 2006; Vatistas *et al.* 2008). However, analysing the flow in terms of point vortices does not lead to the right rotation rates. Indeed, we expect that the system is much more complicated than a system of point vortices in a two-dimensional fluid, due to the free surface and the way in which the system is driven. Finally, we have seen that, even though surface tension is not an important parameter, perturbations of the flow in the vicinity of the contact line can destroy the polygons.

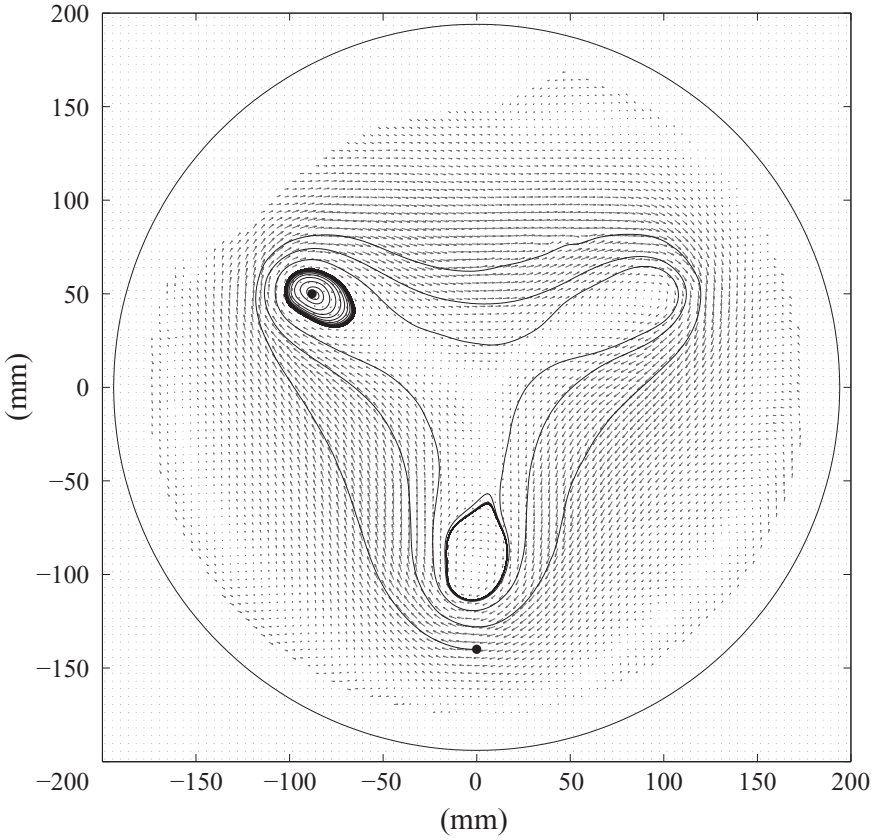

FIGURE 9. Streamlines computed for the PIV data. The trajectories start at the closed circles located at $(0, -141)$ and $(-87, 51)$ mm, and spiral inwards into the vortices from the outside but outwards from the vortex cores. The slow inward motion is consistent with the observation that particles which are initially spread over the entire surface slowly aggregate in the region around the vortices as shown in figure 6 and with the radial motion for the circular state as shown in figures 11 and 12. For very slow motion (e.g. in the vortex cores), one has to keep in mind, however, that the particles are lighter than water, and one must be cautious when inferring streamlines directly from their motion.

5. Theory of surface shape and velocities for the circular state

As we have seen, states with rotational symmetry are important since they are apparently the starting point for the instability which leads to the polygon states. In the following, we shall analyse the surface flows for such circular states. Tophøj (2009) has suggested an analytical method, whereby one can extract information about the velocity field on the free surface from the surface shape, when the effect of viscosity can be neglected. The theory deals with the surface flow on a free surface which is stationary in some (possibly rotating) frame of reference. In the following, we shall derive the basic equations in the rotationally symmetric case and compare the theoretical predictions to measurements. The surface profile of the symmetrical states is relatively easily measured in our set-up by using side-view photos, which are undistorted thanks to the outer rectangular casing. This information is then used to predict the velocities on the free surface theoretically, a prediction which can then be compared to PIV measurements. The theory is purely inviscid, so we assume that viscous effects are restricted to thin boundary layers and that the flow on the surface is dominated by convective momentum transfer. This is partially justified by the high Reynolds numbers (with $Re = R^2\Omega/\nu$, we typically get $Re \sim 500\,000$), but the validity will ultimately be determined by its predictive power.

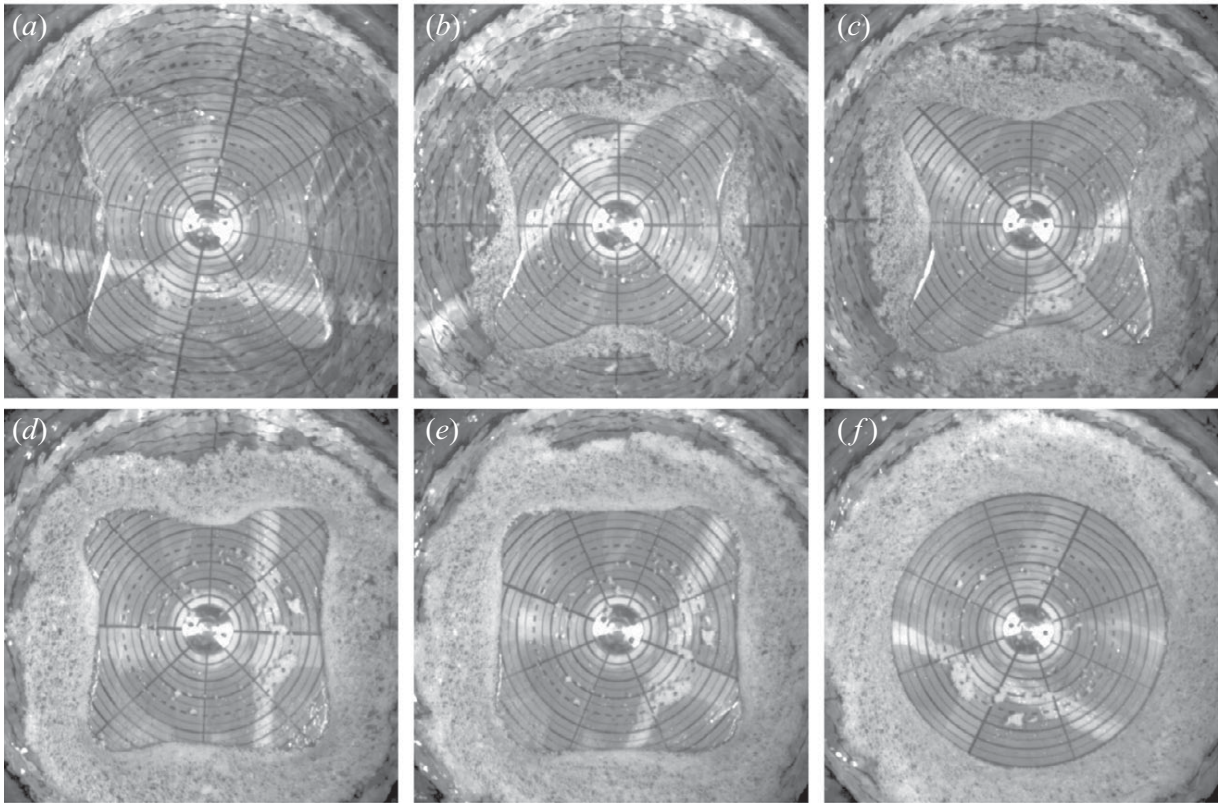

FIGURE 10. A square mode with $H = 3$ cm and $f = 2.4$ Hz with increasing amount of roughly 1 mm polystyrene particles floating on the surface. (*a*) Without particles, (*b*) 0.60 g, (*c*) 1.20 g, (*d*) 2.40 g, (*e*) 3.00 g and (*f*) 3.60 g. The particles obstruct the surface flow and strongly affect the resulting free surface shape.

5.1. *Projecting the Euler equations onto the surface*

To study the surface flow, the Euler equations are projected onto the local tangent plane of the free surface. Using the kinematic and dynamic boundary conditions, one then eliminates all derivatives transverse to the surface and obtains two partial differential equations for the two flow components in the local surface plane. Remarkably, the surface flow decouples from the bulk flow as shown by Tophøj (2009).

The time-independent Euler equations can be written as

$$\frac{1}{2}\nabla \boldsymbol{v}^2 + \omega \times \boldsymbol{v} = -\frac{1}{\rho}(\nabla p + \nabla \phi), \tag{5.1}$$

where $\phi = gz$ is the gravitational potential, ρ is the constant fluid density and ω is the vorticity. Projecting this equation onto a tangent vector $\boldsymbol{t}$ along the free surface, we get

$$\boldsymbol{t} \cdot \nabla \left(\tfrac{1}{2}\boldsymbol{v}^2 + gh\right) + \boldsymbol{t} \cdot (\omega \times \boldsymbol{v}) = 0, \tag{5.2}$$

where the pressure term drops out since the dynamic boundary condition ensures that the pressure is constant on the free surface (neglecting surface tension).

In cylindrical coordinates (r, θ, z) (with the z-axis vertically upwards) we denote the velocity components as $\boldsymbol{v} = \boldsymbol{e}_r V_r + \boldsymbol{e}_\theta V_\theta + \boldsymbol{e}_z V_z$. For a rotationally invariant flow, there is no dependence on θ and the surface profile is given by $z = h(r)$. Projecting along the radial direction along the surface means that we must choose $\boldsymbol{t} = \boldsymbol{t}_r = \boldsymbol{e}_r + h'\boldsymbol{e}_z$, where h' denotes the derivative of the height profile with respect to r. Thus, $\boldsymbol{t}_r \cdot \nabla = \mathrm{d}/\mathrm{d}r = \partial/\partial r + h'\partial/\partial z$, where the total derivative is taken along the free surface,

i.e. at $z = h(r)$. Further, we use the kinematic boundary condition, $V_z = h' V_r$, to get $-\boldsymbol{t}_r \cdot (\omega \times \boldsymbol{v}) = V_\theta((\partial/\partial r) + h'(\partial/\partial z))V_\theta + (V_\theta^2/r) = (\mathrm{d}V_\theta^2/\mathrm{d}r)/2 + (V_\theta^2/r)$ and the projected equation

$$\frac{\mathrm{d}}{\mathrm{d}r}\left(\frac{1}{2}(V_r^2 + V_z^2) + gh\right) - \frac{V_\theta^2}{r} = 0. \tag{5.3a}$$

Similarly, projecting along the tangent vector $\boldsymbol{t}_\theta = \boldsymbol{e}_\theta$, using $\boldsymbol{t}_\theta \cdot \nabla = 0$, only the rightmost term in (5.2) is non-zero. Using $\boldsymbol{t}_\theta \cdot (\omega \times \boldsymbol{v}) = V_r/r((\partial/\partial r) + (h'\partial/\partial z))(rV_\theta)$, we find

$$\frac{V_r}{r}\frac{\mathrm{d}}{\mathrm{d}r}(rV_\theta) = 0. \tag{5.3b}$$

5.2. *The surface flow in terms of the surface velocities u and v*

Thanks to the cylindrical symmetry, we can characterize the surface flow by the surface velocity components u and v defined *on* the surface by $u(r) = V_r\sqrt{1+(\mathrm{d}h/\mathrm{d}r)^2} = \pm\sqrt{V_r^2 + V_z^2}$ and $v(r) = V_\theta$. With this notation, (5.3) can be written in the concise form

$$\frac{\mathrm{d}}{\mathrm{d}r}\left(\frac{1}{2}u^2 + gh\right) - \frac{v^2}{r} = 0, \tag{5.4a}$$

$$u\,\frac{1}{r}\,\frac{\mathrm{d}}{\mathrm{d}r}(r\,v) = 0. \tag{5.4b}$$

This is a set of nonlinear first-order ODEs for the flow velocities $u(r)$ and $v(r)$ on the surface, and we shall solve them on the annulus $r_1 < r < r_2$. As usual, when dealing with inviscid flow theory, we shall use the Dirichlet boundary conditions of impenetrable domain boundaries, i.e. $u(r_1) = u(r_2) = 0$ with no *a priori* specification of v. The solutions to (5.4*b*) are of two types, which are discussed in the following.

In the case of vanishing secondary flow, $u = 0$, (5.4*b*) is automatically satisfied, and (5.4*a*) gives the familiar expression $g\,h' = v^2/r$. The classic Newton's bucket is a special case with rigid body rotation of the fluid, $v = \Omega r$, yielding $h = \Omega^2 r^2/2\,g +$ constant.

A less trivial case arises when there is a finite secondary flow, $u \neq 0$. Then (5.4*b*) leads to

$$v(r) = \frac{\Gamma}{r}, \tag{5.5a}$$

with constant Γ, a purely azimuthal flow that corresponds to the flow induced by a line vortex of circulation $2\pi\Gamma$ centred on the z-axis. This can be understood as follows: particles moving on the surface must, in the absence of viscosity and deviations from cylindrical symmetry, conserve their angular momentum. When u is finite, they carry their angular momentum to other radii and this generates the line-vortex flow. Now (5.5*a*) can be inserted into (5.4*a*) yielding $\mathrm{d}/\mathrm{d}r\left[(u^2 + v^2)/2 + gh\right] = 0$, with the Bernoulli equation

$$u^2 = C - \frac{\Gamma^2}{r^2} - 2gh, \tag{5.5b}$$

as an obvious first integral. Here C is a constant of integration fixed in the entire domain corresponding to the lack of vorticity in the line vortex solution (5.5*a*). Using the boundary conditions, $u_s(r_1) = u_s(r_2) = 0$, and the height profile $h(r)$, one finds C and Γ^2, specifying the flow velocities except for the signs, which must be inferred from considerations beyond inviscid theory. Denoting the integrated height change

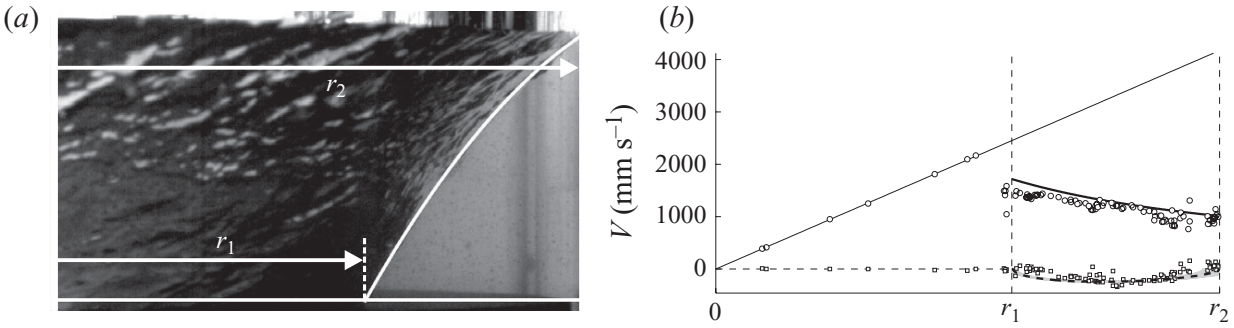

FIGURE 11. (*a*) Side-view photograph of a symmetric height profile and a dry centre region ($f = 3.42$ Hz, $H = 3.9$ cm). The plate, marked by a white horizontal line, rotates with angular frequency $\Omega = 2\pi f = 21.5$ rad s^{-1}. The inner radius of the wet region is $r_1 = 11.4$ cm and the outer (cylinder) radius is $r_2 = R = 19.4$ cm. The height of the fluid layer at the outer edge is $\Delta h = 9.7$ cm. The corresponding parameters in the velocity solution (see (5.6)) are $C = 2.9\,\mathrm{m^2\,s^{-2}}$ and $\Gamma = \pm 0.20\,\mathrm{m^2\,s^{-1}}$. The white curve is a quadratic fit to the height profile with $\mathrm{d}^2h/\mathrm{d}r^2 = -(31\,\mathrm{cm})^{-1}$. (*b*) Plot of the flow velocities as computed from (5.5) compared with PIV data points (circles for azimuthal and squares for radial flow). The solid curve on the right of the vertical dashed line at r_1 is the azimuthal flow velocity $v = \Gamma/r$ computed from r_1, r_2 and Δh. The dashed curve on the right of r_1 is the horizontal projection of the radial surface velocity $V_r = u/\sqrt{1+h'^2}$ computed from the full fit of the height profile. The uncertainty for V_r (not shown) is $120\,\mathrm{mm\,s^{-1}}$ given a measurement uncertainty of 1 mm on the local height. The solid and dashed curves on the left of the vertical dashed line at r_1 are the local bottom plate velocities shown in the dry region ($V_r = 0$ and $V_\theta = \Omega r$). The PIV velocity measurements have an uncertainty interval of approximately $50\,\mathrm{mm\,s^{-1}}$ and correspond well to the analytic solutions of (5.4).

across the annulus by $\Delta h \equiv h(r_2) - h(r_1)$, the velocity coefficients are

$$C = 2g\,\Delta h\,\frac{{r_2}^2}{{r_2}^2 - {r_1}^2}, \quad \Gamma = \pm r_1\sqrt{C}. \tag{5.6}$$

Note that the azimuthal flow $v(r)$ is determined by the parameters r_1, r_2 and Δh alone, whereas the secondary radial flow $u(r)$ depends on the full height profile $h(r)$; see (5.5b).

5.3. *Analysis of experiments*

For high rotation frequencies of the driving bottom plate, the flow settles in a symmetrical state with a dry region in the centre of the bottom plate. Figure 11(*a*) shows an experiment with flow on the annulus $r \in (r_1, r_2)$ and a symmetric height profile. From the above analysis, the flow velocities can be taken from (5.5) with the coefficients given by (5.6). The flow directions are not determined by the inviscid theory, (5.4), and must be inferred from simple physical arguments accounting for viscous effects: the azimuthal flow is in the direction of rotation of the driving plate, and the secondary radial flow must be directed inwards at the surface due to Ekman pumping in the bottom boundary layer, which pushes fluid radially outwards at the bottom, and a Stewartson layer along the cylinder sides, where the fluid is pushed up (for discussion of general aspects of rotating flows, spin-up and the relevant boundary layers, see Hopfinger 1992). The resulting velocities are shown in figure 11(*b*) together with the result of a PIV measurement. The velocities predicted by (5.5) correspond well to the measured values. The viscous boundary layers are not visible in the PIV measurement and this supports the assumptions that we have made.

For very low driving frequencies, the system enters a different symmetrical state, a wet state where the free surface is only weakly disturbed from the hydrostatic

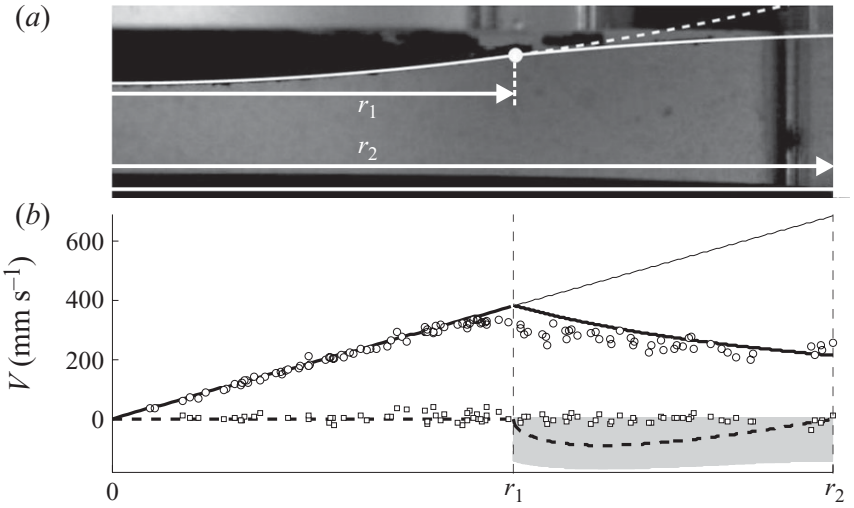

FIGURE 12. (*a*) Side-view photograph of a symmetric height profile and a wet bottom plate ($f = 1.78$ Hz, $H = 3.6$ cm). The plate, marked by a white horizontal line, is rotating with angular frequency $\Omega = 2\pi f = 3.53\,\mathrm{rad\,s^{-1}}$. The solid white curve shows a fit of the surface profile. The white dot at $r = r_1 = 10.8$ cm marks the transition between two different regions. To the left, the surface corresponds to rigid body rotation with the corresponding height profile $h = r^2\Omega^2/2g + \text{constant}$. To the right of the transition point, the observed height profile starts to deviate appreciably from the rigid body curve (continued as the dashed white line). There, the surface profile $h(r)$ is approximated by a quadratic curve with $\mathrm{d}^2h/\mathrm{d}r^2 = -(1.7\,\mathrm{m})^{-1}$. The cylinder radius is $r_2 = 19.4$ cm. The measured integrated height difference is $\Delta h \equiv h(r_2) - h(r_1) = 0.52$ cm. The corresponding velocity parameters for the flow exterior to r_1 are $C = 0.15\,\mathrm{m^2\,s^{-2}}$ and $\Gamma = \pm 0.042\,\mathrm{m^2\,s^{-1}}$. (*b*) Plot of the flow velocities as computed from (5.5) compared with PIV data points (circles for azimuthal and squares for radial flow). The solid curve is the azimuthal flow velocity v. In the region exterior to r_1, v is computed by (5.5*a*) from r_1, r_2 and Δh, and in the region interior to r_1 (the left vertical dashed line), v is taken as the plate rigid body rotation $v = \Omega r$. Note that the two branches of the solid curve are computed from different measurements and yet they match almost perfectly at $r = r_1$. The dashed line gives the predicted radial velocity component. The shaded region marks the uncertainty region for the radial surface velocity $u/\sqrt{1 + h'^2}$ given a measurement uncertainty of 1 mm on the local surface height.

flat shape and the fluid region covers the entire bottom plate. Figure 12(*a*) shows an experiment with a symmetric height profile and a completely wet bottom plate. Because of the different boundary conditions on the bulk flow that apply on the rotating bottom and on the stationary sidewall, boundary layers must exist in some region of the bottom plate and hence also a secondary radial component of the flow ($u(r) \neq 0$ for some r). However, the line-vortex flow (5.5*a*) and the corresponding singularity at $r = 0$ in (5.5*b*) are inconsistent with the observed surface profile, which is regular at the centre. It is therefore tempting to speculate that the flow consists of two regions with different solutions to (5.4). The transition is assumed to take place on a circle given by $r = \text{constant} \equiv r_1$. In the interior region, $r < r_1$, the flow follows the bottom plate in synchronized rigid body motion. Synchronization is necessary to prevent the formation of a bottom boundary layer and consequently a secondary flow. In the exterior region the secondary flow is finite, and the flow velocities are of the type given in (5.5). In order to locate the transition radius r_1, the surface profile is compared to that of synchronized rigid body rotation $h = r^2(\Omega^2/2g) + \text{constant}$. The surface profile fits this shape well for radii below r_1, where it starts to deviate appreciably; see figure 12(*a*). The measured velocity of a tracer particle in this region

closely fits the corresponding plate velocity, supporting the hypothesis of synchronized rigid body rotation.

Exterior to the transition point r_1, i.e. for $r_1 < r < r_2$, where $r_2 = R$ is the container radius, the surface profile $h(r)$ is approximated by a straight line. The resulting fluid velocities are shown in figure 12(*b*). Note that the predicted velocities at the transition point match very well, even though they are determined by independent measurements. The velocity on the left, $v(r)|_{r\uparrow r_1}$, is computed from r_1 and the plate angular frequency Ω, while the velocity on the right, $v(r)|_{r\downarrow r_1}$, is computed from r_1, r_2 and Δh. This compelling result suggests that the system adjusts the position of the transition so as to match the azimuthal flow in the interior and exterior regions. The synchronization is a viscous effect which enters into (5.4) through the observed height profile $h(r)$. So the inviscid assumptions leading to (5.4) can lead to a sensible description of the surface flow of the experiment, even though viscous forces are responsible for the selection of the realized flow parameters.

Similar flows were observed in a numerical simulation by Lopez *et al.* (2004), albeit for a much lower Reynolds number, $Re \approx 1400$–2000, where the free surface was assumed planar and modelled by a symmetry plane. In particular, their figures 2 and 3 share the main features of the rotationally symmetric flows described above. They may be described approximately as having a central region of synchronized rigid body rotation surrounded by an annular region of nearly irrotational flow. The resemblance is most pronounced in the shallow-water flow in their figure 2. In both cases, weak secondary flows are observed in the central region, but, as discussed above, their strength depends sensitively on the exact shape of the free surface.

6. Conclusion

We have provided new experimental and theoretical results on the rotating polygons found in free-surface flows. We have seen that the symmetry-breaking transition can have the characteristics of a low-dimensional linear instability along a unique unstable manifold out of an almost stable rotationally symmetric state. Further, the wet polygons (triangles) clearly show vortex structures, but a point vortex model alone is insufficient to account for the flow or the rotation rate of the polygon. Finally, we have analysed the rotationally symmetric shapes theoretically and found that the surface flow should be well described as a Rankine vortex so that even the wet circular states have a singular circle inside which the flow is a rigid rotation with no secondary flow. These states should be important for a subsequent analysis of the instabilities leading to the polygonal states.

REFERENCES

Aref, H., Newton, P. K., Stremler, M. A., Tokieda, T. & Vainchtein, D. L. 2003 Vortex crystals. *Adv. Appl. Mech.* **39**, 1–79.

Godfrey, D. A. 1988 A hexagonal feature around Saturn's north pole. *Icarus* **76**, 335–356.

Hirsa, A. H., Lopez, J. M. & Miraghaie, R. 2002 Symmetry breaking to a rotating wave in a lid-driven cylinder with a free surface: experimental observation. *Phys. Fluids* **14**, L29–L32.

Hopfinger, E. J. 1992 In *Rotating Fluids in Geophysical and Industrial Applications* (ed. E. J. Hopfinger). Springer.

Jansson, T. R. N., Haspang, M. P., Jensen, K. H., Hersen, P. & Bohr, T. 2006 Polygons on a rotating fluid surface. *Phys. Rev. Lett.* **96**, 174502.

Lopez, J. M., Marques, F., Hirsa, A. H. & Miraghaie, R. 2004 Symmetry breaking in free-surface cylinder flows. *J. Fluid Mech.* **502**, 99–126.

Miraghaie, R., Lopez, J. M. & Hirsa, A. H. 2003 Flow induced patterning at the air–water interface. *Phys. Fluids* **15**, L45–L48.

Poncet, S. & Chauve, M. P. 2007 Shear-layer instability in a rotating system. *J. Flow Vis. Image Process.* **14**, 85–105.

Rabaud, M. & Couder, Y. 1983 A shear-flow instability in a circular geometry. *J. Fluid Mech.* **136**, 291–319.

Suzuki, T., Iima, M. & Hayase, Y. 2006 Surface switching of rotating fluid in a cylinder. *Phys. Fluids* **18**, 101701.

Tasaka, Y. & Iima, M. 2009 Flow transitions in the surface switching of rotating fluid. *J. Fluid Mech.* **636**, 475–484.

Tophøj, L. 2009 Private communication.

Vatistas, G. H. 1990 A note on liquid vortex sloshing and Kelvin's equilibria. *J. Fluid Mech.* **217**, 241–248.

Vatistas, G. H., Wang, J. & Lin, S. 1992 Experiments on waves induced in the hollow core of vortices. *Exp. Fluids* **13**, 377–385.

Vatistas, G. H., Wang, J. & Lin, S. 1994 Recent findings on Kelvin's equilibria. *Acta Mech.* **103**, 89–102.

Vatistas, G. H., Abderrahmane, H. A. & Kamran Siddiqui, M. H. 2008 Experimental confirmation of Kelvin's equilibria. *Phys. Rev. Lett.* **100**, 174503.

J. Fluid Mech. (2012), *vol.* 691, *pp.* 605–606.
doi:10.1017/jfm.2011.492

ERRATUM

Polygon formation and surface flow on a rotating fluid surface – ERRATUM

R. Bergmann, L. Tophøj, T. A. M. Homan, P. Hersen, A. Andersen and T. Bohr

doi:10.1017/jfm.2011.152, Published by Cambridge University Press, 24 May 2011

Our recent paper Bergmann *et al.* (2011) on polygon states on a rotating fluid surface contained a few typographical errors as well as an imprecise statement about the feasibility of point vortex models for the flows under consideration. In the following, we shall correct these shortcomings.

(*a*) In (4.1) on p. 422, there is a superfluous R, and r_v should have been R_v – the distance of the vortex from the rotation axis. The equation should thus read

$$\Omega = \frac{\Gamma}{2\pi R_v^2} \approx 0.26 \,\frac{\text{rad}}{\text{s}}. \tag{4.1}$$

In the calculations, the correct formula was used, so the result of (4.1) remains valid. Two lines above this equation, r_v also appears and again it should be replaced by R_v.

(*b*) At the bottom of page 421 we write: 'it has been speculated that the flow may be described by a simple point vortex model; see Vatistas et al. (2008)'. Having identified three point-like vortices on the fluid surface, we compute (using (4.1)) the rotation rate of three point vortices in an otherwise irrotational 2d fluid, and conclude that it is an order of magnitude smaller than the observed rotation rate. We then continue: 'refining the model by introducing image counter-rotating vortices outside the cylinder so as to satisfy the no-penetration boundary condition at the cylinder wall does not improve matters much. The inclusion of image vortices leads to a relative increase of the predicted angular velocity (4.1) by about 30 %, which is still far too low. Thus the motion of the vortices is only to a small degree influenced by the advection from the other vortices and must be subjected, in addition, to a strong background velocity field. A Hamiltonian model of point vortices in an otherwise potential flow would capture neither the observed rotation velocities nor the spiralling effects seen in figure 9'.

The last statement is somewhat sweeping. We can of course not conclude that a general point vortex model is not feasible. All we can say is that a point vortex model with only $N = 3$ point vortices (plus images) in an otherwise irrotational flow is insufficient to account for the flow or the rotation rate of the polygon. Other vortices, e.g. a strong central vortex, might be necessary. To substantiate this, it would have been helpful to include additional data from our surface flow measurements, and we

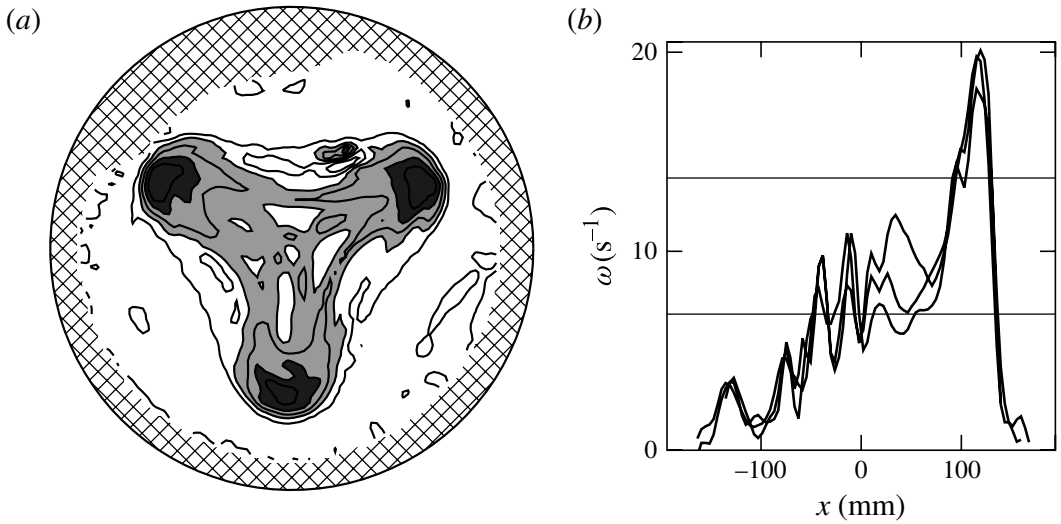

FIGURE 1. (*a*) Vorticity contours in the lab frame. Each of the 'point' vortices have strengths around 0.025 $\mathrm{m}^2\ \mathrm{s}^{-1}$, where the sign of ω is chosen as positive for clockwise rotation. Their centers are 110 mm from the center of the container (the rotation axis) and their radii are around 20 mm. The circulation inside a disk of radius 90 mm (the 'inner area') is around 0.18 $\mathrm{m}^2\ \mathrm{s}^{-1}$, which corresponds well to the observed rotational velocity of the triangle-shaped surface deformation. The contour lines show levels of ω in units of $\omega_{max}/6$. The light grey areas have $2\omega_{max}/3 > \omega > \omega_{max}/3$ and the dark grey has $\omega > 2\omega_{max}/3$, where $\omega_{max} = 20.5\ \mathrm{s}^{-1}$. (*b*) Clockwise vorticity in the lab frame as function of distance (in mm) from the rotation axis on a ray passing through a vortex to the right and the midpoint between two vortices on the left. The three different curves each pass through one of the three different vortices. The vorticity is computed from the data used for figures 7–9 in Bergmann *et al.* (2011) and a slight spatial smoothing has been applied.

shall amend this by showing the present figure 1. The figure shows (*a*) the vorticity ω (in the lab frame) on the entire fluid surface and (*b*) the vorticity as function of distance from the rotation axis on the three rays passing through the centres of the vortices. The three point-like vortices are clearly visible and have a vorticity of the order of twice the largest vorticity elsewhere. In addition, there is a 'plateau' of vorticity between the rotating vortices, whereas the vorticity is basically zero outside. Whether this can be successfully modelled in terms of point vortices, will be left to the judgement of the readers and future researchers.

Acknowledgements

We would like to thank G. Vatistas for pointing out the error in (4.1) and questioning our arguments on point vortex models.

REFERENCES

BERGMANN, R., TOPHØJ, L., HOMAN, T. A. M., HERSEN, P., ANDERSEN, A. & BOHR, T. 2011 Polygon formation and surface flow on a rotating fluid surface. *J. Fluid Mech.* **679**, 415–431.

A model of the rotating polygon experiment using conservation of angular momentum

Laust Tophøj & Tomas Bohr

March 14, 2012

This paper discusses the modelling of the "rotating polygon experiment" using the conservation of angular momentum. The experiment is described in [Jansson *et al.* (2006)]. We shall refer to the data from [Jansson *et al.* (2006)] as well as more recent experiments by Antoine Fruleux and Bjarne Bach, cf. [Fruleux (2010)] and [Bach (2011)]. The setup consists of a cylindrical bucket with vertical side walls, partially filled with a fluid, typically water. The bucket is so designed as to allow the independent rotation of the bottom plate and the side wall, both of which have smooth surfaces, by electrical motors. Care is taken to keep the whole thing symmetric under rotations. An experiment is performed by pouring a controlled volume of fluid into the bucket and then setting the two control surfaces to rotate at constant angular velocities. The flow is typically turbulent, with Reynolds numbers of the order 10^4.

As the primary method of observation we look at the deformation of the free surface. This is typically a depression of the surface around the axis of rotation, caused by centrifugal forces on the rapidly rotating fluid. For some control parameters, one sees "wet states", where the surface depression does not extend all the way to the bottom plate. For other control parameters, one sees "dry states", where the central part of the bottom plate is almost completely drained of fluid, with the fluid occupying a roughly toroidal volume near the edge between the bottom plate and the side wall. The experiment and some dry states are shown in figure 1. We note that the "dry" region of the plate is in many cases covered by a thin film of fluid, but we believe this to play a minor role in the flow dynamics, and we shall denote the curve separating the "dry" region from the region under the bulk fluid mass as the *contact line*. Throughout this paper, we restrict our attention to dry states.

Figure 1: *The rotating polygon experiment. To the left, a side view of the running experiment is given, showing a dry triangular state. The plexiglass bottom plate is clearly visible, and the fluid occupies the roughly toroidal volume under the free surface. The corrugated surface is a sign of the highly turbulent flow. In this setup, used by [Jansson et al. (2006)], the bottom plate rotates, while the side wall is stationary. To the right, a top-down view shows the polygon character of a few dry states. Starting from the top, we see a pentagon, a square and a triangle. The pictures are reprinted from [Jansson et al. (2006)].*

Now, one might expect to see a rotationally symmetric flow, and an associated symmetric deformation of the free surface. However, for a range of parameters, the flow breaks the symmetry, and the contact line is deformed into a sort of polygonal shape, for example an ellipse or a triangle shape with smooth corners. This shape rotates rather like a rigid body at a constant angular velocity, typically a fraction of the rotation speed of the fluid particles, as measured directly by injecting some visible marker into the fluid. Pictures of some polygon states are shown in figure 1.

We believe that the polygon states arise as a consequence of a symmetric state becoming unstable. This is supported in part by the findings in
[Bergmann *et al.* (2011)], where the observed evolution of states was discussed from a dynamical systems point of view. With this in mind, an understanding of the symmetric states becomes central in any analysis of the rotating polygon experiment. For if the polygon states arise by dynamical evolution of a symmetric "parent" state, we might expect the properties of the polygon "child" state, e.g. the number of corners, to be determined by the properties of the parent state.

In the next section, we proceed to construct a model, which predicts the shape of the symmetric equilibrium state associated with a given set of control parameters. The model is based on the conservation of angular momentum, by viewing the fluid volume in the experiment as a conduit, serving to transport angular momentum, received from the rapidly rotating bottom plate and then deposited on the slower side wall. Then, an important criterion for equilibrium is that the amounts of angular momentum received and deposited must be identical. The sketch shown in figure 2 illustrates this line of thought, if we think of the contact areas to the bottom and side walls as dynamically adjustable. We might say that the fluid adjusts its shape so as to be in equally strong contact with the two control surfaces. If the contact with the fast bottom plate is stronger than that with the slow side wall, the fluid accelerates as a consequence, which in turn by centrifugal forces causes the fluid to settle into a steeper shape, with a stronger contact to the side wall and a weaker contact to the bottom plate. If, on the other, the fluid volume is too steep, the opposite happens.

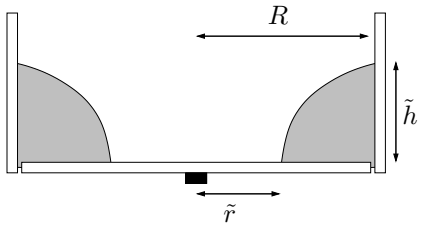

Figure 2: Sketch of the setup. The fluid velocity at the scaled radius r is called $\tilde{U}(r)$, the bottom plate velocity $\tilde{V}(r)$ and the cylinder wall velocity $\tilde{W}$. The filling depth in the still condition (flat water surface) is $H\tilde{R}$.

The model

We now introduce the model solely in terms of nondimensional parameters. Whenever a dimensional quantity does occur, we mark it by a tilde. Velocities are counted positive in the counterclockwise direction. The setup is sketched in figure 2. We nondimensionalize all lengths by the cylinder radius $\tilde{R}$ and all velocities by the velocity scale $(\tilde{g}\tilde{R})^{1/2}$, where $\tilde{g}$ is the gravity constant.

Based on the assumption that the turbulent motion thoroughly mixes the fluid, so as to keep the density of angular momentum approximately uniform, we take the flow velocity to be that induced by a single central line vortex. This simplistic description ignores a possible secondary flow in the poloidal direction as well as extended boundary layers. This is in part supported by the findings of [Bergmann *et al.* (2011)], where the velocity directly on the free surface was measured, revealing that the secondary flow is an order of magnitude weaker than the primary flow, and that the boundary layers near the walls are very thin, at least so far as the flow on the free surface is concerned. Thus, the nondimensional fluid velocity is $\tilde{U}(r) = r^{-1}U(\tilde{g}\tilde{R})^{1/2}$, where r is the nondimensional radius. So U is a nondimensional constant characterizing the fluid flow.

The velocity of the bottom plate is $\tilde{V}(r) = rV(\tilde{g}\tilde{R})^{1/2}$ and the velocity of the cylinder wall is $\tilde{W} = W(\tilde{g}\tilde{R})^{1/2}$. We take U and V to be positive as a convention. The total volume of fluid is also a control parameter, and we describe it by the number H, the non-dimensional filling height in the quiescent system, so that the total dimensional volume is $\pi\tilde{R}^2(H\tilde{R})$.

In summary, we have three control parameters: The bottom plate driving speed V, the side wall driving speed W and the filling height H. The state of the fluid is characterized by three numbers, the velocity variable U, the nondimensional fluid height h at the outer wall and the nondimensional radius of the contact line ρ.

The influx of nondimensional angular momentum, i.e. the moment exerted on the fluid by the control surfaces, is

$$M = \int_A \mathrm{d}A \;\; r\,\tau(r, U, V, W), \tag{1}$$

where the integral is over the entire solid boundary area A, and τ is the shear stress at the wall, which we count positive if it forces the fluid in the counterclockwise direction. Note that we have ignored a factor 2π in (1).

We now need to estimate the wall shear stress τ in (1). In rotating systems, there are several types of boundary layers, each with their different scaling on Reynolds number. However, because the Reynolds number is large, we expect the

fluid viscosity to be absent in our expression, an assumption also supported by the experiments of [Jansson *et al.* (2006)]. So we are left with rather few quantities that must together determine τ. Those are the boundary layer thickness, the constant fluid density $\tilde{\rho}_0$ and the velocity difference between the solid wall and the bulk flow, say $\tilde{u}$. On dimensional grounds, the boundary layer thickness drops out, and we must have a relation of the form

$$\tilde{\tau} \sim \tilde{\rho}_0 \tilde{u}^2. \tag{2}$$

These assumptions are discussed in further detail in [Landay & Lifshitz (1987)], §42-44, together with turbulent boundary layers and the well-known logarithmic velocity profile. Here, we assume that (2) applies to both solid boundaries, the bottom plate and the side wall, with the same constant of proportionality.

Now, we assemble (1) and (2), while ignoring a common factor, cf. the above discussion. In nondimensional terms, we get

$$M = -h(U-W)^2 + \int_\rho^1 \mathrm{d}r \, \left(Vr^2 - U\right)^2. \tag{3}$$

Here the first term gives the decelerating moment exterted by the side wall, and the second term with the integral is the accelerating moment exerted by the bottom plate. For consistency, we must assume $W < U$ and $U/r < Vr$ throughout the fluid volume $\rho < r < 1$, i.e. that the fluid motion U/r is faster than the side wall motion and slower than the bottom plate motion.

The moment given in (3) depends on the control parameters V and W as well as the unknown quantities U, ρ and h. Below, we proceed to obtain relations between the unknowns.

First, we obtain a relation giving $h = h(U, \rho)$: We can describe the shape of the free surface by simply balancing the centrifugal outward force on a fluid element with the gravitational pull tending to flatten the surface. In dimensional terms, we have $\tilde{g}\,\partial y/\partial \tilde{r} = \tilde{U}^2/\tilde{r}$, where $\tilde{y}$ is the surface elevation at a given radius $\tilde{r}$. Solving this equation in nondimensional terms with the boundary condition $y(\rho) = 0$, we have

$$y(r) = \frac{U^2}{2}\left(\frac{1}{\rho^2} - \frac{1}{r^2}\right),$$

and the height at the cylinder wall $h \equiv y(1)$ is

$$h = U^2 \frac{1-\rho^2}{2\rho^2}. \tag{4}$$

Secondly, we obtain a relation $U = U(H, \rho)$. By considering the total volume of water (recall that the nondimensional radius is equal to 1), we get

$$V = \pi H = 2\pi \int_{\rho}^{1} \mathrm{d}r \; ry(r) = \frac{\pi}{2} U^2 \left(\rho^{-2} - 1 - \log \rho^{-2} \right).$$

Rearranging, we find that

$$U^2 = 2H \left(\rho^{-2} - 1 - \log \rho^{-2} \right)^{-1} \equiv 2H \, A(\rho). \tag{5}$$

We are now ready to assemble the whole thing and put forward our equilibrium requirement

$$M = 0. \tag{6}$$

By inserting equations (3-5) into (6), we get a self-contained equation in for the unknown variable ρ, in terms of the control parameters V, W and H. Here it comes.

$$0 = -2HA(\rho) \frac{1 - \rho^2}{2\rho^2} \left(\sqrt{2HA(\rho)} - W \right)^2 + \int_{\rho}^{1} \mathrm{d}r \left(Vr^2 - \sqrt{2HA(\rho)} \right)^2. \tag{7}$$

This is a nonlinear equation in the unknown variable ρ, whose solution is a clear criterion for equilibrium in the balance of angular momentum. We stress that the model gives a simple answer, and has no tunable parameters. One can easily expand the integral and write (7) more explicitly, but we do not show the ugly expression here. Rather, we solve (7) numerically using $MATLAB$.

We remark that one needs to take care to satisfy the above-mentioned consistency relations, $U/r < Vr$ and $W < U$, in order that the signs on the shear stresses, which have been fixed by hand, remain correct. If, on the other hand, the fluid becomes faster than the bottom plate for some radii, the stress must be counted in the opposite sense. Of course one could easily include a procedure in the solution method to assign the proper sign in each term and at each radius in the integral in (7). However, the change of direction in the sign typically takes place in regions of the parameter space, other than those of interest, so we shall not go further into the matter here, except to say that the model predictions used in the following section have been produced using the correct signs in (7).

Note also that (7) is quadratic in the control parameters V and W. So we could have solved it analytically in terms of one of these parameters and express

the functional form, say $V(\rho, W, H)$ in a closed form. But we are more interested in the inverse problem of determining ρ as a function of the control parameters, and for that we need to use numerics.

Comparison to experiments

We can compare to the experiments performed by Antoine Fruleux, who measured ρ and h directly for a range of parameters H and V, while keeping $W = 0$ fixed, [Fruleux (2010)]. In some cases, when the observed states were in fact assymmetric, Antoine recorded their mean values, even though these might not be exactly identical to values corresponding to the associated symmetric "parent" state. The data have been imported into *MATLAB*, interpolated using the `v4` procedure and smoothed a bit using the `conv2` convolution procedure. Contour plots of the result are shown in figure 4 together with the result of the model. In figure 3, a plot of the measured variables on selected lines through the 2D control parameter space is shown from the same experiments. Note that in the figures, all quantities are in CGS units.

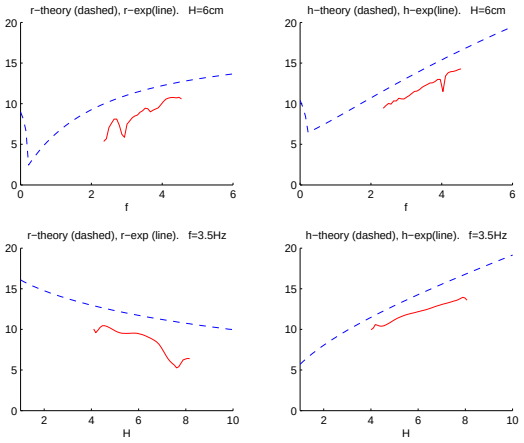

Figure 3: Comparison of model predictions and experimental results obtained by Antoine Fruleux. Some sections of the data shown in figure 4. In the top row, H is kept constant while V (f) is varied. In the bottom row, V (f) is kept constant while H is varied. The measurements are the red curves, while the dashed blue curves show the model results from (7). The model reproduces the general behaviour of ρ and h well, but apparently tends to overestimate both quantities.

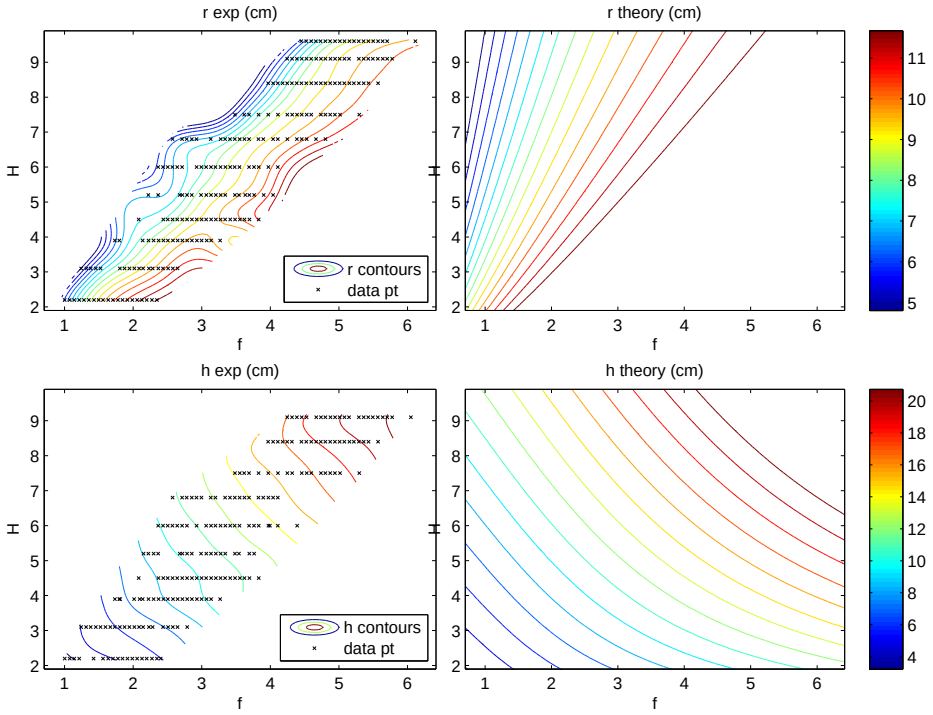

Figure 4: Comparison of model predictions and experimental results obtained by Antoine Fruleux. Dimensional quantities are given in CGS units. In each diagram, the horizontal axis shows the frequency f and the vertical axis shows the filling height H, which correspond to our nondimensional control parameters V and H. (Top Row): The mean radius ρ of the contact line. To the left, the experimental results are shown. The measurement points are marked by $\times$. To the right, the result of (7) is shown. The contours of both figures are colored according to the top color bar. (Bottom Row): The water level h at the wall. To the left, the experimental result is shown. The measurement points are marked by an (x). To the right, the theoretical prediction is shown. A reasonable agreement is seen, in particular in the bottom row. The values of h and ρ at selected lines through parameter space are shown in figure 3.

The data shown in figures 3 and 4 is in good agreement with the corresponding prediction made from (7).

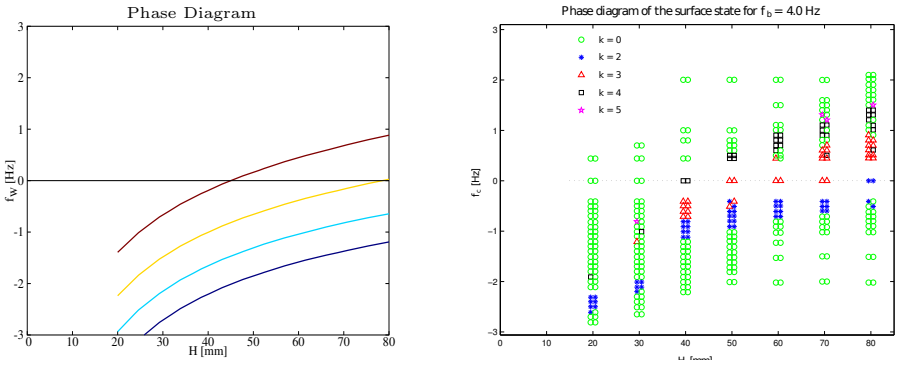

Figure 5: Phase diagram. The horizontal axes show the filling height H and the vertical axes show the frequency f_W corresponding to the side wall rotation W. The bottom plate is rotating at a fixed rate $f_V = 4\text{Hz} > f_W$. On the right, the markers show the occurence of various polygon states, cf. [Bach (2011)]. On the left, lines of constant ρ given by (7) are shown. The values range linearly from $\rho = 0.3$ (blue) to $\rho = .6$ (dark red). The curves separating different states in the phase diagram correspond qualitatively to the curves given by (7).

1 Connecting the predicted parameter ρ to the wavenumber selection

We have shown above, that we can predict the nondimensional wetting radius ρ for a symmetric state as a function of the control parameters, and that the result compares well to experiment, at least in the case $W = 0$. As mentioned in the introduction, we speculate that the properties of the symmetric state associated with a given set of control parameters somehow determine the properties of the actually observed polygon state. We now give some preliminary evidence to support this hypothesis.

We propose that the wavenumber n, i.e. the number of polygon corners, is determined simply as a function of ρ. This is reasonable, as ρ (or rather its dimensional counterpart) is pretty much the only length scale available to us. In the end, however, only experiments will tell us if the hypothesis is any good.

Figures 5 and 6 show various phase diagrams giving the occurence of polygon states in various sections of the parameter space from [Bach (2011)], together with lines of constant ρ as given by (7). In both figures, the lines of constant ρ

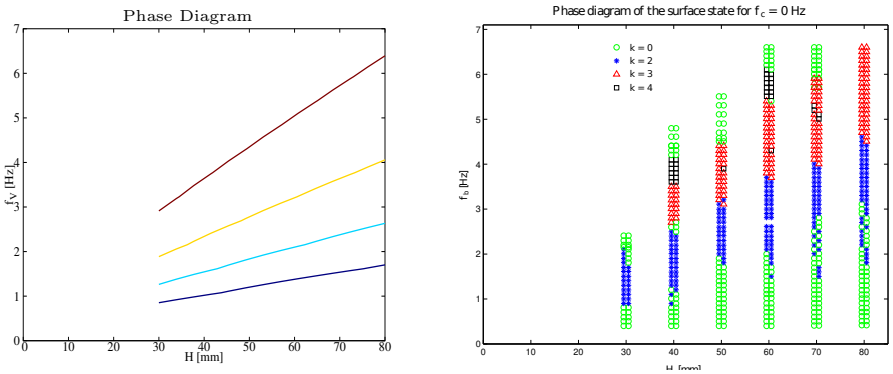

Figure 6: Phase diagram. The horizontal axes show the filling height H and the vertical axes show the frequency f_V corresponding to the bottom plate rotation V. The side wall is kept fixed $W = 0$. On the right, the markers show the occurence of various polygon states, cf. [Bach (2011)]. On the left, lines of constant ρ given by (7) are shown. The values range linearly from $\rho = 0.3$ (blue) to $\rho = .6$ (dark red). The curves separating different states in the phase diagram correspond qualitatively to the curves given by (7). Phase diagram, $\rho = 0.3$ (blue) to $\rho = .6$ (red). $f_W = 0Hz$.

behave in very much the same manner as the observed lines of transition between states. Furthermore, in both figures the same values of ρ appear to signal the same transitions observed in the experiment.

Figure 7 shows yet another slice through parameter space, this time with W being varied, allowing for a counterrotating side wall. Again the qualitative correspondence between experiment and (7) is good, except that the experiments show that two bands of polygon states exist in the phase diagram, with the "extra" band showing up when the side wall is strongly counterrotating. This is not reflected in the model predictions. We speculate that it is due to a fundamental change in the flow structure, with a counterrotating flow developing in a region near the side wall, with the polygon-forming flow effectively restricted to a smaller "effective" cylinder radius. Surely, such complicated flow structures cannot be described by our simplistic model. However, taken together, figures 5-7 strongly suggest that the above-mentioned hypothesis does give a useful link between knowledge on parent state properties and the wavenumber of the associated polygon state. This is encouraging, and perhaps it will help us in our future search for understanding the underlying instability mechanism.

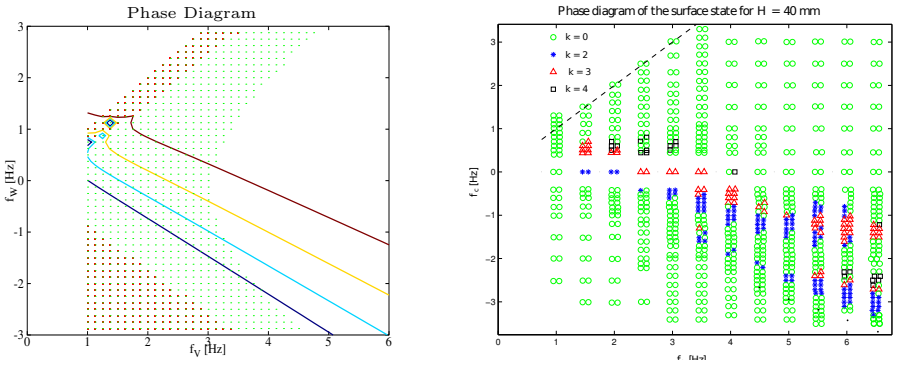

Figure 7: Phase diagram. The horizontal axes show the bottom plate rotation frequency f_V corresponding to the parameter V and the vertical axes show the side wall rotation frequency f_W corresponding to the parameter W. The filling height is kept constant with $\tilde{H} = 40$mm. On the right, the markers show the occurence of various polygon states, cf. [Bach (2011)]. On the left, lines of constant ρ given by (7) are shown. The values range linearly from $\rho = 0.3$ (blue) to $\rho = .6$ (dark red). The curves separating different states in the phase diagram correspond qualitatively to the curves given by (7), except for the extra band of polygons observed for a strongly counterrotating bottom plate (i.e. in the lowest part of the right panel). As explained in the text, we believe this to be a result of a more complicated flow structure, which is not captured by our simplistic model.

We note that phase diagrams like the ones we have shown here, ought to be given in terms of nondimensional parameters. It was noted by
[Jansson *et al.* (2006)] that the experiments for different cylinder radii give very similar results, which is hard to reconcile with the very direct scaling on $\tilde{R}$ implied by our model. We shall not go further into this discussion here, but rather postpone it to a future work.

2 Concluding remarks

Considering symmetric states in the rotating polygon experiment, we have seen that simple assumptions on the flow structure and on the nature of the boundary layers lead to a predictive model. The condition that the angular momentum be constant in a state of equilibrium was condensed into (7) allowing us to solve for the nondimensional wetting radius in terms of the control parameters. Comparing

to experiments, we saw that the model does a rather good job.

We have hypothesized that the wavenumber selection for polygon states depends on the properties of an associated symmetric "parent" state. Again, the predictions are in fair agreement with experimental results.

We expect to continue this work in the future, and we hope to connect the predictive power of the model presented here with an understanding of the instability causing a symmetric parent state to deform into a polygon state. Also, we wish to gain a better understanding of the scaling problem first observed by [Jansson *et al.* (2006)].

References

[Bach (2011)] Bach, B. 2011 Bachelor thesis: *Experimental Studies of Rotating Flows with a Free Surface.* DTU Physics, Technical University of Denmark.

[Bergmann *et al.* (2011)] Bergmann, R. & Tophøj, L. & Homan, T. A. M. & Hersen, P. & Andersen, A. & Bohr, T. 2011
Polygon formation and surface flow on a rotating fluid surface *J. Fl. Mech.* **679**, 415-431.

[Fruleux (2010)] Fruleux, A. 2010 Private communication.

[Jansson *et al.* (2006)] Jansson, T. R. N., Haspang, M. P., Jensen, K. H., Hersen, P. & Bohr, T. 2006 Polygons on a rotating fluid surface. *Phys. Rev. Lett.* **96**, 174502.

[Landay & Lifshitz (1987)] Landau & Lifshitz 1987 ***Fluid Mechanics, 2nd ed.*** Butterworth-Heinemann

Chapter 2

Point Vortex Dynamics: Chaotic Advection & Instability

The internal dynamics of fluid flow is extremely complicated, ranging from the simplest of lubrication problems to fully developed turbulence. In many cases, when the Reynolds number is small enough, it is useful to work in the limit of vanishing viscosity. Then the flow may be regarded as potential, except in regions of finite vorticity, with the vorticity in turn inducing a definite motion of the entire fluid. Approximating still further, we can consider all of this vorticity to be concentrated in singular vortex lines, whose dynamics occurs in a dramatically reduced phase space, while still preserving many of the features of a real high Reynolds number flow. In this chapter, I shall present some work on 2D flows within the framework point vortex dynamics.

It is well-known that a pair of vortices of opposite rotation tend to propagate along a straight line, analagously to a vortex ring blown by a smoker, or the little vortex pair that one can generate in a coffee cup with a teaspoon, famously termed the "Kaffeelöffelexperiment" by Felix Klein. If two such vortex pairs collide, they will eventually scatter off each other and move away along their new straight-line trajectories. The intermediate interaction, however, can be quite complicated. In particular, the scattering process is in some cases chaotic, with the scattering output (the angle between the outgoing pairs, say) depending sensitively on the scattering input.

I have been working on point vortex dynamics for a few years, beginning with my master thesis project done at DTU Physics and at Virginia Tech under the guidance of Hassan Aref. The main outcome of the project is summarized in the paper [Tophøj *et al.* (2008)], dealing with the chaotic scattering of vortex pairs. In the paper, we showed that even the scattering of two identical vortex pairs can be chaotic, with the intermediate dynamics consisting of various unstable periodic motions, such as perturbed periodic 3-vortex motions and the so-called leapfrogging motion. Leapfrogging is a situation, where two vortex pairs propagate along a common axis of symmetry, and the trailing pair is swept forward by the leading

pair in an alternating process, which is periodic in a co-moving frame of reference. We have continued to investigate various aspects of these problem, and two papers are included in this chapter.

Furthermore, I have been working on the problem of *weak scattering* of vortex pairs, i.e. a restriction of the above-mentioned problem to the limit where the pairs pass each other at a comfortable distance, so that various simplifying assumptions can be made about their interaction. I have suceeded in producing a valid analytical approximation to the scattering outcome, with the approximation error decaying like $|\rho|^{-6}$ in the distance of closest approach $|\rho|$. The method is new, and I hope to extend the work significantly before publication, so I have omitted the derivation from this thesis. However, I give a little preview in figure 2.1, showing a scattering diagram from [Tophøj *et al.* (2008)] as well as some of the recently developed approximation results.

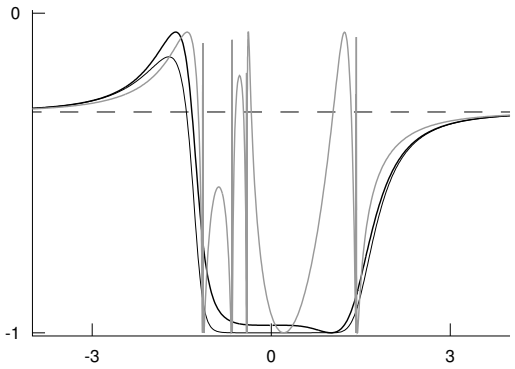

Figure 2.1: Scattering diagram for weak scattering of vortex pairs discussed in the text. The grey erratic curve is reproduced from figure 4 in [Tophøj *et al.* (2008)]. The plot shows a function of the scattering outcome as a function of the impact parameter $|\rho|$ defined in [Tophøj *et al.* (2008)]. On the vertical axis, the cosine of the angle between the outgoing pairs is shown. The black curves are different approximations, valid for weak scattering, that were recently developed. The thin black curve has an approximation error scaling like $|\rho|^{-6}$. The thick black curve is an energy-corrected version of the same approximation, made to exactly conserve the dynamical invariants associated with point vortex dynamics, but with the same order of error decay for large $|\rho|$.

Outline of chapter 2

On pp. 69-77 I include the short paper "Nonlinear excursions of particles in ideal 2D flows" by Hassan Aref, Johan Rønby, Mark Stremler and Laust Tophøj, published in Physica D, Nonlinear phenomena, cf. [Aref *et al.* (2011)]. The paper

discusses various examples of nonlinear advection, with the scattering of vortex pairs given as an example. My contribution to the paper is the technical background to the discussion of chaotic scattering as well as general discussion and helping with the preparation of the manuscript for publication.

Next, on pp. p. 79-89, I include the paper "Instability of vortex pair leapfrogging" by Laust Tophøj and Hassan Aref, submitted to Physics of Fluids on March 1, 2012. In the paper, we extend a work by [Acheson (2000)], who undertook a numerical investigation of the leapfrogging motion, finding both a stable and an unstable range of the one parameter characterizing the family of motions.

Physica D 240 (2011) 199–207

Contents lists available at ScienceDirect

Physica D

journal homepage: www.elsevier.com/locate/physd

Nonlinear excursions of particles in ideal 2D flows

H. Aref[a,d,*], J. Roenby[b,d], M.A. Stremler[a], L. Tophøj[c,d]

[a] Department of Engineering Science & Mechanics, Virginia Tech, Blacksburg, VA 24061, USA
[b] Department of Mathematics, Technical University of Denmark, Lyngby, DK-2800, Denmark
[c] Department of Physics, Technical University of Denmark, Lyngby, DK-2800, Denmark
[d] Center for Fluid Dynamics, Technical University of Denmark, Lyngby, DK-2800, Denmark

ARTICLE INFO

Article history:
Available online 26 August 2010

Keywords:
Particle motion
Ideal flow
Point vortex
Rigid body
Chaos

ABSTRACT

A number of problems related to particle trajectories in ideal 2D flows are discussed. Both regular particle paths, corresponding to integrable dynamics, and irregular or chaotic paths may arise. Examples of both types are shown. Sometimes, in the same flow, certain particles will follow regular paths while others follow irregular paths. Even in the chaotic region the amount of regularity or irregularity of a path depends on initial conditions and system parameters. The notion of a transported fluid region or "atmosphere" is mentioned. Various conclusions, ideas and queries are formulated based on the examples given. The intimate mix of regular and chaotic trajectories complicates a purely Lagrangian approach to fluid flow problems.

1. Introduction

It is well known that fluid dynamical problems may be approached using either the Lagrangian or the Eulerian representation. In a number of applications, fluid stirring and mixing problems in particular, the Lagrangian representation captures important information on the motion and distribution of individual particles. The appearance of chaotic particle trajectories, which is possible even in very simple flows, is an important phenomenon, both fundamentally and from the perspective of applications. We shall refer to the complex motions that passive particles, vortices, or rigid bodies interacting with their ambient flow undergo as *nonlinear excursions*. In this paper we summarize some of our experiences in this problem area by juxtaposing various examples. We work in an idealized "universe" that consists of 2D ideal flow, point vortices, freely moving rigid bodies (with slip boundary conditions) and passively advected particles. We survey a number of cases and formulate some conclusions that we hope may be of interest and applicability beyond our idealized flow situations.

It is a pleasure to dedicate this paper to Lou Howard on the occasion of his 80th birthday.

2. Advection

The simplest problem of the type under consideration is the motion of a passively advected particle in a prescribed flow. Equivalently, this problem addresses the kinematics of the flow itself since every particle of the fluid may be thought of as being passively advected by the flow of which it is a part. The potential complexity of this problem is immediately apparent by considering the case of 2D incompressible flow given by a streamfunction $\psi(x, y, t)$:

$$\frac{dx}{dt} = \frac{\partial \psi}{\partial y}, \qquad \frac{dy}{dt} = -\frac{\partial \psi}{\partial x}. \tag{2.1}$$

These equations are in the form of Hamilton's canonical equations for a one-degree-of-freedom system, with x and y as the conjugate variables and with the stream function, $\psi(x, y, t)$, playing the role of Hamiltonian. This identification derives from the incompressibility of the flow, and so pertains both to inviscid and viscous flows. The dissipative dynamics of a viscous fluid can still have "conservative" Hamiltonian kinematics so long as the fluid is incompressible.

A pair of conjugate variables in a Hamiltonian system are usually thought of as a "generalized coordinate" and a "generalized momentum". In the case of flow kinematics or advection both conjugate variables are coordinates of the advected particle. In this sense, as advection by an incompressible 2D flow is followed in real space, one is peering into the phase space of the Hamiltonian system defined by its flow kinematics. While this identification must have been known for quite some time, its consequences in terms of fluid stirring and mixing were realized only more recently [1].

If ψ is independent of time, Eqs. (2.1) constitute two first-order ODEs with a conserved quantity, namely ψ itself. Such a problem is

* Corresponding author at: Department of Engineering Science & Mechanics, Virginia Tech, Blacksburg, VA 24061, USA.
E-mail address: haref@vt.edu (H. Aref).

0167-2789/$ – see front matter © 2010 Elsevier B.V. All rights reserved.
doi:10.1016/j.physd.2010.08.007

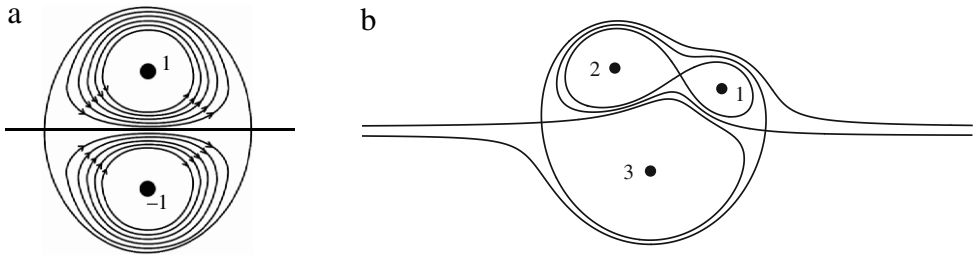

Fig. 1. Streamline patterns in a co-moving frame of translating vortex configurations. (a) Kelvin's atmosphere of a translating vortex pair of relative circulations ± 1, after Thomson [4]; (b) atmosphere of a translating vortex tripole with vortices labeled according to their relative circulations, after Aref et al. [5]. Both configurations translate from left to right.

clearly integrable. More formally, the rate of change of ψ following a particle is

$$\frac{\mathrm{D}\psi}{\mathrm{D}t} = \frac{\partial\psi}{\partial t} + u\frac{\partial\psi}{\partial x} + v\frac{\partial\psi}{\partial y} = \frac{\partial\psi}{\partial t}.$$

Hence, ψ is a Langrangian invariant precisely when it has no explicit time dependence, i.e., precisely when the flow is steady. For time-dependent ψ, we have a non-autonomous Hamiltonian system with one degree of freedom, sometimes said to have "one-and-a-half degrees of freedom". Such a system is closer in its properties to a two-degree-of-freedom system than to the autonomous, steady flow, one-degree-of-freedom system. As Arnold [2] put it, somewhat provocatively, in his textbook: "Analyzing a general potential system with two degrees of freedom is beyond the capability of modern science". In other words, advection by a 2D, unsteady, incompressible flow is a surprisingly difficult problem.

Chaos in the dynamical system (2.1) leads to nonlinear excursions where particles initially placed close to one another may deviate exponentially. In turn, this *chaotic advection* leads to efficient stirring of the fluid and, in due course, to enhanced mixing. See [3] for a historical perspective on the development of this idea. Applications of chaotic advection, sometimes called chaotic mixing, encompass length scales from thousands of kilometers (in geophysical applications) to microns (microfluidics).

Two classical examples related to particle advection are worth noting. The first is Kelvin's idea of the "atmosphere" of a vortex pair [4]. In the problem of two point vortices (see Section 3), a pair of opposite vortices will translate side by side, the 2D counterpart of a vortex ring. Kelvin noticed that if one goes to the rest frame of the pair, the steady streamline pattern has an oval envelope surrounding the vortices. Fluid within the envelope will advect forward with the pair, while fluid exterior to the envelope travels around the oval dividing streamline and is eventually left behind. The original diagram (with the horizontal streamline added) is reproduced in Fig. 1(a). A trapped region of fluid of this type is usually referred to as the *atmosphere* of the vortex pair.

The appearance of a region of fluid in a bound motion about a point vortex is generic due to the vortex being an isolated point about which there is circulation in an otherwise irrotational flow. Fig. 1(b) shows a more elaborate situation with three vortices having zero net circulation placed at the vertices of an equilateral triangle [5]. This configuration is a relative equilibrium that translates uniformly. The gross features of the streamline pattern in the rest frame of such a translating vortex tripole are similar to the streamline pattern around the translating dipole in Fig. 1(a). In particular, the velocity field far from the tripole is similar, to leading order, to the flow field far from the dipole. There is a forward and a rearward stagnation point, and there are regions of fluid that orbit each of the three vortices and are carried along with them. However, the specific pattern of the dividing streamlines for the vortex tripole is considerably richer than for the vortex dipole. The single streamline that impinges on the vortex pair atmosphere from the front and departs from the rear has been broadened into a band of fluid that enters the tripole at its front, loops around inside it, and exits from the back. There is also a region of fluid that orbits both of the two positive vortices.

There are simpler examples as well: for a cylinder of small radius with circulation around it, a common model of a spinning cylinder in a uniform stream of viscous fluid, there will be a trapped region around the cylinder when its angular velocity is high enough that the stagnation streamline detaches. This example is usually included in introductory texts as part of the discussion of lift on a spinning cylinder. The region inside the detached, self-intersecting streamline constitutes an atmosphere that follows the cylinder.

Since streamlines and pathlines coincide for steady flows, these examples illustrate that questions of particle trapping around vortex configurations or spinning bodies can be decided quite easily in cases where the fluid motion becomes steady in a suitably chosen rest frame.

In an appropriate frame of reference, a point where a (steady) streamline self-intersects is a stagnation point of the flow. For an incompressible flow, such a point will generally be a saddle point. The trapped region, if there is one, will then have one boundary that is a homoclinic or heteroclinic saddle connection of the streamline pattern. This leads to the trapped region being, in general, unstable to perturbations. Thus, if a steady flow with this kind of flow feature is made unsteady by a perturbation, the trapped fluid will tend to "leak out" due to the disintegration of the saddle point into a homoclinic or heteroclinic tangle. This is a general mechanism of chaos. Due to the leakage, the question of long-term existence of trapped regions in unsteady flow becomes quite difficult and requires advanced tools from the theory of dynamical systems. For background and details see any of several texts on chaotic dynamics, e.g., [8]. For a collection of articles that deal with the so-called "Lagrangian coherent structures", essentially contours of Lyapunov exponents, see [9].

All the stagnation points shown in Fig. 1, except for the vortices themselves, are hyperbolic. Leakage from a configuration such as that in Fig. 1(a) due to an externally applied perturbation was analyzed in detail by Rom-Kedar et al. [10]. Applying their results to a configuration such as Fig. 1(b), we see that the hyperbolic point located between the two positive vortices is not "dangerous"—even if it leaks due to perturbation, the trapped fluid will still remain inside a confined region. (One can imagine sufficiently localized perturbations that the inner saddle connection is destroyed, but the outer one remains intact.) The front and rearward hyperbolic points, however, will leak to the ambient fluid exactly as in the case of the vortex pair. Indeed, in this case leakage may lead to an enhancement of the transport through the dipole that is already present in the steady state. A systematic analysis of this case awaits execution.

The second example we highlight is the analysis by Maxwell [6]. The advection due to uniform translation of a cylinder through

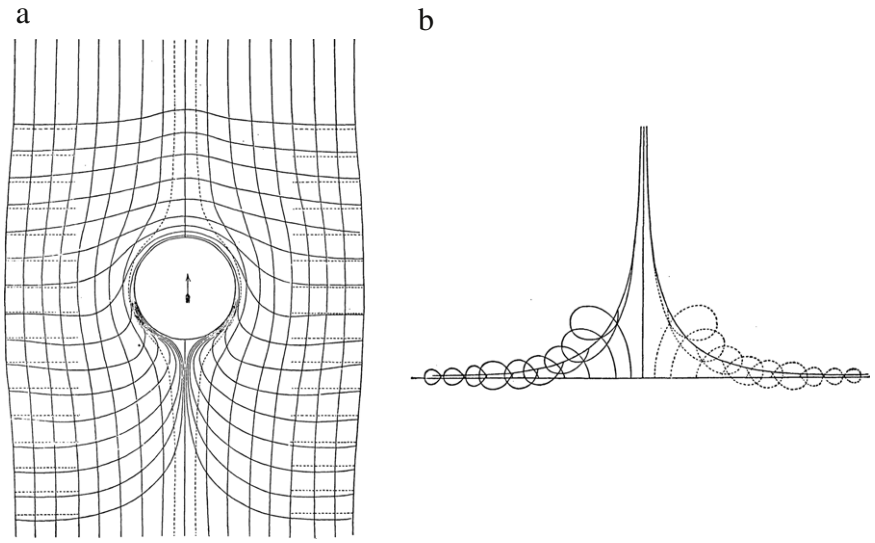

Fig. 2. Particle motion due to a translating cylinder in 2D ideal flow. (a) Deformation of a rectangular grid of material lines; (b) trajectories of individual fluid particles. After Maxwell [6].

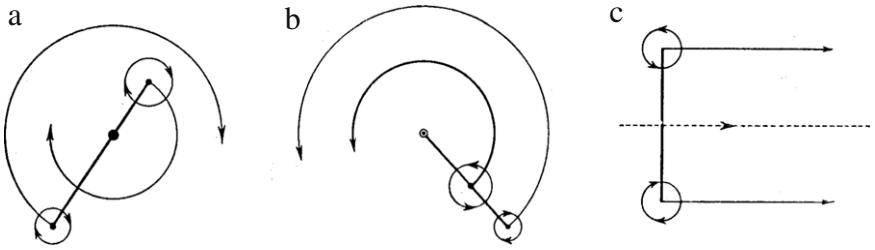

Fig. 3. Vortex trajectories for two-vortex motion in 2D ideal flow. (a) Vortices of the same sign; (b) vortices of opposite sign; (c) a pair of vortices of opposite strengths. After Joukowski [7].

2D ideal fluid otherwise at rest is considered. Maxwell showed that the advection is integrable in this case by directly integrating the resulting advection Eqs. (2.1) in the rest frame of the cylinder where the flow is steady. He produced plots of both the deformation of material lines and the trajectories of individual particles. These are reproduced in Fig. 2. The characteristic looping motion, where the particle is first pushed ahead and away from the cylinder, and subsequently is sucked in behind it as it moves past, will reappear in what follows. While particles that are initially close to one another will certainly deviate as the flow progresses, they will only do so algebraically, not exponentially as in the case of chaotic motion. Morton [11] extended Maxwell's analysis to elliptical cylinders and also considered the case of uniform rotation. We shall return to recent extensions of this work in Section 4.

With one notable exception, interest in Lagrangian aspects of fluid flows, including particle trajectories, seems to have waned for several decades in the first half of the 20th century. The paper by Darwin [12], which introduced the notion of *drift*, was published some 40 years after Morton's study (and does not cite his work). Darwin's work was famously taken up a few years later by Lighthill [13] in a paper that probably can claim to have the shortest title of any in fluid mechanics. The notable exception is the study of vortex motion, a subject where Lagrangian considerations play a very significant role. Tracking vortices analytically, numerically or experimentally has been of considerable interest for a long time. We turn to this topic next.

3. Point vortices

These intriguing singular structures and their equations of motion were introduced by Helmholtz [14] in his seminal paper. On the unbounded plane, thought of as the complex plane, we consider N point vortices of constant circulations $\Gamma_1, \ldots, \Gamma_N$. The positions of the vortices at time t may be thought of as complex numbers $z_1(t), \ldots, z_N(t)$. If we only have the vortices, and no boundaries or imposed potential flow, the mutually induced motion is given by the set of ODEs:

$$\overline{\frac{\mathrm{d}z_\alpha}{\mathrm{d}t}} = \frac{1}{2\pi \mathrm{i}} \sum_{\beta=1}^{N}{}' \frac{\Gamma_\beta}{z_\alpha - z_\beta}, \quad \alpha = 1, \ldots, N. \tag{3.1}$$

The bar over the vortex velocity on the left-hand side indicates complex conjugation. See [15] or any of several texts on fluid mechanics for a derivation and discussion. The earliest use of the complex variable representation is unclear, but it was certainly used by Friedrichs [16] in his lectures on the subject. The prime on the sum on the right-hand side tells us to omit the singular term $\beta = \alpha$.

The solution to the two-vortex problem was given by Helmholtz. The solution of the three-vortex problem for arbitrary circulations is due to Gröbli [17], see [15,18] for further background. The trajectories for two-vortex motion are shown in Fig. 3. Two vortices generally orbit on concentric circles. They move opposite to one another when their circulations are of the same sign, Fig. 3(a), and together when they are of opposite sign, Fig. 3(b). In the special

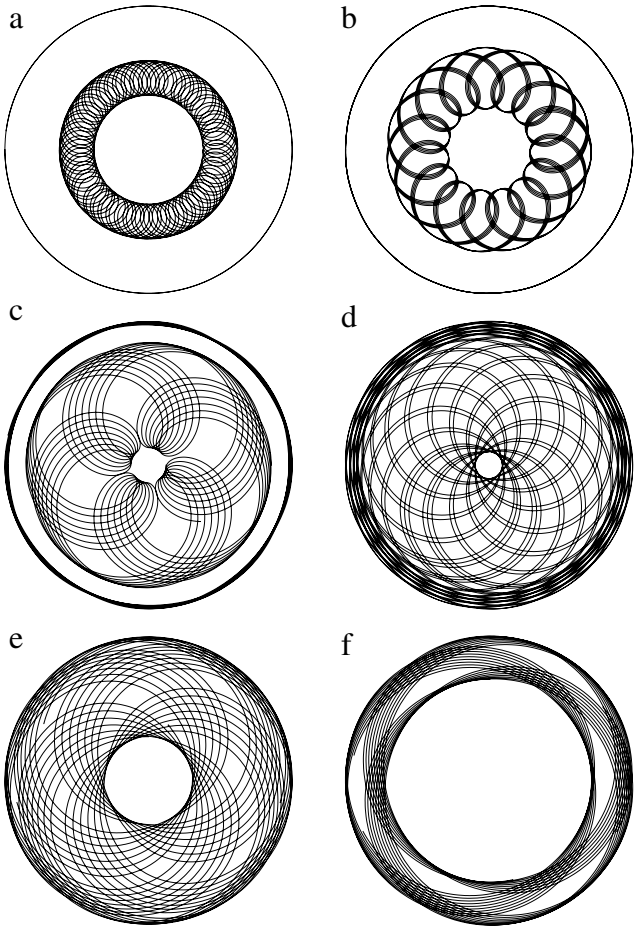

Fig. 4. Vortex trajectories for motion of three identical vortices in 2D ideal flow. In (a) the distance between two of the vortices is much smaller than the distances of these two from the third vortex. As we progress through (b)–(f), the initial positions are changed such that the distances between the three vortices become more and more alike.

case when their circulations are exactly opposite, they translate along parallel lines with uniform velocity. The atmosphere for a translating vortex pair, Fig. 1(a), is the streamline pattern in the co-moving frame of the motion depicted in Fig. 3(c).

The trajectories for the three-vortex problem vary with the vortex circulations and, for given circulations, with the initial positions of the vortices. Fig. 4 shows a series of trajectories for three identical vortices as the initial positions are varied. In the initial panel, Fig. 4 (a), two of the vortices are much closer together than either one is to the third vortex. In effect, these two form a bound state that acts much like a single vortex of twice the strength. This "compound vortex" then orbits the third vortex, as we see in Fig. 3(a), although its internal structure leads to a small periodic perturbation of the overall motion. As we make the three inter-vortex distances more and more similar in size, we produce more and more "collective motion" in which there are no bound states between any two of the vortices. Ultimately, as we approach an initial condition in the shape of an equilateral triangle, where the three vortex separations are equal, we obtain a relative equilibrium which, for three identical vortices, is stable. The regularity of the trajectory plots in Fig. 4 arises from the motion being quasi-periodic as one would expect in an integrable system.

Fig. 5 shows something quite different. We are again looking at vortex trajectories, this time during the collision and interaction of two vortex pairs, i.e., a four-vortex problem. The vortices have circulations ± 1 in each pair. This problem was explored by Price [19] and more recently by Tophøj and Aref [20]. For the motion shown the vortices colored blue and red are positive, the other two negative. The two pairs have been set on a collision course, with the two panels in Fig. 5 tracing the evolution from imperceptibly different initial conditions. A complicated collision interaction process takes place with numerous nonlinear excursions of the vortices until, after some time, two pairs re-emerge. The initial four loops are similar in the two panels, but then the motions depart quite radically from one another since the motion is chaotic. Indeed, in Fig. 5(a) the two original pairs re-emerge in a process we call *direct scattering*. In Fig. 5(b), on the other hand, the vortices switch partners in a process we call *exchange scattering*.

Four-vortex problems are generally non-integrable, although for special choices of the circulations and the initial conditions we may have integrability. The most interesting example is for the case $\Gamma_1 + \Gamma_2 + \Gamma_3 + \Gamma_4 = 0$ and

$$\Gamma_1 z_1 + \Gamma_2 z_2 + \Gamma_3 z_3 + \Gamma_4 z_4 = 0. \tag{3.2}$$

For choices of the four circulations and initial positions that satisfy these two constraints the problem of relative motion of the vortices can be "projected down" to a three-particle problem, akin to the three-vortex problem, and a complete analysis performed [21,22]. When the motion is bounded, the relative motion is periodic, and trajectories of the four vortices are reminiscent of the trajectories seen in Fig. 4. For unbounded motions, we obtain regular counterparts to the scattering trajectories in Fig. 5. Aref and Stremler [22] give many examples of trajectory plots.

In the limit when one of the four vortices has circulation zero and so has become a passive particle in the flow field generated by the three remaining vortices, we have an interesting split between the four fluid particles under consideration: the three vortices move integrably as in Fig. 4, while the passively advected particle moves chaotically according to the considerations in Section 2. This *restricted four-vortex problem* [23] was the pre-cursor to the general idea of chaotic advection. As an amusing historical aside we may mention that in his thesis [17], which was the first publication in which the three-vortex problem was solved, Gröbli wrote: "Auf die Bestimmung der Bewegung von Flüssigkeitstheilchen welche sich in endlicher Entfernung von den Wirbelfäden befinden, werden wir nicht eingehen". [English translation: "We shall not enter into the determination of the motion of fluid particles located at a finite distance from the vortices".] This suggests that he had tried the problem of advection by three vortices and found it impenetrable to analysis. Today we understand the reason: one cannot make much analytic progress with a chaotic system.

Fig. 6 provides an example of restricted four-vortex motion in which the three vortices move regularly and the passive particle moves irregularly. Not only is the trajectory of the advected particle clearly less regular than the vortex motion, the details of the trajectory are also sensitive to small perturbations of the initial particle position. Between panels (a) and (b) in Fig. 6, the initial position of the advected particle has been shifted by 0.0025 times the initial separation between vortices 1 and 2.

When might advection by three vortices be integrable? If we think of the problem as the limiting case of the four-vortex problem with $\Gamma_4 = 0$, then the case of advection by three vortices with $\Gamma_1 + \Gamma_2 + \Gamma_3 = 0$ and $\Gamma_1 z_1 + \Gamma_2 z_2 + \Gamma_3 z_3 = 0$ should be integrable. Indeed it is but, unfortunately, in a trivial way: for vanishing linear impulse the solution to the problem of three vortices with net circulation zero is a rigidly rotating, collinear tripole [24,25]. For the symmetric case, $\Gamma_1 = \Gamma_2$, it is related to the well-known tripole vortex of geophysical fluid dynamics [26]. The advection about such a structure is clearly integrable as one sees by transforming to the co-rotating frame of the tripole.

There are other instances of integrable advection by three vortices (e.g., advection by a translating tripole as in Fig. 1(b)) but, in general, the advection is irregular, and the restricted four-vortex problem is chaotic.

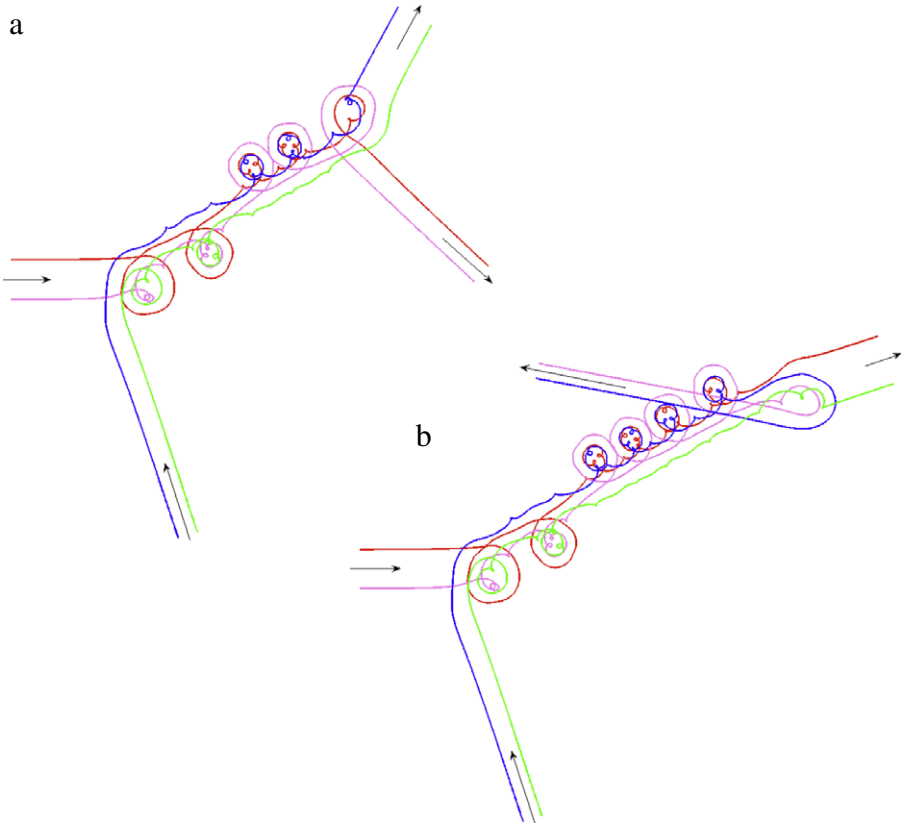

Fig. 5. Vortex trajectories for the collision-interaction of two vortex pairs. Each vortex is color-coded, with blue and red vortices having strength $+1$, green and purple vortices having strength -1. Initial conditions vary imperceptibly between (a) and (b), yet the long-term outcome is very different since the interaction takes place in a chaotic regime.

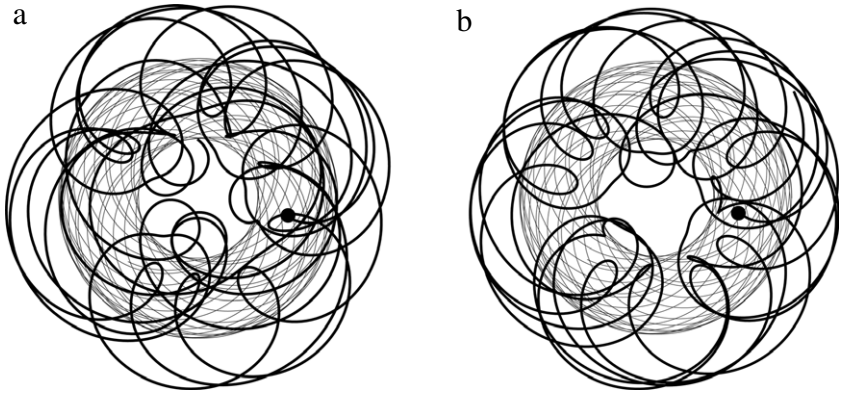

Fig. 6. Advected particle trajectory (black) in the field of three identical vortices in 2D ideal flow (trajectories shown as grey). The vortex motion is of the integrable variety seen in Fig. 4. The trajectory of the advected particle is clearly much less regular than the vortex trajectories. Furthermore, small perturbations of the starting position of the particle (shown by black dots in the two panels) lead to substantial deviations in the trajectory.

4. Rigid bodies

We may also consider particle motion problems that include, in addition to point vortices, a rigid body that is free to move and, inevitably, advected particles. The motion of the body, which is launched with a linear and angular velocity, is affected by the reactive pressure forces from the fluid, which may include contributions from one or more point vortices. Apart from the motion of the body, and the choice of initial positions of the vortices, the fluid is assumed "otherwise at rest". We now enter the topic of *flow-structure interactions* viewed from a Lagrangian perspective.

Incorporating a rigid body into the equations of motion requires several adaptations: first, the moving rigid body produces a potential flow that must be added to the right-hand sides of Eq. (3.1). The calculation of the potential flow induced by the body motion is, in essence, classical and one can find an algorithm for it in the text by Milne-Thomson [27]. Since the fluid domain outside a finite rigid body is no longer simply connected, ideal flow theory also provides the freedom to assign a constant circulation around the body. Such a circulation, in turn, adds a term to the potential flow. Next, the mere presence of the rigid body changes the boundary conditions on the vortex flow and thus the motion of the vortices: the vortices have "images" inside the rigid body. This part of the modification to Eq. (3.1) is essentially the *Kirchhoff–Routh–Lin theory* of point vortex motion outside a rigid boundary [28]. The third and final ingredient required is the equations of motion of the body itself. These are, in essence,

the *Kirchhoff–Kelvin equations* for rigid body motion, now with the addition of the forces due to the vortices and the circulation around the body. A convenient way of stating these equations in the present case turns out to be conservation of linear and angular impulse for the entire system, since no external forces act. These equations are available at several places in the literature [29–33]. The formal statement of the equations of motion is cumbersome and so we omit it here.

Although the analysis covers general body shapes and arbitrary mass distributions within the body, most studies have been done for ellipses with the further specialization that the ellipse has a homogeneous mass distribution within it, so the geometrical center of the ellipse coincides with its center of mass. Ellipses are given by the Riemann mapping

$$f(\zeta) = \zeta + \frac{a^2}{\zeta}, \tag{4.1}$$

from a unit circle in a second, complex ζ-plane to the physical plane. For $0 \leq a \leq 1$, the mapping (4.1) sends $\zeta = e^{i\vartheta}$, $0 \leq \vartheta < 2\pi$, to an ellipse in the physical plane with foci at $\pm 2a$ and eccentricity $\frac{2a}{1+a^2}$. The case of a circular cylinder corresponds to $a = 0$. For $a = 1$, we obtain a flat plate connecting the points ± 2. In the illustrations provided here, Figs. 7 and 8, we have used a rather elongated ellipse corresponding to the parameter choice $a = 0.7$.

Fig. 7 provides an example from the very simplest problem in this category: the result of particle advection in the flow field due to a freely moving elliptical cylinder. In this calculation, the mass of the ellipse is equal to the mass of the fluid it displaces—had gravity been included, the elliptical cylinder would be neutrally buoyant. The cylinder has no circulation about it and in this case no vortices have been introduced into the flow field. The entire fluid motion is due to the moving body. The body motion is integrable as first shown by Kirchhoff, cf. [35]. However, the motion of the particles around it is apparently chaotic as illustrated in Fig. 7. Two particles were started virtually at the same location: the deviation in initial positions is 10^{-5} times the dimension of the ellipse. Hence, the two particles initially follow virtually the same path. At some point, however, the exponential deviation in their long-time trajectories becomes apparent, and the two particles move to opposite sides of the ellipse! This is another example of the chaotic advection phenomenon from Section 2.

Returning to another theme of Section 2 we may ask: Is it possible for a rigid body, translating and rotating in an ideal fluid, to carry an atmosphere with it in its motion? Clearly, the uniformly translating circular cylinder analyzed by Maxwell [6] does not carry fluid with it. Had we introduced a circulation around the cylinder, on the other hand, it could have an atmosphere, as mentioned in Section 2. But what if we consider an ellipse, with no circulation about it, that is spinning and translating integrably as per Kirchhoff's solution? In the limit of pure rotation Morton [11] showed that there would be "islands" on either side of the ellipse. As Lamb [35] wrote, when reviewing this work: "The *paths* followed by the particles of fluid in several…cases, as distinguished from the streamlines, have been studied by Prof. Morton; they are very remarkable". The result lay dormant for four decades until Darwin rediscovered it [12], apparently without being aware of the work by Morton [11]. We may add a modern twist to this result: if the islands are slightly perturbed by adding a small translation to the body motion, *KAM theory* shows that some kind of islands remain. Roenby and Aref [34] show that for a predominantly spinning motion of the ellipse, it may indeed carry an atmosphere with it. The atmosphere breaks up into regular "islands" embedded in a chaotic "sea". Numerical experiments [34] show that so long as the ratio of translational velocity to angular velocity multiplied by a characteristic, linear dimension of the body is 0.1 or less, a discernible atmosphere is present. In Fig. 7 we have exploited our knowledge of where the chaos is within such an atmosphere to pick initial positions that are very close in the chaotic part of the atmosphere. The two particle trajectories follow one another for a long time (since the initial conditions are so close) but ultimately deviate considerably due to exponential separation of close orbits in a chaotic system.

We have also studied the case of an ellipse and one vortex, when the circulation around the body is opposite to the circulation of the vortex [33]. This corresponds physically to the case when the vortex has been shed from the body by viscous flow processes that are, of course, not captured in the model. This is certainly an important special case from the point of view of applications.

Fig. 8 shows two examples of trajectories of the center of an ellipse and of a point vortex with which it interacts. In these examples the mass of the ellipse equals one quarter the mass of displaced fluid. Both examples have the same values of linear and angular impulse and of the Hamiltonian (kinetic energy) of the motion. The differences in the trajectories come from a small change in the initial position of the vortex that was constructed so that it preserves the constants of motion. Visual observation suggests that the top trajectories in Fig. 8 show a predominantly regular motion of both body and vortex, while the bottom trajectories show chaotic motion of both. These conclusions are borne out by considering other measures, in particular appropriately constructed Poincaré sections of the motion [33]. One curious observation is that when regular and irregular motions exist side by side for the same values of the integrals (and for all system parameters), the irregular motion makes greater headway in a fixed interval of time than the regular motion. This is clear from Fig. 8 where both interaction sequences have been traced for the same time interval.

There is a gross similarity between the body–vortex motions in Fig. 8 and the forward motion of a vortex pair, Fig. 3(c). The vortex and the body, which has a circulation around it that is opposite to the circulation of the vortex, move forward together. However, the strong body–vortex interactions arising from having the body and the vortex close to one another induce the many nonlinear excursions that are evident. For some initial conditions the paths of both vortex and body center are predominantly regular, for others they are irregular. This is similar to the Lagrangian chaos seen in the vortex interaction problems discussed in Section 3.

5. Concluding remarks

In conclusion we make three points. First, consider 2D inviscid hydrodynamics written in the Lagrangian representation as a pair of PDEs for the position coordinates of a fluid particle (PDEs because the Lagrangian positions depend on the initial coordinates and on time). Our examples suggest that this is unlikely to be a useful approach in general. We have seen that already within the "universe" of a rigid body, a few point vortices and a passively advected particle, individual material points in the same flow can have either integrable (regular) or chaotic (irregular) motions. For example, three (and in special cases four) interacting vortices will (can) have regular trajectories while a particle they advect will move irregularly (more or less so depending on where it is started in the flow). Similarly, a rigid body may move regularly in response to fluid reactive forces, but the flow field it induces by its motion advects particles chaotically. Encompassing both these types of motion in a single solution of the aforementioned PDEs is not possible. In terms of describing the flow field, then, the conventional Eulerian representation is the preferred approach since the additional level of detail given by individual particle trajectories is "hidden". Abrashkin and Yakubovich [36,37] attempted to study 2D ideal flow with embedded vorticity using the Lagrangian representation. However, they had to confine

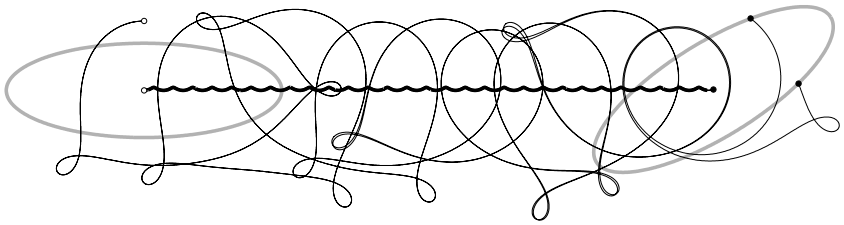

Fig. 7. Trajectories of two particles (large amplitude black curves) advected by the motion of a homogeneous elliptical cylinder in an ideal fluid. The center of the ellipse moves left-to-right along the small-amplitude, wiggly curve. Initial and final positions of the cylinder are shown by grey outlines. Initial positions (open circles) of the two particles are virtually identical. Initially the particles follow the same path. After some time, however, one particle moves to the other side of the ellipse. Final positions of particles are shown as black dots. The motion of the cylinder is integrable, the motion of the particles chaotic. For additional details see [34].

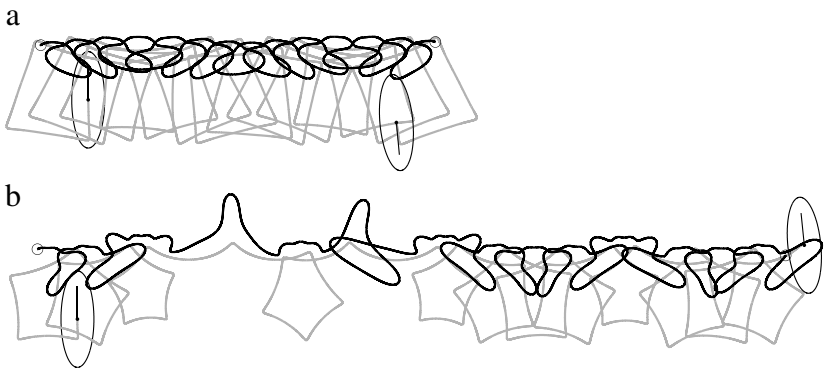

Fig. 8. Trajectories of a point vortex (black curve) and the center of a homogeneous elliptical cylinder (grey curve), with a circulation around it that is opposite to the vortex, as they interact in an ideal fluid. The cylinder has one quarter of the mass of the fluid it displaces. The initial and final positions of the ellipse are shown. The initial and final positions of the point vortex are shown as open circles. Both trajectory segments are for the same length of time. Top: the body–vortex interaction is predominantly regular. Bottom: chaotic body–vortex interaction. The initial positions of the vortices in the two sequences are only sightly different. For additional details see [33].

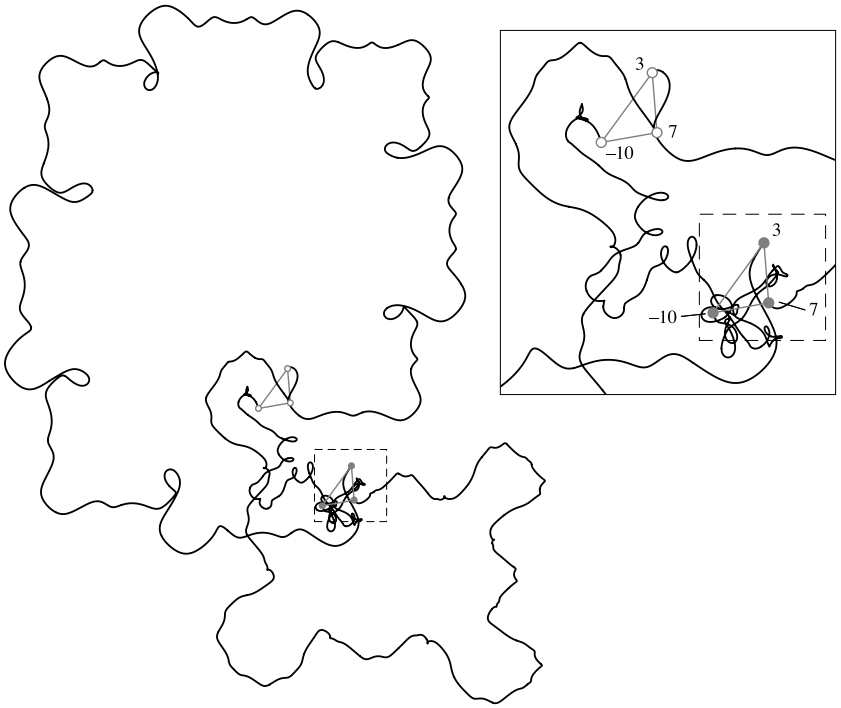

Fig. 9. Trajectories of three vortices (black curves) in a square, doubly-periodic domain during one period of the relative motion. This problem is integrable and periodic, yet the trajectories are quite complex. The inset shows a close-up of the basic square (dashed lines). Vortices are labeled according to their relative circulations, 7, 3 and −10. Initial (solid circles) and final (open circles) vortex positions are joined (grey curves) to highlight the periodicity of the relative motion. The vortices travel well beyond the boundaries of the basic square and interact with numerous periodic images, which are not shown.
Source: From [38].

themselves to solutions with simple time dependence of the vorticity field. A more complicated vorticity field would immediately bring in chaotic motions. We suggest that our simple examples, even though they involve singular point vortices, illustrate why a purely Lagrangian representation runs into difficulties.

Second, we point out that one cannot, in all cases, decide whether particle motions are regular or chaotic simply by looking at them. We have been somewhat cavalier with the assignment of labels such as "integrable" and "chaotic", or "regular" and "irregular", in the preceding developments. However, there are more rigorous definitions and arguments behind these assignments, and further numerical diagnostics in the chaotic/irregular case, that support the assignments we have made. Nevertheless, the issue arises if one can simply "see" integrability versus chaos "with the naked eye" from the regularity or irregularity of particle trajectories. From the examples given up to now it would appear that one can.

We provide a cautionary note with Fig. 9 taken from calculations of integrable motion of three vortices in a square domain with periodic boundary conditions [38]. Although the interactions are more complex than in Eq. (3.1)—the periodic images result in the inter-vortex interactions involving Weierstrass elliptic functions—the symplectic structure is similar, and the three-vortex problem is integrable when the sum of the vortex circulations vanishes. See [38] for details. Similar, although less dramatic, examples are seen in the integrable case of three vortices, with net circulation zero, in a periodic strip [39]. The example shown is from the case of circulations 7, 3, and −10 (only the ratio of circulations matters).

For rational ratios between the vortex strengths, the relative motion is periodic except for separatrices. Thus, in principle, the motion is quite simple. What comes as a surprise is that the motion during a period can be very complex. Visual observation of the three trajectories in Fig. 9, without knowing that the relative motion is periodic, would not immediately suggest integrability! Indeed, if the ratios between the vortex circulations are irrational, the problem is still Liouville integrable but the relative motions are not periodic. In terms of complexity and convolution these trajectories compare well to computed trajectories of strong isolated vortices in numerical simulations of 2D Navier–Stokes turbulence, even though a vortex in the turbulence simulation may encounter additional processes such as merging or tearing. One point of Fig. 9, then, is to underscore that visual observation of trajectories alone may be ambiguous in assessing integrability versus chaos. Closer analysis of the particle trajectories is required, and any assessment should be corroborated by looking at further diagnostics.

Finally, we remark that chaos in the Lagrangian representation of a flow may seem a rather subtle thing. As we said previously, it is largely invisible if one works in the Eulerian representation. However, the chaotic motion of individual particles or bodies provides a key mechanism in a number of situations. Apart from the well studied applications to stirring and mixing of viscous fluids, we submit that chaotic vortex motion and chaotic interactions between vortices and bodies have potential applications to areas such as turbulence, flow-structure interactions, and advective transport. In the Eulerian framework it would be difficult to distinguish three vortices moving regularly while advecting particles chaotically. Similarly, it would be difficult to distinguish chaotic and regular body-vortex interactions. These issues are intrinsically Lagrangian both in their formulation and elucidation. The fluctuations in particle positions, or in forces on a body, are quite different in the regular and chaotic regimes. In order to understand such differences, and their consequences, one has to adopt a Lagrangian description.

Acknowledgements

We thank members of the *Center for Fluid Dynamics* at *DTU* for comments and discussion. This work is supported by a Niels Bohr Visiting Professorship at the Technical University of Denmark sponsored by the Danish National Research Foundation.

References

[1] H. Aref, Stirring by chaotic advection, J. Fluid Mech. 143 (1984) 1–21.
[2] V.I. Arnold, Mathematical Methods of Classical Mechanics, Springer, ISBN: 0-3879-6890-3, 1978.
[3] H. Aref, The development of chaotic advection, Phys. Fluids 14 (2002) 1315–1325.
[4] Sir W. Thomson (Lord Kelvin), On vortex atoms, Proc. Roy. Soc. Edinburgh 6 (1867) 94–105.
[5] H. Aref, M.A. Stremler, F.L. Ponta, Exotic vortex wakes—point vortex solutions, J. Fluids Struct. 22 (2006) 929–940.
[6] J.C. Maxwell, On the displacement in a case of fluid motion, Proc. Lond. Math. Soc. 1–3 (1870) 82–87.
[7] N.E. Joukovskii, Helmholtz's works on mechanics, in: A.G. Stoletov (Ed.), Hermann von Helmholtz 1821–1891. Public Lectures Delivered at the Imperior Moscow University for the Helmholtz Fund, Moscow University Press, 1892, pp. 37–52 (in Russian).
[8] M. Tabor, Chaos and Integrability in Nonlinear Dynamics: An Introduction, Wiley, New York, 1989.
[9] T. Peacock, J. Dabiri, Focus issue: Lagrangian coherent structures, Chaos 20 (2010) 017501–017516.
[10] V. Rom-Kedar, A. Leonard, S. Wiggins, An analytical study of transport, mixing and chaos in an unsteady vortical flow, J. Fluid Mech. 214 (1990) 347–394.
[11] W.B. Morton, On the displacements of the particles and their paths in some cases of two-dimensional motion of a frictionless liquid, Proc. R. Soc. Lond. Ser. A 89 (1913) 106–124.
[12] Sir C. Darwin, Note on hydrodynamics, Math. Proc. Cambridge Philos. Soc. 49 (1953) 342–354.
[13] M.J. Lighthill, Drift, J. Fluid Mech. 1 (1956) 31–53.
[14] H.von Helmholtz, Über integrale der hydrodynamischen Gleichungen, welche den Wirbelbewegungen entsprechen, J. Reine Angew. Math. 55 (1858) 25–55. English translation by Tait, P.G. On integrals of the hydrodynamical equations, which express vortex-motion, Phil. Mag. 33 (4) (1867), 485–512.
[15] H. Aref, Integrable, chaotic and turbulent vortex motion in two-dimensional flows, Annu. Rev. Fluid Mech. 15 (1983) 345–389.
[16] K.O. Friedrichs, Special Topics in Fluid Dynamics, in: Notes on Mathematics and its Applications, Gordon & Breach, New York, ISBN: 0677010052, 1966.
[17] W. Gröbli, Spezielle probleme über die Bewegung geradliniger paralleler Wirbelfäden, (Zürcher ung Furrer, Zürich, 1877); also Vierteljahrsschr. Naturforsch. Ges. Züer. 22, 37–81, 129–165.
[18] H. Aref, Chaos in the dynamics of a few vortices—fundamentals and applications, in: N. Olhoff, F.I. Niordson (Eds.), Proceedings of the Sixteenth International Congress of Theoretical and Applied Mechanics, Lyngby, Denmark, 1984, North-Holland Publ. Co., 1985, pp. 43–68.
[19] T. Price, Chaotic scattering of two identical point vortex pairs, Phys. Fluids A 5 (1993) 2479–2483.
[20] L. Tophøj, H. Aref, Chaotic scattering of two identical point vortex pairs revisited, Phys. Fluids 20 (2008) 093605.
[21] B. Eckhardt, Integrable four vortex motion, Phys. Fluids 31 (1988) 2796–2801.
[22] H. Aref, M.A. Stremler, Four-vortex motion with zero total circulation and impulse, Phys. Fluids 11 (1999) 3704–3715.
[23] H. Aref, N. Pomphrey, Integrable and chaotic motions of four vortices, Phys. Lett. A 78 (1980) 297–300.
[24] N. Rott, Three-vortex motion with zero total circulation, J. Appl. Math. Phys. ZAMP 40 (1989) 473–494. [With an Addendum by H. Aref (1989)].
[25] H. Aref, Three-vortex motion with zero total circulation: addendum, J. Appl. Math. Phys. ZAMP 40 (1989) 495–500.
[26] G.J.F. van Heijst, R.C. Kloosterziel, Tripolar vortices in a rotating fluid, Nature 338 (1989) 569–571.
[27] L.M. Milne-Thomson, Theoretical Hydrodynamics, 5th ed., MacMillan & Co., Ltd., London, 1968, (Republished by Dover Publications, New York).
[28] C.C. Lin, On the Motion of Vortices in Two Dimensions, University of Toronto Press, Toronto, 1943.
[29] B.N. Shashikanth, J.E. Marsden, J.W. Burdick, S.D. Kelly, The Hamiltonian structure of a 2D rigid circular cylinder interacting dynamically with *N* point vortices, Phys. Fluids 14 (2002) 1214–1227;
B.N. Shashikanth, J.E. Marsden, J.W. Burdick, S.D. Kelly, The Hamiltonian structure of a 2D rigid circular cylinder interacting dynamically with *N* point vortices, Phys. Fluids 14 (2002) 4099 (erratum).
[30] A.V. Borisov, I.S. Mamaev, S.M. Ramodanov, Dynamic interaction of point vortices and a two-dimensional cylinder, J. Math. Phys. 48 (2007) 065403.
[31] E. Kanso, B. Oskouei, Stability of a coupled body-vortex system, J. Fluid Mech. 800 (2008) 77–94.
[32] S. Michelin, S.G. Llewellyn Smith, An unsteady point vortex method for coupled fluid–solid problems, Theor. Comput. Fluid Dyn. 23 (2009) 127–153.
[33] J. Roenby, H. Aref, Chaos in body-vortex interactions, Proc. R. Soc. Lond. Ser. A 466 (2010) 1871–1891.

[34] J. Roenby, H. Aref, On the atmosphere of a moving body, Phys. Fluids 22 (2010) 057103.
[35] H. Lamb, Hydrodynamics, 6th ed., Cambridge University Press, Cambridge, 1932.
[36] A.A. Abrashkin, E.I. Yakubovich, Planar rotational flows of an ideal fluid, Sov. Phys. Dokl. 29 (1984) 370–371.
[37] A.A. Abrashkin, E.I. Yakubovich, Steady flows with constant vorticity, Sov. Phys. Dokl. 32 (1987) 6–8.
[38] M.A. Stremler, H. Aref, Motion of three vortices in a periodic parallelogram, J. Fluid Mech. 392 (1999) 101–128.
[39] H. Aref, M.A. Stremler, On the motion of three point vortices in a periodic strip, J. Fluid Mech. 314 (1996) 1–25.

Instability of vortex pair leapfrogging

Laust Tophøj[1, 2, a)] and Hassan Aref[2, 3]
[1)] *Department of Physics, Technical University of Denmark, Kongens Lyngby, DK-2800, Denmark*
[2)] *Center for Fluid Dynamics, Technical University of Denmark, Kongens Lyngby, DK-2800, Denmark*
[3)] *Department of Engineering Science & Mechanics, Virginia Tech, Blacksburg, VA 24061, USA*

(Dated: 1 March 2012)

Leapfrogging is a periodic solution of the four-vortex problem with two positive and two negative point vortices all of the same absolute circulation arranged as co-axial vortex pairs. It occurs for initial pair size ratio $\alpha > \sigma^2$, where $\sigma = \sqrt{2}-1$ is the silver ratio. The motion is known in full analytical detail since the 1877 thesis of Gröbli and a well known 1894 paper by Love. Acheson [*Eur. J. Phys.* **21**, 269-273 (2000)] determined by numerical experiments that leapfrogging is linearly unstable for $\sigma^2 < \alpha < 0.382$, but apparently stable for larger α. Here we perform a Floquet analysis of the analytical solution. We find transition from linearly unstable to stable leapfrogging at $\alpha = \phi^2 \approx 0.381966$, where $\phi = \frac{1}{2}(\sqrt{5}-1)$ is the golden ratio. Acheson suggested also that there was a sharp transition between a "disintegration" instability mode, where two pairs fly off to infinity, and a "walkabout" mode, where the vortices depart from leapfrogging but still remain within a finite distance of one another. We show numerically that this transition is more gradual, a result that we relate to earlier investigations of chaotic scattering of vortex pairs [*Phys. Fluids* **20**, 093605 (2008)]. Both leapfrogging and "walkabout" motions can appear as intermediate states in chaotic scattering at the same values of linear impulse and energy.

Keywords: **ideal fluid dynamics, point vortices, leapfrogging, instability**

I. INTRODUCTION

The possibility that two vortex rings with a common axis can "leapfrog" was already mentioned by Helmholtz in his original paper on vortex dynamics[1]. He wrote (in Tait's translation): "We can now see generally how two ring-formed vortex-filaments having the same axis would mutually affect each other... the foremost widens and travels more slowly, the pursuer shrinks and travels faster, till finally, if their velocities are not too different, it overtakes the first and penetrates it. Then the same game goes on in the opposite order, so that the rings pass through each other alternately." Pipe smokers skilled in blowing smoke rings will often blow two rings in succession demonstrating the phenomenon. A more precise and often-cited flow visualization experiment was performed many years ago[2].

Here we are interested in the two-dimensional counterpart, where two co-axial vortex pairs leapfrog one another, in the special case when the four vortices all have the same absolute circulation. The analytical solution of this periodic motion, when the vortices are represented as point vortices, was derived by Gröbli[3], and subsequently by Love[4], more than a century ago. Gröbli and Love both found that leapfrogging was possible only if the size ratio of the two pairs at the moment one slips through the other is not too large. To quote from Love's paper[4]: "...the motion is periodic, if, at the instant when one pair passes through the other, the ratio of the breadths of the pairs is less than $3+2\sqrt{2}$. When the ratio has this precise value the smaller pair shoots ahead of the larger and widens, while the larger contracts, so that each is ultimately of the same breadth ..., and the distance between them is ultimately infinite. When the ratio in question is greater than $3+2\sqrt{2}$, the smaller shoots ahead and widens, and the latter falls behind and contracts... When the ratio is less than $3+2\sqrt{2}$, the motion of the two pairs is similar to the motion described by Helmholtz for two rings on the same axis, and it is probable that there is for this case also a critical condition in which the rings, after one has passed through the other, ultimately separate to an infinite distance, and attain equal diameters." We note that $3+2\sqrt{2} \approx 5.82843$ and that $(3+2\sqrt{2})^{-1} = 3-2\sqrt{2} \approx 0.171573$. Here $3-2\sqrt{2} = \sigma^2$, where $\sigma = \sqrt{2}-1$ is called the *silver ratio*.

In 2000 Acheson published a short paper[5] in which he reported on numerical simulations where the classical leapfrogging solution had been slightly perturbed, in essence by rotating one of the pairs so that it no longer was symmetric with respect to the centerline of the other. Acheson then found that the leapfrogging motion is unstable and that it breaks down through one of two different modes of instability. He worked in terms of the size ratio α of the smaller pair to the larger at the moment of slip-through. The classical solutions[3,4] show that leapfrogging requires $\alpha > \sigma^2 \approx 0.172$. For $\alpha = 0.220$ Acheson reproduced the classical solution numerically. Perturbing one of the vortex positions by one part in 10^6, Acheson observed the leapfrogging to cease after a few periods and the four-vortex system disintegrated into

[a)] Electronic mail: laust@fysik.dtu.dk

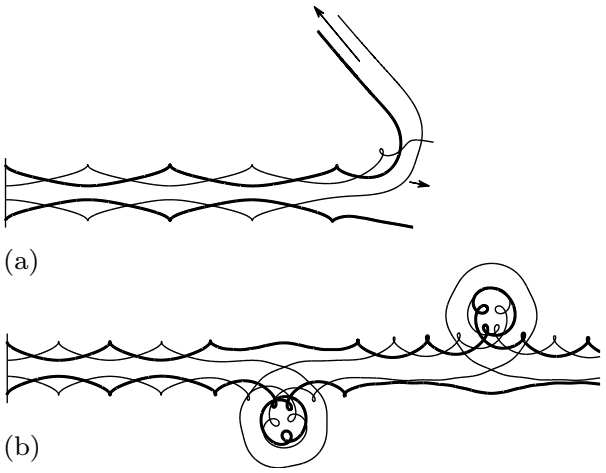

FIG. 1. Instability calculations of leapfrogging similar to those reported by Acheson[5]. Two different perturbations are shown. Vertical lines indicate the initial positions. (a) shows a "disintegration" instability for $\alpha = 0.25$ perturbed by $\xi_- = \eta_+ = -10^{-6}$. (b) shows a "walkabout" instability for $\alpha = 0.30$ perturbed by $\xi_- = 0, \eta_+ = 10^{-5}$ (see text for precise definitions).

two pairs that propagated off to infinity. (See Fig.1(a) for a similar calculation at $\alpha = 0.25$.) For $\alpha = 0.310$, and a larger perturbation, a different mode of instability was observed, that Acheson termed the "walkabout" instability. Here one vortex leaves its partner, crosses the centerline, and joins with the other pair in a complicated bounded motion while the entire system continues to move forward. This would then resolve itself back into a leapfrogging motion. Later another "walkabout" event might take place, and so on. (See Fig.1(b) for a similar calculation at $\alpha = 0.305$.) Acheson described his observations in these words: "What appears to happen is that two like-signed vortices occasionally get so close that they revolve rapidly around one another, and the combination of the two is then strong enough to sweep one of the other, oppositely-signed, vortices out of its usual path. The three then go off together on a roughly circular excursion, before meeting up again with the fourth, which has been continuing on a more or less straight path in the meantime. 'Walkabout' episodes of this kind take place on seemingly unpredictable sides of the original symmetry axis and at seemingly irregular intervals." In fact, these irregular "walkabout" motions and the sensitive dependence of the directions in which the two pairs propagate in the pair-disintegration mode are both manifestations of this four-vortex problem being chaotic. Acheson[5] found numerically that there was a transition from the disintegration instability mode to the "walkabout" mode when $\alpha \approx 0.29$. He also found that the "walkabout" instability had a finite range in α and ceased for $\alpha > 0.382$. In physical terms[5] this is "because vortices of like sign are close enough to 'stick together' and avoid disruption by a vortex of opposite sign."

In 2008 the present authors explored scattering experiments in which two identical vortex pairs were sent towards one another and the resulting motion was traced[6]. We found, among other things, that the intermediate bound states of all four vortices, before they eventually disintegrated into two independent pairs, could contain segments of leapfrogging and also segments that look like Acheson's "walkabout" instability. See Fig.7 in Ref.6 and also Fig.6 later in the present paper. Unfortunately, we were unaware of Acheson's paper[5] at the time.

Acheson's results[5] and ours[6] strongly suggest that the classical leapfrogging solution is an unstable periodic motion of the four-vortex system over part of its parameter range. This statement is amenable to more detailed analysis. Since we are considering a periodic solution, we are led to *Floquet theory*[7,8]. The paper is thus laid out as follows: In Sec.II we state the governing equations of motion and establish our notation. The four-vortex system is Hamiltonian. We introduce a new set of canonical variables for it, initially due to Eckhardt & Aref.[9] These variables reduce the four-degree-of-freedom problem to a two-degree-of-freedom problem and an auxiliary problem that can subsequently be solved. This canonical reduction is particularly important because it allows us to construct perturbations that conserve the total linear impulse of the system.

In Sec.III we summarize those details of the analytical solution for leap-frogging that we need in the following stability analysis. In Sec.IV we write out the linear stability analysis of the canonically reduced system. Although one could have expected this to lead to four coupled ODEs, it turns out that these decouple into two independent systems of two ODEs. These two systems are very similar. In Sec.V we give a brief exposition of Floquet analysis with an eye to its application to our problem in Sec.VI. We evaluate the Floquet exponents numerically. We find that there is indeed a transition from linear instability to stability at a value $\alpha = \alpha_2 \approx 0.38197$. Deeper analysis reveals that $\alpha_2 = \phi^2$, where $\phi = \frac{1}{2}(\sqrt{5} - 1)$ is the golden ratio.

On the other hand, linear analysis does not shed light on Acheson's empirically found value of $\alpha_1 \approx 0.29$ where there seems to be a change-over from "disintegration" to "walkabout" instability. By precision numerical computations we show that one can find α-values close to 0.29 such that if the four-vortex problem is evolved forward in time, it is unstable to a "walkabout" instability mode, whereas if it is evolved backward in time, it goes directly into the "disintegration" instability mode. Both these computations can be reversed in time. This leads us to conclude that the transition around $\alpha = 0.29$ is not a simple, sharp transition in the same sense that the (linear) instability-to-stability transition at α_2 is.

In Sec.VII we consider the limit $\alpha \to 1$ in detail. In this limit we may analytically evaluate everything in the Floquet stability analysis.

Finally, Section VIII contains our conclusions.

II. EQUATIONS OF MOTION

We represent the vortices as points in the complex plane, with z_1^+ and z_2^+ the two positive vortices, z_1^- and z_2^- the two negative. The equations of motion of our point vortex system are

$$\begin{aligned}
\overline{\frac{\mathrm{d}z_1^+}{\mathrm{d}t}} &= \frac{\Gamma}{2\pi \mathrm{i}}\Big(\frac{1}{z_1^+ - z_2^+} - \frac{1}{z_1^+ - z_1^-} - \frac{1}{z_1^+ - z_2^-}\Big),\\
\overline{\frac{\mathrm{d}z_2^+}{\mathrm{d}t}} &= \frac{\Gamma}{2\pi \mathrm{i}}\Big(\frac{1}{z_2^+ - z_1^+} - \frac{1}{z_2^+ - z_1^-} - \frac{1}{z_2^+ - z_2^-}\Big),\\
\overline{\frac{\mathrm{d}z_1^-}{\mathrm{d}t}} &= \frac{\Gamma}{2\pi \mathrm{i}}\Big(\frac{1}{z_1^- - z_1^+} + \frac{1}{z_1^- - z_2^+} - \frac{1}{z_1^- - z_2^-}\Big),\\
\overline{\frac{\mathrm{d}z_2^-}{\mathrm{d}t}} &= \frac{\Gamma}{2\pi i}\Big(\frac{1}{z_2^- - z_1^+} + \frac{1}{z_2^- - z_2^+} - \frac{1}{z_2^- - z_1^-}\Big).
\end{aligned} \tag{1}$$

As with all point vortex problems this system is Hamiltonian.

We change to another set of variables by a canonical transformation due to Eckhardt & Aref[9]:

$$\begin{aligned}
\zeta_0 &= \tfrac{1}{2}\Gamma(z_1^+ + z_2^+ - z_1^- - z_2^-),\\
\hat{\zeta}_0 &= \tfrac{1}{2}(z_1^+ + z_2^+ + z_1^- + z_2^-),\\
\zeta_+ &= \tfrac{1}{2}(z_1^+ - z_2^+ + z_1^- - z_2^-),\\
\zeta_- &= \tfrac{1}{2}\Gamma(z_1^+ - z_2^+ - z_1^- + z_2^-).
\end{aligned} \tag{2a}$$

It is also useful to have the inverse transformation:

$$\begin{aligned}
z_1^+ &= \tfrac{1}{2}[\hat{\zeta}_0 + \zeta_+ + (\zeta_0 + \zeta_-)/\Gamma],\\
z_1^- &= \tfrac{1}{2}[\hat{\zeta}_0 + \zeta_+ - (\zeta_0 + \zeta_-)/\Gamma],\\
z_2^+ &= \tfrac{1}{2}[\hat{\zeta}_0 - \zeta_+ + (\zeta_0 - \zeta_-)/\Gamma],\\
z_2^- &= \tfrac{1}{2}[\hat{\zeta}_0 - \zeta_+ - (\zeta_0 - \zeta_-)/\Gamma].
\end{aligned} \tag{2b}$$

If we think of the configuration as consisting of two vortex pairs, (z_1^+, z_1^-) and (z_2^+, z_2^-), the intra-pair separations are $d_1 = z_1^+ - z_1^-$ and $d_2 = z_2^+ - z_2^-$. The vector connecting vortex pair centers, from pair (z_2^+, z_2^-) to pair (z_1^+, z_1^-), is ζ_+. The difference between the intra-pair separations, multiplied by Γ, is $\zeta_- = \frac{1}{2}\Gamma(d_1 - d_2)$. The quantity $\zeta_0 = \frac{1}{2}\Gamma(d_1 + d_2)$ is half the linear impulse of the system and is thus a constant of the motion. A sketch of the coordinates is shown in Fig.2.

The variables ζ_0 and $\hat{\zeta}_0$ are canonically conjugate in the sense that $\mathrm{Re}\,\zeta_0$ and $\mathrm{Im}\,\hat{\zeta}_0$ are canonically conjugate, as are $\mathrm{Re}\,\hat{\zeta}_0$ and $\mathrm{Im}\,\zeta_0$. Similarly, $\zeta_\pm$ are canonically conjugate. In particular, since ζ_0 is an integral of the motion, $\hat{\zeta}_0$ is a cyclic variable that does not appear in the Hamiltonian H. Geometrically $\hat{\zeta}_0$ is twice the centroid of the vortex positions. This point may be shifted by a translation of the coordinates which, since the vortex circulations sum to 0, does not change the value of the linear impulse, ζ_0, a property that we shall use in what follows. Since only relative positions of the vortices enter the equations of motion, it is intuitively clear that it should be possible to find a subset of equations that do not contain $\hat{\zeta}_0$. The canonical transformation in Eqs.(2a-b) achieves this formally.

Note that a configuration that has the real axis as a symmetry axis, such as the leapfrogging motions, i.e., for which $z_1^- = \overline{z_1^+}$, $z_2^- = \overline{z_2^+}$, must have ζ_+ real and ζ_- imaginary. Also note that if we had paired up the vortices as (z_2^+, z_1^-) and (z_1^+, z_2^-), we would, in essence, have interchanged the definitions of $\zeta_\pm$ (except for a factor of Γ). Hence, the equations of motion written in terms of $\zeta_\pm$ must display this symmetry.

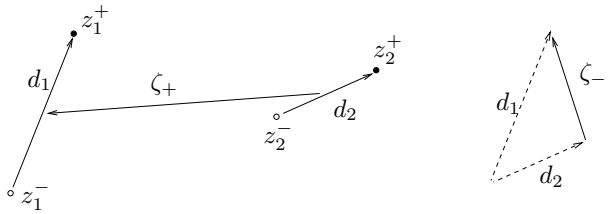

FIG. 2. Positive vortices are at z_1^+, z_2^+ in the complex plane, negative vortices at z_1^-, z_2^-. Also shown are $\zeta_\pm$, Eqs.(2a.

The canonical transformation implies that the equations for ζ_+ and ζ_- form a closed two-degree-of-freedom dynamical system, in which the constant ζ_0 enters as a parameter. According to Ref.9, Eq.(3.14), the Hamiltonian of this reduced system is

$$H = -\frac{\Gamma^2}{2\pi}\log\left|\frac{1}{\zeta_0^2 - \zeta_+^2} - \frac{1}{\zeta_0^2 - \zeta_-^2}\right|. \tag{3}$$

The resulting equations of motion are

$$\begin{aligned}
\overline{\frac{\mathrm{d}\zeta_+}{\mathrm{d}t}} &= \frac{\Gamma^2}{\mathrm{i}\pi}\zeta_-\left(\frac{1}{\zeta_-^2 - \zeta_+^2} + \frac{1}{\zeta_0^2 - \zeta_-^2}\right),\\
\overline{\frac{\mathrm{d}\zeta_-}{\mathrm{d}t}} &= \frac{\Gamma^2}{\mathrm{i}\pi}\zeta_+\left(\frac{1}{\zeta_+^2 - \zeta_-^2} + \frac{1}{\zeta_0^2 - \zeta_+^2}\right),
\end{aligned}$$

and also,

$$\overline{\frac{\mathrm{d}\hat{\zeta}_0}{\mathrm{d}t}} = \frac{\Gamma^2}{\mathrm{i}\pi}\zeta_0\left(\frac{1}{\zeta_+^2 - \zeta_0^2} + \frac{1}{\zeta_-^2 - \zeta_0^2}\right).$$

The case $\zeta_0 = 0$ is integrable[9] but not of particular interest for the present considerations. Assuming $\zeta_0 \neq 0$, we scale $\zeta_\pm$ and $\hat{\zeta}_0$ by $-i\zeta_0$, but again call the scaled variables $\zeta_\pm$ and $\hat{\zeta}_0$. This scaling guarantees that if the vortices initially are placed on the y-axis, so that the leapfrogging motion would propagate along the x-axis, then $\zeta_\pm$ and $\hat{\zeta}_0$ are proportional to their scaled counterparts with a real coefficient of proportionality. We now obtain a common pre-factor $\Gamma^2/\pi|\zeta_0|^2$ on the right hand sides of the preceding equations of motion. We may choose units of length and time such that this common pre-factor is 1. The re-scaled equations of motion are

then simply

$$\overline{\frac{\mathrm{d}\zeta_+}{\mathrm{d}t}} = \mathrm{i}\zeta_-\left(\frac{1}{\zeta_+^2-\zeta_-^2}+\frac{1}{1+\zeta_-^2}\right), \tag{4a}$$

$$\overline{\frac{d\zeta_-}{dt}} = \mathrm{i}\zeta_+\left(\frac{1}{\zeta_-^2-\zeta_+^2}+\frac{1}{1+\zeta_+^2}\right), \tag{4b}$$

$$\overline{\frac{\mathrm{d}\hat{\zeta}_0}{\mathrm{d}t}} = \frac{1}{1+\zeta_+^2}+\frac{1}{1+\zeta_-^2}. \tag{4c}$$

These may be derived from the re-scaled Hamiltonian, cf. (3),

$$H = -\tfrac{1}{2}\log\left|\frac{1}{1+\zeta_+^2}-\frac{1}{1+\zeta_-^2}\right|. \tag{5}$$

The simplest way to verify that (4a-b) are indeed in canonical form with H as the Hamiltonian is to consider the analytic continuation of H, *viz*,

$$\mathcal{H} = -\tfrac{1}{2}\log\left(\frac{1}{1+\zeta_+^2}-\frac{1}{1+\zeta_-^2}\right). \tag{6a}$$

It is then easy to see that Eqs.(4a-b) are simply

$$\overline{\frac{\mathrm{d}\zeta_+}{\mathrm{d}t}} = \mathrm{i}\frac{\partial\mathcal{H}}{\partial\zeta_-}, \qquad \overline{\frac{\mathrm{d}\zeta_-}{\mathrm{d}t}} = \mathrm{i}\frac{\partial\mathcal{H}}{\partial\zeta_+}. \tag{6b}$$

Using the analyticity of $\mathcal{H}$, and that $H = \mathrm{Re}\,\mathcal{H}$, we arrive at the standard Hamiltonian formulation of Eqs.(4a-b).

III. LEAPFROGGING SOLUTIONS

We consider leapfrogging motions along the real axis, where the vortices are originally aligned on the y-axis. For such motions ζ_0 is imaginary and, according to (2a), ζ_+ is real and ζ_- imaginary both before and after rescaling. In Eqs.(4a-b) we set

$$\zeta_+(t) = X(t), \qquad \zeta_-(t) = \mathrm{i}Y(t), \tag{7a}$$

with $X(t)$ and $Y(t)$ real. In terms of these quantities Eqs.(4a-b) become

$$\begin{aligned}\frac{\mathrm{d}X}{\mathrm{d}t} &= -\frac{Y(1+X^2)}{(X^2+Y^2)(1-Y^2)},\\ \frac{\mathrm{d}Y}{\mathrm{d}t} &= \frac{X(1-Y^2)}{(X^2+Y^2)(1+X^2)}.\end{aligned} \tag{7b}$$

The vortices in both pairs have the real axis as a common axis of symmetry. This discrete symmetry is preserved throughout the motion.

At the initial instant we have $\zeta_- = \frac{1}{2}\Gamma(d_1-d_2)$, $\zeta_0 = \frac{1}{2}\Gamma(d_1+d_2)$, where $d_{1,2}$ are both imaginary. In terms of the initial values $X(0)=X_0$ and $Y(0)=Y_0$

$$X_0 = 0, \qquad Y_0 = \frac{1-\alpha}{1+\alpha}, \tag{8}$$

where $\alpha = d_2/d_1$ is the (real) pair separation ratio at $t=0$.

Equations (7b) are nonlinear but integrable by virtue of the existence of an integral of motion, the Hamiltonian, given by (5) specialized to (7a), or

$$H = -\tfrac{1}{2}\log\big(\frac{1}{1-Y^2}-\frac{1}{1+X^2}\big). \tag{9a}$$

The integral takes the form

$$\frac{(1+X^2)(1-Y^2)}{X^2+Y^2} = h = \mathrm{e}^{2H}, \tag{9b}$$

which may also be written

$$(X^2+h+1)(Y^2+h-1) = h^2. \tag{9c}$$

The connection between α and h is given by

$$\frac{4\alpha}{(1-\alpha)^2} = h. \tag{9d}$$

It is easy to verify that

$$\dot{X} = \frac{\partial H}{\partial Y}, \qquad \dot{Y} = -\frac{\partial H}{\partial X}. \tag{9e}$$

We note that the equations of motion (7b) can be written

$$\frac{\mathrm{d}X}{\mathrm{d}t} = -\frac{hY}{(1-Y^2)^2}, \qquad \frac{\mathrm{d}Y}{\mathrm{d}t} = \frac{hX}{(1+X^2)^2}. \tag{7b$'$}$$

Level curves of H, Eq.(9a), are plotted in Fig.3. (An equivalent figure appears also in Love's paper[4] at the end of §4.) Close to $(X,Y)=(0,0)$ these curves are circles $X^2+Y^2 \approx h^{-1}$. This limit corresponds to $h\to\infty$ or $\alpha\to 1$. We explore it further in Sec.VII.

In order for a curve (9b) to be closed, we must be able to solve (9b) for X when $Y=0$. This implies $h>1$, and all the level curves (9b) for $1<h<\infty$ are closed and lead to leapfrogging motions. The lower limit $h=1$ corresponds via (9d) to $\alpha=\alpha_0=3-2\sqrt{2}$. The range in α to be explored, and to which we restrict attention, is then

$$3-2\sqrt{2} < \alpha < 1. \tag{10}$$

The determination of the the lower limit of this range, $\alpha_0=\sigma^2$, is a key result of the classical analyses[3,4]. See also Appendix B of Ref.9 for a development of this material in a notation more similar to that used here.

The period T_{lf} of the leapfrogging motion is given by Love[4] in terms of elliptic integrals. In the present notation, and using the re-scaled time scale occuring in (7b), we have

$$T_{lf} = 2^6\frac{\alpha^2}{(1-\alpha)^2}\left[\frac{E(k^2)}{(6\alpha-\alpha^2-1)}-\frac{K(k^2)}{(1+\alpha)^2}\right], \tag{11}$$

where $k^2 \equiv -2^4\alpha(1+\alpha)^2(1-\alpha)^{-4}$, and K and E are the complete elliptic integrals of the first and second kind, respectively.

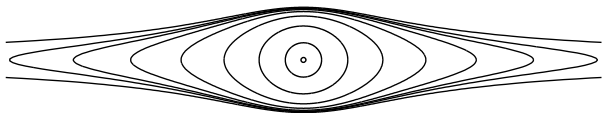

FIG. 3. Level curves of the Hamiltonian (9a).

IV. LINEAR STABILITY THEORY

Within the framework of Eqs.(4a-b) we now consider perturbations to the periodic motion described in Sec.III of the form

$$\begin{aligned}\zeta_+(t) &= X(t) + \epsilon[\xi_+(t) + \mathrm{i}\eta_+(t)],\\ \zeta_-(t) &= iY(t) + \epsilon[\xi_-(t) + \mathrm{i}\eta_-(t)],\end{aligned} \tag{12}$$

where ϵ is small and determines the size of the perturbation. All the functions $X, Y, \xi_\pm$, and $\eta_\pm$ appearing here are real.

The most transparent way to derive the linearized perturbation equations is to start from Eqs.(6b) and expand to linear order. This gives

$$\begin{aligned}&\dot\xi_+ - \mathrm{i}\dot\eta_+ = \\ &\quad \mathrm{i}\frac{\partial^2\mathcal{H}}{\partial\zeta_-^2}(\xi_- + \mathrm{i}\eta_-) + \mathrm{i}\frac{\partial^2\mathcal{H}}{\partial\zeta_+\partial\zeta_-}(\xi_+ + \mathrm{i}\eta_+),\\ &\dot\xi_- - \mathrm{i}\dot\eta_- = \\ &\quad \mathrm{i}\frac{\partial^2\mathcal{H}}{\partial\zeta_+^2}(\xi_+ + \mathrm{i}\eta_+) + \mathrm{i}\frac{\partial^2\mathcal{H}}{\partial\zeta_-\partial\zeta_+}(\xi_- + \mathrm{i}\eta_-).\end{aligned} \tag{13a}$$

The derivatives of $\mathcal{H}$ for the base solution, $\zeta_+ = X$, $\zeta_- = \mathrm{i}Y$, are:

$$\begin{aligned}\frac{\partial^2\mathcal{H}}{\partial\zeta_-^2} &= -\frac{\partial^2 H}{\partial Y^2} = -H_{YY},\\ \frac{\partial^2\mathcal{H}}{\partial\zeta_+^2} &= \frac{\partial^2 H}{\partial X^2} = H_{XX},\\ \frac{\partial^2\mathcal{H}}{\partial\zeta_-\partial\zeta_+} &= -i\frac{\partial^2 H}{\partial X\partial Y} = -iH_{XY}.\end{aligned} \tag{13b}$$

The components of the *Hessian* of H,

$$\mathcal{W} = \begin{bmatrix} H_{XX} & H_{XY}\\ H_{YX} & H_{YY}\end{bmatrix}, \tag{13c}$$

are, of course, all real. Explicitly,

$$H_{XY} = H_{YX} = \frac{2XY}{(X^2+Y^2)^2}, \tag{14a}$$

and

$$H_{XX} = F(\mathrm{i}Y, X), \qquad H_{YY} = -F(X, \mathrm{i}Y), \tag{14b}$$

where

$$F(Z_1, Z_2) = \frac{(1+Z_1^2)(3Z_2^4 - Z_1^2Z_2^2 + Z_1^2 + Z_2^2)}{(1+Z_2^2)^2(Z_1^2 - Z_2^2)^2}. \tag{14c}$$

Separating (13a) into real and imaginary parts, we now see that the perturbations decouple into two independent systems of equations for two variables each:

$$\frac{d}{dt}\begin{bmatrix}\xi_+\\ \eta_-\end{bmatrix} = \begin{bmatrix} H_{XY} & H_{YY}\\ -H_{XX} & -H_{XY}\end{bmatrix}\begin{bmatrix}\xi_+\\ \eta_-\end{bmatrix}, \tag{15a}$$

$$\frac{d}{dt}\begin{bmatrix}\xi_-\\ \eta_+\end{bmatrix} = \begin{bmatrix} H_{XY} & -H_{XX}\\ H_{YY} & -H_{XY}\end{bmatrix}\begin{bmatrix}\xi_-\\ \eta_+\end{bmatrix}. \tag{15b}$$

We note that the coefficient matrix appearing in the second of these is

$$\begin{bmatrix} H_{XY} & -H_{XX}\\ H_{YY} & -H_{XY}\end{bmatrix} = \mathcal{W}\mathcal{E},$$

where

$$\mathcal{E} = \begin{bmatrix} 0 & -1\\ 1 & 0\end{bmatrix} \tag{16}$$

We note for later use that $\mathcal{E}^2 = -\mathbf{1}$.

The coefficient matrix appearing in Eqs.(15a) is the transpose:

$$\begin{bmatrix} H_{XY} & H_{YY}\\ -H_{XX} & -H_{XY}\end{bmatrix} = (\mathcal{W}\mathcal{E})^T = \mathcal{E}^T\mathcal{W} = -\mathcal{E}\mathcal{W}.$$

The perturbation equations may thus be written in the form

$$\frac{\mathrm{d}}{\mathrm{d}t}\begin{bmatrix}\xi_+\\ \eta_-\end{bmatrix} = -\mathcal{E}\mathcal{W}\begin{bmatrix}\xi_+\\ \eta_-\end{bmatrix}, \qquad \frac{\mathrm{d}}{\mathrm{d}t}\begin{bmatrix}\xi_-\\ \eta_+\end{bmatrix} = \mathcal{W}\mathcal{E}\begin{bmatrix}\xi_-\\ \eta_+\end{bmatrix}, \tag{17}$$

where $\mathcal{W}$ is the Hessian (13c) and $\mathcal{E}$ is given by (16). The following explicit form is also important

$$\frac{d}{dt}\begin{bmatrix}\xi_+\\ \eta_-\end{bmatrix} = \mathcal{A}^T\begin{bmatrix}\xi_+\\ \eta_-\end{bmatrix}, \qquad \frac{d}{dt}\begin{bmatrix}\xi_-\\ \eta_+\end{bmatrix} = \mathcal{A}\begin{bmatrix}\xi_-\\ \eta_+\end{bmatrix}, \tag{18a}$$

where

$$\mathcal{A} = g(X,Y)\begin{bmatrix} XY & f(iY,X)\\ f(X,iY) & -XY\end{bmatrix}, \tag{18b}$$

with (cf. (14a))

$$g(X,Y) = \frac{2}{(X^2+Y^2)^2}, \tag{18c}$$

and (cf. (14c))

$$f(Z_1,Z_2) = -\tfrac{1}{2}(Z_1^2 - Z_2^2)^2 F(Z_1,Z_2). \tag{18d}$$

Since $g(X,Y) > 0$ it may be absorbed into a rescaling of time via $d\tau = g(X,Y)dt$.

Formally the equations for (ξ_+, η_-) and (ξ_-, η_+) appear to be quite similar. There is, however, an important difference in terms of the physics between the two types of perturbations: The (ξ_+, η_-) perturbations preserve the discrete symmetry of the leapfrogging motion since ζ_+ remains real and ζ_- imaginary. In other words, infinitesimal perturbations of this kind must lead from

one leapfrogging motion to another. The (ξ_-, η_+) perturbations break the discrete symmetry. Hence, it is among these perturbations that we are to seek potential instabilities of leapfrogging motion.

By construction all perturbations (ξ_+, η_-) and (ξ_-, η_+) conserve the linear impulse ζ_0. The change in the analytic continuation of the Hamiltonian, $\mathcal{H}$ in Eq.(6a), for a general perturbation (12) is

$$\begin{aligned}\delta\mathcal{H} =& H_X(\xi_+ + \mathrm{i}\eta_+) - \mathrm{i}H_Y(\xi_- + \mathrm{i}\eta_-) = \\ & H_X\xi_+ + H_Y\eta_- + \mathrm{i}(H_X\eta_+ - H_Y\xi_-).\end{aligned}$$

This is pure imaginary for perturbations with $\xi_+ = \eta_- = 0$ which shows that to leading order there is no change in the real part of $\mathcal{H}$, in other words no change in H, Eq.(5), for a (ξ_-, η_+)-perturbation. The (ξ_+, η_-) perturbations will in general change H, the one exception being a perturbation along $(H_Y, -H_X)$, i.e., along $(\dot{X}, \dot{Y})$. As we shall see, such perturbations are, in fact, solutions of the linearized equations (15a).

Turning to the angular impulse, we have

$$\begin{aligned}I &= \Gamma(|z_1^+|^2 + |z_2^+|^2 - |z_1^-|^2 - |z_2^-|^2) \\ &= 2\mathrm{Re}\,(\hat{\zeta}_0\overline{\zeta_0} + \zeta_+\overline{\zeta_-}),\end{aligned}$$

according to Eq.(3.15) of Ref.9. After rescaling this becomes $I = 2\mathrm{Im}(\hat{\zeta}_0) + 2\mathrm{Re}\,(\zeta_+\overline{\zeta_-})$. The change in I to first order in a perturbation of the form (12) is:

$$\begin{aligned}\delta I &= 2\mathrm{Im}(\delta\hat{\zeta}_0) + 2\mathrm{Re}\,[-\mathrm{i}Y(\xi_+ + \mathrm{i}\eta_+) + X(\xi_- - \mathrm{i}\eta_-)] \\ &= 2\mathrm{Im}(\delta\hat{\zeta}_0) + 2(X\xi_- + Y\eta_+).\end{aligned}$$

Thus, (ξ_+, η_-)-perturbations automatically preserve I. For (ξ_-, η_+)-perturbations we may preserve I if we agree to move the origin of coordinates, i.e., shift $\delta\hat{\zeta}_0$, such that $\delta I = 0$ for the perturbed initial state. This is possible since $\hat{\zeta}_0$ is simply twice the geometrical centroid of the four points where the vortices are located. Such a shift of the origin of coordinates has no effect on the value of the linear impulse or the Hamiltonian, and the value of $\hat{\zeta}_0$ does not enter into the dynamical equations for $\zeta_\pm$. Perturbations (ξ_-, η_+) along $(-Y, X)$ preserve I without need for shifting the origin of coordinates.

In summary, then, the perturbations (ξ_-, η_+) may be considered to take place at fixed values of the integrals of motion H and I. The perturbations (ξ_+, η_-) have a one-dimensional subspace that does not conserve H.

V. FLOQUET ANALYSIS

Exploring the solutions to a system such as (17) leads us directly to *Floquet theory.*[7] Due to the periodic time dependence of the coefficient matrix, the behavior of solutions is not immediately given by the local behavior of the solutions but rather by these solutions integrated over a period of the periodic motion. In effect, Floquet theory exploits the properties of the *return map* of the linear system integrated over a period of the motion whose stability is the object of study. We outline the basics of the theory in order to establish our notation and emphasize what we need in the present case. The theory is treated in several places in the literature, e.g., Ref.8.

We are dealing with a general system of ODEs of the form

$$\dot{\boldsymbol{\xi}} = \mathcal{A}\boldsymbol{\xi}, \tag{19}$$

where $\boldsymbol{\xi}$ is a two-component vector and $\mathcal{A}$ a 2×2 matrix that is periodic in time. We shall apply the theory to both the (ξ_+, η_-)- and (ξ_-, η_+)-perturbations of the preceding section.

Construct a so-called *fundamental matrix*, Ξ, by placing in the first column the solution $\boldsymbol{\xi} = (\xi, \eta)$ to (19) with initial condition $(1, 0)$. In the second column place the solution with initial condition $(0, 1)$. The 2×2 matrix, Ξ then satisfies the equation of evolution

$$\dot{\Xi} = \mathcal{A}\Xi. \tag{20}$$

If $\mathcal{A}$ were constant in time, the solution would be easy enough:

$$\Xi(t) = \mathrm{e}^{\mathcal{A}t}\Xi(0).$$

If $\mathcal{A}$ has eigenvalues $\mu_{1,2}$ with corresponding eigenvectors $\boldsymbol{v}^{(1,2)}$, we have

$$\mathcal{A}\boldsymbol{v}^{(1,2)} = \mu_{1,2}\boldsymbol{v}^{(1,2)}, \qquad \mathrm{e}^{\mathcal{A}t}\boldsymbol{v}^{(1,2)} = \mathrm{e}^{\mu_{1,2}t}\boldsymbol{v}^{(1,2)}.$$

Hence, expanding $\boldsymbol{\xi}(0)$ along $\boldsymbol{v}^{(1,2)}$, we obtain solution components that vary as $\mathrm{e}^{\mu_{1,2}t}$. If $\mu_{1,2}$ is pure imaginary, this leads to oscillatory evolution and thus spectral stablity. On the other hand, if either of $\mu_{1,2}$ has a positive real part, we obtain unstable exponential growth of the perturbation.

For a time-periodic coefficient matrix we must proceed a bit differently: We exploit the periodicity of $\mathcal{A}$ with some period, T, to argue that if $\Xi(t)$ is a solution of (20), then $\Xi(t + T)$ will also be a solution. Next, since the space of solution vectors is two-dimensional, the columns of $\Xi(t+T)$ may be expressed as linear combinations of the columns of $\Xi(t)$. In other words, there exists a matrix, M, called the *monodromy matrix*, such that

$$\Xi(t + T) = \Xi(t)M. \tag{21a}$$

With the two independent solutions we have chosen, we have $\Xi(0) = \mathbf{1}$, the 2×2 unit matrix. Hence,

$$M = \Xi(T), \qquad \Xi(t + T) = \Xi(t)\Xi(T). \tag{21b}$$

If we wish to find the solution $\hat{\Xi}(t)$ starting from general initial conditions $\hat{\Xi}(0) = \mathcal{C}$, we have only to set $\hat{\Xi}(t) = \Xi(t)\mathcal{C}$. Then,

$$\dot{\hat{\Xi}} = \dot{\Xi}\mathcal{C} = \mathcal{A}\Xi\mathcal{C} = \mathcal{A}\hat{\Xi},$$

so $\hat{\Xi}$ satisfies the ODE, and by construction $\hat{\Xi}(0) = \mathcal{C}$.

A word of caution is necessary if $\Xi(t)$ becomes degenerate. Indeed, the term "fundamental matrix" is usually reserved for the case when $\Xi(t)$ is non-degenerate. If the columns of $\Xi(t)$ become proportional, we must supplement the first column vector by a perpendicular vector to have a basis in the 2D space. The general theory is then somewhat modified. We continue with the assumption that $\Xi(t)$ is non-degenerate for $0 \le t \le T$ and return to the degenerate case as necessary.

Let $\boldsymbol{v}^{(\pm)}$ be the eigenvectors of M corresponding to eigenvalues $\rho_\pm$, respectively, i.e., $M\boldsymbol{v}^{(\pm)} = \rho_\pm \boldsymbol{v}^{(\pm)}$. It is important to emphasize that $\rho_\pm$ and $\boldsymbol{v}^{(\pm)}$ are time independent quantities. Important properties of $\rho_\pm$ follow from the identity

$$\frac{\mathrm{d}}{\mathrm{d}t}\det\Xi = \mathrm{Tr}\mathcal{A}\det\Xi. \tag{22}$$

This is, essentially, the relation for change of area in the 2D "flow" (20) and is, in any event, not difficult to verify. In our case the coefficient matrix $\mathcal{A}$ is either $\mathcal{W}\mathcal{E}$ or its transpose. Both have vanishing trace, so the right hand side of (22) vanishes, and $\det\Xi$ is invariant in time. Since $\det\Xi(0) = 1$, we have $\det M = \det\Xi(T) = 1$ and thus $\rho_+\rho_- = 1$. Furthermore, in our case the vectors and matrices are all real. In particular, the matrix M is real and its eigenvalues are thus either both real (in which case they have the form $\rho_\pm = \rho^{\pm 1}$ for some real ρ), or they are complex conjugates (in which case they have the form $\rho_\pm = \mathrm{e}^{\pm i\varphi}$ for some angle φ).

Now consider the time-dependent vectors

$$\boldsymbol{\xi}^{(\pm)}(t) = \Xi(t)\boldsymbol{v}^{(\pm)}. \tag{23}$$

We have

$$\dot{\boldsymbol{\xi}}^{(\pm)} = \dot{\Xi}\boldsymbol{v}^{(\pm)} = \mathcal{A}\Xi\boldsymbol{v}^{(\pm)} = \mathcal{A}\boldsymbol{\xi}^{(\pm)},$$

so the $\boldsymbol{\xi}^{(\pm)}(t)$ are solutions to the ODEs (19). They have the initial values $\boldsymbol{\xi}^{(\pm)}(0) = \boldsymbol{v}^{(\pm)}$. We see that

$$\begin{aligned}\boldsymbol{\xi}^{(\pm)}(t+T) &= \Xi(t+T)\boldsymbol{v}^{(\pm)} = \\ &\Xi(t)M\boldsymbol{v}^{(\pm)} = \rho_\pm\Xi(t)\boldsymbol{v}^{(\pm)} = \rho_\pm\boldsymbol{\xi}^{(\pm)}(t).\end{aligned} \tag{24}$$

Thus, over a period of the coefficient matrix $\mathcal{A}$ the solutions $\boldsymbol{\xi}^{(\pm)}$ are multiplied by $\rho_\pm$, respectively. The general solution to the functional relation (24) is

$$\boldsymbol{\xi}^{(\pm)}(\tau) = \rho_\pm^{\tau/T}\boldsymbol{\Pi}_\pm(\tau), \tag{25}$$

where the arbitrary function $\boldsymbol{\Pi}_\pm(\tau)$ is periodic with period T and satisfies $\boldsymbol{\Pi}_\pm(0) = \boldsymbol{v}^{(\pm)}$. A direct proof that $\boldsymbol{\Pi}_\pm(\tau)$ is periodic follows:

$$\begin{aligned}\boldsymbol{\Pi}_\pm(\tau+T) &= \rho_\pm^{-(\tau+T)/T}\boldsymbol{\xi}^{(\pm)}(\tau+T) = \\ &\rho_\pm^{-(\tau+T)/T}\rho_\pm\boldsymbol{\xi}^{(\pm)}(\tau) = \rho_\pm^{-\tau/T}\boldsymbol{\xi}^{(\pm)}(\tau) = \boldsymbol{\Pi}_\pm(\tau).\end{aligned}$$

The quantities $\rho_\pm$ are called the *Floquet multipliers*. One often sets $\rho_\pm = \mathrm{e}^{\mu_\pm T}$, even though the $\mu_\pm$ are defined only up to multiples of $2\pi i/T$. The $\mu_\pm$ are called the *Floquet exponents*.

If $\rho_\pm$ are reciprocal real numbers, we have found a solution to (19) that grows exponentially. The underlying periodic motion from which these equations arose as linear perturbations is then unstable. If $\rho_\pm$ are complex conjugates of modulus 1, the motion is linearly stable. A general initial condition may be decomposed along $\boldsymbol{v}^{(\pm)}$:

$$\boldsymbol{\xi}(0) = a_+\boldsymbol{v}^{(+)} + a_-\boldsymbol{v}^{(-)},$$

and so will evolve according to

$$\begin{aligned}\boldsymbol{\xi}(\tau) = a_+\boldsymbol{\xi}^{(+)}(\tau) + a_-\boldsymbol{\xi}^{(-)}(\tau) = \\ a_+\rho_+^{\tau/T}\boldsymbol{\Pi}^{(+)}(\tau) + a_-\rho_-^{\tau/T}\boldsymbol{\Pi}^{(-)}(\tau).\end{aligned}$$

VI. FLOQUET ANALYSIS APPLIED TO THE EQUATIONS OF SEC.IV

We now adapt the general theory to our perturbation equations for the leapfrogging motion. First, concerning the period, T, of the coefficient matrices, $-\mathcal{E}\mathcal{W}$ and $\mathcal{W}\mathcal{E}$ in Eqs.(17), we see that this must be *half* the period of the leapfrogging motion T_{lf}, (11). We start at $X = 0$ and some finite value of Y. During an entire cycle of the leapfrogging motion X and Y vary through positive and negative values. However, all the quantities H_{XX}, H_{XY}, H_{YY} appearing in the coefficient matrices of the stability problem are even functions of X and Y. Hence, the period of the matrices is half the leapfrogging period.

Let us first consider the (ξ_+, η_-) equations even though these are not of primary interest to the stability of leapfrogging. There is one obvious solution to these equations: If we differentiate Eqs.(9e) once more with respect to time, we get

$$\ddot{X} = H_{YX}\dot{X} + H_{YY}\dot{Y}, \qquad \ddot{Y} = -H_{XX}\dot{X} - H_{XY}\dot{Y}.$$

Written in matrix form, these equations show that $(\xi_+, \eta_-) = (\dot{X}, \dot{Y})$ solve Eqs.(15a).

The initial conditions (8) for leapfrogging imply

$$\dot{X}(0) = \frac{-1}{hY_0^3}, \qquad \dot{Y}(0) = 0. \tag{26}$$

This follows from (7b) or (7b′) and (9b) when the values from (8) are substituted. It is also clear from Fig.3 that $\dot{Y}(0)$ vanishes and that $\dot{X}(0)$ is negative: The leapfrogging motion starts at a point on the positive Y-axis of Fig.3 as given by Eqs.(8). Since the level curves all have horizontal tangents on this axis, a (ξ_+, η_-)-perturbation of the initial condition that has only an X-component will simply move the phase point a bit forward or backward along the chosen trajectory, i.e., lead to a leapfrogging motion with the same value of the Hamiltonian.

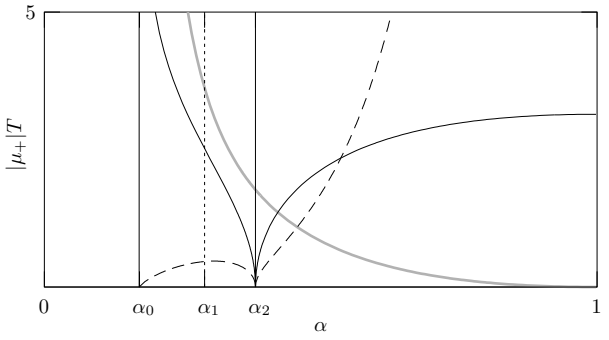

FIG. 4. Floquet exponents as a function of α shown for $\alpha_0 < \alpha \leq \alpha_2$. See the text for these values of α. The dashed curve shows $2|\mu_+|$, the thick grey curve shows $T/3$, cf. (11), and the solid curve shows $|\mu_+|T$. Note that μ_+ is purely real for $\alpha < \alpha_2$ and purely imaginary for $\alpha_2 < \alpha < 1$, indicating that the monodromy matrix has complex conjugate eigenvalues of unit modulus in the latter range.

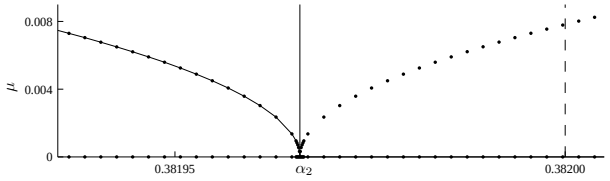

FIG. 5. Detail of the Floquet exponent μ_+ around $\alpha = \alpha_2 = \phi^2$. For $\alpha < \alpha_2$, where μ_+ is imaginary, we show μ_+/i. The dashed line at $\alpha = 0.382$ shows Acheson's numerically determined value for the cross-over from unstable to stable leapfrogging[5]. The text provides further discussion.

At time T the perturbation $(\dot{X}, \dot{Y})$ will have evolved into $(\dot{X}(T), \dot{Y}(T)) = (-\dot{X}(0), 0)$. In other words, the (ξ_+, η_-)-perturbation that at $t = 0$ is $(1, 0)$ must, by linearity, have evolved into $(-1, 0)$ at time $t = T$. This gives the first column of the monodromy matrix M.

Next, from the determinant of the monodromy matrix being $+1$ we know that the lower diagonal element must also be -1. Hence, we have the form of the monodromy matrix for the (ξ_+, η_-) equations:

$$M = \begin{bmatrix} -1 & A \\ 0 & -1 \end{bmatrix}. \tag{27}$$

To find the number A, we proceed as follows. We consider a perturbation with initial condition $(\xi_+, \eta_-) = (0, 1)$ of a state with initial condition $(X, Y) = (0, Y_0)$. This effectively take us to another leapfrogging motion with initial condition $(X, Y) = (0, Y_0 + \epsilon)$. Now, the leapfrogging period has increased by an amount $\mathrm{d}T_{lf} = \epsilon \partial T_{lf}/\partial Y_0$, which can be computed from (8) and (11). So after a time $T = T_{lf}/2$, the perturbed system will be a time $\mathrm{d}T_{lf}/2$ behind reaching its own half-period. To first order in ϵ, the system will have evolved to $(X, Y) = (-\mathrm{d}T_{lf}\dot{X}(T)/2, -Y_0 - \epsilon)$. Since the perturbation governed by (15a) must evolve in agreement with this result to linear order in ϵ, we will have $(\xi_+, \eta_-) = (-\mathrm{d}T_{lf}\dot{X}(T)/2, -1)$ at time T. Now, $\dot{X}(T) = -\dot{X}(0)$, so

$$A = \frac{1}{2}\frac{\partial T_{lf}}{\partial Y_0}\dot{X}(0), \tag{28}$$

with $A < 0$. The result (27, 28) shows that leapfrogging is always stable to (ξ_+, η_-) perturbations, as we have already argued. Also, it has been useful in checking our numerical procedure for evaluating the monodromy matrix.

It is straightforward to compute the Floquet exponents for the leapfrogging motion numerically. We have done so as a function of the parameter α in the initial condition (8). The classical leapfrogging solution is required. This solution is given in terms of elliptic functions[3,4] that would, in any event, require numerical evaluation. It is therefore easier operationally, and just as accurate, to simply solve the ODEs (7b) numerically along with the stability equations (17) such that $X(t)$ and $Y(t)$ are available at each step. We have used the Runge-Kutta 45 solver in the software package *MATLAB*® for this purpose.

For the (ξ_+, η_-)-equations the numerical calculations simply verify the result in (27, 28). The Floquet analysis calculation for the (ξ_-, η_+)-equations is more interesting. The results have been collected in Fig.4 which shows both $\mu_+ T$ and μ_+ as functions of α. The relevant interval is $\alpha_0 < \alpha < 1$. In this interval $\alpha_0 = \sigma^2 \approx 0.172$ marks the onset of leapfrogging. Since $T \to \infty$ as $\alpha \to \alpha_0$, we have plotted both μ_+ and $\mu_+ T$ in Fig. 4 as functions of α. We see that for a range of α, from the onset of leapfrogging to $\alpha = \alpha_2 \approx 0.382$, we have a real, positive Floquet exponent corresponding to instability. The Floquet exponent μ_+ vanishes at $\alpha = \alpha_0$ and at $\alpha = \alpha_2$. Beyond $\alpha = \alpha_2$ the Floquet exponents become pure imaginary. The positive imaginary part, $\mathrm{Im}\,\mu_+ T$, has been plotted in Fig.4. Again, since $T \to 0$ for $\alpha \to 1$, we have also plotted $\mathrm{Im}\,\mu_+$. Figure 5 shows a magnification of the region close to $\alpha = \alpha_2$. The vertical line is at $\alpha_2 = 0.38197\ldots$, which we determine analytically in the sequel. This value agrees to three decimal places with the value found by Acheson[5] using direct numerical experiments. It also agrees to all decimal places with the value of ϕ^2, where ϕ is the golden ratio. The numerical result motivates the analytical argument that the zero Floquet exponent, in fact, occurs for $\alpha = \phi^2$ given below.

The Floquet exponent plot shows an inflection point, at $\alpha = \alpha_1 \approx 0.29$, approximately the point where Acheson[5] noticed a transition from the "walkabout" to the disintegration mode of instability by numerical experiments. However, it is optimistic to expect a linearized analysis to detect a cross-over between two modes of finite-amplitude instability. Furthermore, our numerical investigation shows that the transition from "walkabout" to disintegration mode is not sharp in the same sense as the transition at $\alpha = \alpha_2$. Fig.6 shows an orbit of two vortex pairs scattering off each other

through an intermediate stage of leapfrogging motion. This is similar to scattering processes discussed in Ref. 6. The orbit realised in Fig.6 was realised by integrating both forward and backward in time from a perturbed leapfrogging state with $\alpha = 0.25$. The two directions are equivalent, in the sense that moving backwards in time from a state perturbed by (ξ_-, η_+) corresponds to moving forward from a different perturbation $(\xi_-, -\eta_+)$. This shows that one single leapfrogging state can be pushed into either the "walkabout" or the "disintegration" instability mode by different small perturbations.

We proceed to give a tentative argument as to the exact value of the α_2 marking the transition to instability. Consider a set of trajectories of the form, cf. (25),

$$\boldsymbol{\xi}(\tau, \alpha) = e^{\mu(\alpha)\tau}\boldsymbol{\Pi}(\tau, \alpha),$$

as a one-parameter family of curves in $\mathbb{R}^2$ by the parameter α. μ is one of the Floquet exponents, and $\boldsymbol{\Pi}$ is periodic. We boldly assume the function $\boldsymbol{\xi}_\alpha$, where subscript denotes differentiation, exists, in which case

$$\boldsymbol{\xi}_\alpha = \tau\mu_\alpha\boldsymbol{\xi} + e^{\mu\tau}\boldsymbol{\Pi}. \tag{29}$$

Now, it is clear that $\mu(\alpha)$ undergoes a sharp transition at $\alpha = \alpha_2$, with distinct limiting values of the derivative μ_α on either side of the transition point. From Fig. 4, we see that μ_α diverges, so we expect $\boldsymbol{\xi}_\alpha$, (29), to change dramatically at the transition point. If we differentiate (19) with respect to α, we obtain

$$\dot{\boldsymbol{\xi}}_\alpha = \mathcal{A}_\alpha\boldsymbol{\xi} + \mathcal{A}\boldsymbol{\xi}_\alpha, \tag{30}$$

This dynamical system is identical to the one governing the evolution of $\boldsymbol{\xi}$, except for the forcing term $\mathcal{A}_\alpha\boldsymbol{\xi}$.

We are thus naturally led to examine the behaviour of the matrix $\mathcal{A}_\alpha$. In particular the determinant $|\mathcal{A}_\alpha|$ will be of interest. We note that $|\mathcal{A}_\alpha|$ is a smooth function of time and periodic with period T. It has two distinct regimes for $\alpha_0 < \alpha < 1$, with the transition taking place for a particular value of α, say $\alpha = \alpha_2'$. For $\alpha < \alpha_2'$, $|\mathcal{A}_\alpha|$ changes sign twice during one period. For $\alpha_2' < \alpha$, $|\mathcal{A}_\alpha|$ is positive throughout the period. So α_2' marks a distinct change in the character of the forcing term in (30). The cross-over takes place at the time corresponding to $X = 0$, so we can determine α_2' by differentiating the matrix

$$\begin{bmatrix} XY & f(iY, X) \\ f(X, iY) & -XY \end{bmatrix},$$

cf. (18b), with respect to Y at $X = 0$ (which is equivalent to differentiating with respect to Y_0, and so with respect to α), we find after a brief calculation

$$\frac{\partial}{\partial Y}\begin{bmatrix} XY & f(iY, X) \\ f(X, iY) & -XY \end{bmatrix}_{X=0} = \begin{bmatrix} 0 & \frac{Y_0(1-5Y_0^2)}{(1-Y_0^2)^3} \\ Y_0(1-2Y_0^2) & 0 \end{bmatrix}.$$

Thus, in order for $\mathcal{A}_\alpha$ to have a null vector we find the necessary condition

$$(1 - 2Y_0^2)(1 - 5Y_0^2) = 0.$$

In other words,

$$Y_0 = \frac{1}{\sqrt{2}} \qquad \text{or} \qquad Y_0 = \frac{1}{\sqrt{5}}. \tag{31}$$

These translate into the values $\alpha = \alpha_0 = \sigma^2$ and $\alpha = \alpha_2' = \phi^2$, respectively.

The latter corresponds to a high precision to the transition point located by numerical methods, cf. Figs.4 and 5. It seems the change in the forcing term, i.e. in $|\mathcal{A}_\alpha|$ is somehow critical in determining the transition to instability, and the range $\alpha_2' < \alpha$ with $|\mathcal{A}_\alpha| \gtrless 0$ corresponds to linearly stable leapfrogging. We thus speculate that $\alpha_2 = \alpha_2'$.

VII. THE $\alpha \to 1$ LIMIT

When $\alpha \to 1$ the two positive and the two negative vortices are close and orbit one another in bound states, effectively producing a vortex pair with strengths $\pm 2\Gamma$. In this limit X^2 and Y^2 are $\ll 1$. Thus Eqs.(7b) reduce to

$$\frac{\mathrm{d}X}{\mathrm{d}t} = -\frac{Y}{X^2 + Y^2}, \qquad \frac{\mathrm{d}Y}{\mathrm{d}t} = \frac{X}{X^2 + Y^2}. \tag{32}$$

One consequence of Eqs.(32) is that X^2+Y^2 is a constant. From its initial value (8), and to leading order in $1 - \alpha$,

$$X^2 + Y^2 = \tfrac{1}{4}(1 - \alpha)^2 = \frac{1}{h}.$$

From the definition of $g(X, Y)$, Eq.(18c), we then have $d\tau = 2h^2 dt$. In this limit t and re-scaled time, τ, are proportional. The solution to Eqs.(32) that satisfies the initial conditions (8) is

$$X(t) = -\frac{\sin(ht)}{\sqrt{h}}, \qquad Y(t) = \frac{\cos(ht)}{\sqrt{h}}. \tag{33}$$

In the system matrix (18b) we now get

$$XY = -\frac{\sin(2ht)}{2h}. \tag{34a}$$

Also, to lowest order in $1 - \alpha$, we find

$$f(X, iY) = f(X, iY) \approx -\tfrac{1}{2}(X^2 - Y^2) = \frac{\cos(2ht)}{2h}. \tag{34b}$$

Thus, Eqs.(15b) read

$$\frac{\mathrm{d}}{\mathrm{d}t}\begin{bmatrix} \xi_- \\ \eta_+ \end{bmatrix} = \omega\begin{bmatrix} -\sin(2\omega t) & \cos(2\omega t) \\ \cos(2\omega t) & \sin(2\omega t) \end{bmatrix}\begin{bmatrix} \xi_- \\ \eta_+ \end{bmatrix}. \tag{35}$$

This matrix has periodicity $T = \pi/\omega$ in t. Unfortunately, the $\alpha \to 1$ limit corresponds to a special case of the general theory in Sec.V where the monodromy matrix is degenerate. The single eigenvalue has only a one-dimensional eigenspace.

One can obtain the general solution of (35) in several ways. For example, one may note that the two vectors

$$\boldsymbol{\xi}^{(1)}(t) = \begin{bmatrix}\cos(\omega t)\\ \sin(\omega t)\end{bmatrix}, \qquad \boldsymbol{\xi}^{(2)}(t) = \begin{bmatrix}-\sin(\omega t)\\ \cos(\omega t)\end{bmatrix}, \quad (36a)$$

satisfy

$$\frac{d\boldsymbol{\xi}^{(1)}}{dt} = \omega\boldsymbol{\xi}^{(2)}, \qquad \frac{d\boldsymbol{\xi}^{(2)}}{dt} = -\omega\boldsymbol{\xi}^{(1)}. \quad (36b)$$

Further, if the matrix on the right hand side of (35), without the factor ω, is designated $\hat{A}$, then

$$\hat{A}\boldsymbol{\xi}^{(1)} = \boldsymbol{\xi}^{(2)}, \qquad \hat{A}\boldsymbol{\xi}^{(2)} = \boldsymbol{\xi}^{(1)}. \quad (36c)$$

If we posit that a vector, $\boldsymbol{\xi}(t)$, solves (35), and if we expand it in terms of $\boldsymbol{\xi}^{(1,2)}$ as

$$\boldsymbol{\xi}(t) = a(t)\boldsymbol{\xi}^{(1)}(t) + b(t)\boldsymbol{\xi}^{(2)}(t),$$

with time-dependent coefficient $a(t)$ and $b(t)$, we find the conditions

$$\frac{\mathrm{d}a}{\mathrm{d}t} = -2\omega b, \qquad \frac{\mathrm{d}b}{\mathrm{d}t} = 0.$$

This shows that such a decomposition requires b to be a constant, $b = C_1$, and $a(t) = -2\omega C_1 t + C_2$, where C_2 is a second constant. In particular, a and b cannot both be constants, but there must be a *secular term* in the expansion. The general solution is

$$\begin{bmatrix}\xi_-\\ \eta_+\end{bmatrix} = (C_2 - 2C_1\omega t)\begin{bmatrix}\cos\omega t\\ \sin\omega t\end{bmatrix} + C_1\begin{bmatrix}-\sin\omega t\\ \cos\omega t\end{bmatrix}, \quad (37a)$$

with constants C_1 and C_2 chosen to match initial conditions. The initial conditions $\xi_- = 1, \eta_+ = 0$ correspond to $C_1 = 0, C_2 = 1$, the initial conditions $\xi_- = 0, \eta_+ = 1$ to $C_1 = 1, C_2 = 0$. At $t = T = \pi/\omega$ these have evolved to $(-1, 0)$ and $(2\pi, -1)$, respectively. Thus,

$$M = \Xi(T) = \begin{bmatrix}-1 & 2\pi\\ 0 & -1\end{bmatrix}. \quad (37b)$$

The eigenvalue $\rho = -1$ has a one-dimensional eigenspace. The secular term in (37a) reflects this degeneracy of the monodromy matrix.

VIII. CONCLUSIONS

The stability of leapfrogging motion has been investigated using Floquet theory. The numerical results of Acheson[5] were confirmed, and we found that the transition to instability occurs for the pair size ratio $\alpha = \phi^2$, the square of the golden ratio. The linear analysis does not explain the transition between the "walkabout" and "disintegration" instability modes identified by Acheson[5], but our numerical calculations has revealed that the transition is gradual rather than sharp, with both modes accessible by perturbation of a single leapfrogging motion. An example was given of leapfrogging occurring as an intermediate state in the chaotic scattering of vortex pairs[6]. We mention that the advection of particles by the periodic flow due to leapfrogging is chaotic. This has been explored by Péntek *et al.*[10].

ACKNOWLEDGMENTS

This work is supported in part by a Niels Bohr Visiting Professorship at the Technical University of Denmark sponsored by the Danish National Research Foundation.

Personal note by Laust Tophøj:
This paper is dedicated to the memory of Hassan Aref, who passed away during its preparation. He was a friend and a great inspiration.

[1] Helmholtz, H. von 1858 Über Integrale der hydrodynamischen Gleichungen, welche den Wirbelbewegungen entsprechen. *Journal für reine und angewandte Mathematik* **55**, 25-55. English translation by P. G. Tait, "On integrals of the hydrodynamical equations, which express vortex-motion." *Philosophical Magazine* (4) **33**, 485-512 (1867).

[2] Yamada, H. & Matsui, T. 1978 Preliminary study of mutual slip-through of a pair of vortices. *Physics of Fluids* **21**, 292-294.

[3] Gröbli, W. 1877 *Spezielle probleme über die Bewegung geradliniger paralleler Wirbelfäden, Vierteljahrsschrift der Naturforschenden Gesellschaft in Zürich* **22**, 37-81, 129-165.

[4] Love, A. E. H. 1894, On the motion of paired vortices with a common axis. *Proceedings of the London Mathematical Society* **25**, 185-194.

[5] Acheson, D. J. 2000 Instability of vortex leapfrogging. *European Journal of Physics* **21**, 269-273.

[6] Tophøj, L. & Aref, H. 2008 Chaotic scattering of two identical point vortex pairs revisited. *Physics of Fluids* **20**, 093605.

[7] Floquet, G. 1883 Sur les équations différentielles linéaires à coefficients périodiques. *Annal Scientifiques de l'É.N.S.* (2nd series), **12** 47-88.

[8] Nayfeh, A. H. & Balachandran, B. 1995 *Applied Nonlinear Dynamics – Analytical, Computational and Experimental Methods.* (John Wiley & Sons, Inc., New York)

[9] Eckhardt, B. & Aref, H. 1988 Integrable and chaotic motions of four vortices II. Collision dynamics of vortex pairs. *Philosophical Transactions of the Royal Society (London)* A **326**, 655-696.

[10] Péntek, A., Tél, T. & Toroczkai, T. 1995 Chaotic advection in the velocity field of leapfrogging vortex pairs. *Journal of Physics A: Mathematical and General* **28** 2191-2216.

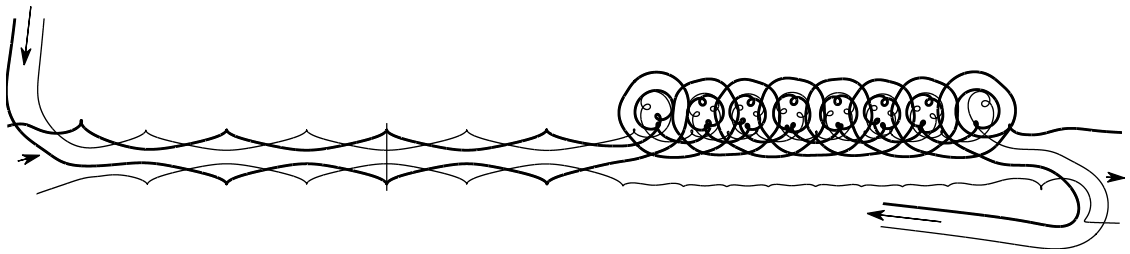

FIG. 6. Scattering of two identical vortex pairs showing intermediate states consisting of leapfrogging and "walkabout" motions. The vertical bar marks the starting leapfrogging configuration, $\alpha = 0.25, (\xi_-, \eta_+) = (-1, 1) \cdot 10^{-5}$, from which time is integrated forwards and backwards. The computation has been checked by reverse integration, and the variation of the integrals of motion is of negligible order (10^{-12}).

Chapter 3

Collisions of wet elastic spheres

In this diminutive chapter, I include the results from my visit to École Polytechnique in the spring of 2010, where I worked at the Laboratoire d'Hydrodynamique under the guidance of Christophe Clanet. I studied the effect on elastic collisions of steel spheres by applying a thin layer of viscous fluid to the surface of the target. The presence of the fluid film significantly alters the outcome of a collision, with a large fraction of the energy being dissipated during a very short time interval. Sometimes, the projectile even sticks completely to the target. I encountered some rather interesting results, suggesting that the pre-existing theory by [Barnocky & Davis (1988)] does not accout well for the basic observations, and furthermore that surface tension might play a key role. Unfortunately, we still lack a thorough understanding of the physical mechanism, and we have not moved to publish this work. It remains a standing problem to fully understand these collisions and the energy transfer processes that govern the outcome.

COLLISIONS OF WET ELASTIC SPHERES

Laust Tophøj

July 14, 2010, Technical University of Denmark
laust@fysik.dtu.dk

Abstract

This report summarizes an experimental study performed February-May 2010 at the Laboratoire d'Hydrodynamiqe (LadHYX) of École Polytechnique in Paris. The work was supervised by Prof. Christophe Clanet[1].

The collision and possible rebound between elastic spherical particles and a coated plate is examined experimentally and discussed theoretically. A previous analysis based on the theory of viscous lubrication, cf. Barnocky and Davis (1988), seems unable to explain the observed phenomena. An alternative predictive law based on the experimental findings is proposed and discussed. The possible role of capillary effects is briefly adressed.

1 INTRODUCTION

Particle-particle collisions can behave in various ways. Depending on the energy dissipation, a collision may result in a rebound with variable energy or a capture, where the particles stick, losing all of the energy corresponding to their initial relative motion. The collision behaviour is vital to a number of phenomena and applications. Examples are aggregation of suspended particles and particle capture on the mucus-covered bronchiola walls in the lungs.

An analogous process is the head-on collision between an elastic sphere and a hard planar surface. This phenomenon is easily studied experimentally, and the behaviour is closely related to that of particle-particle collisions.

In the case where the ambient air can be neglected, the behaviour is simple. The rebound coefficient, defined as the ratio of outgoing to incoming particle velocities, is simply a constant. In other words, each collision dissipates a fixed fraction of the particle kinetic energy, typically a few percent.

A more complicated process arises when the ambient fluid cannot be ignored, cf. for example Gondret et al. (2002), who studied collisions at low Reynolds numbers. The dynamics is more complicated, and the dynamic fluid viscosity enters as a parameter. The particles rebound when the impact velocity exceeds a critical value. The critical velocity is simply described by the relation St$\approx$10, where St is the Stokes number, cf. Gondret et al. (2002). This result is consistent with a theoretical analysis by Davis et al. (1986), who considered the viscous dissipation in the region between the particle and the wall in the lubrication approximation.

A third case arises when the target plate is covered by a thin layer of fluid. An image sequence of such a collision is shown in figure 1. This case was adressed experimentally by

[1] clanet@ladhyx.polytechnique.fr

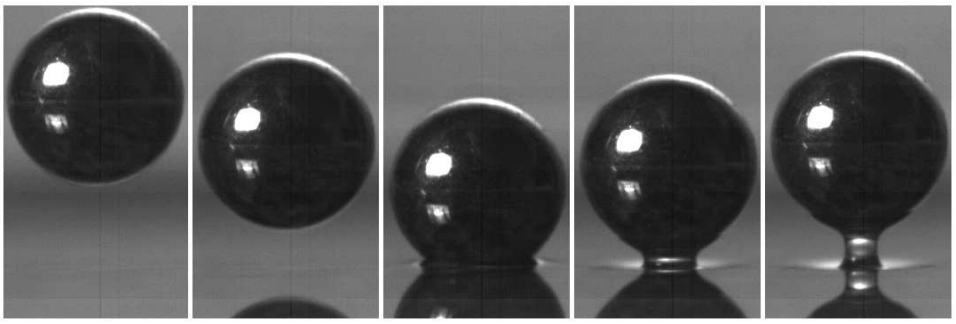

Figure 1: Montage of a collision between a steel sphere ($\emptyset = 5.5mm$) and a granite plate covered by a thin film (0.5mm) of viscous liquid (glycerol). The time between frames is 1ms. The output velocity is seen to be smaller than the input velocity, so a considerable fraction of the mechanical energy has been dissipated.

Barnocky and Davis (1988), who used the analysis of Davis et al. (1986) to develop a theoretical prediction of the critical impact velocity. The prediction involves a weak logarithmic dependence on the fluid film thickness. Subsequent experimental work was done by Le Goff (2009), Maudou et al. and Dupeux (2009). A considerable discrepancy between the experimental data and the theoretical prediction is observed in all cases, including the work by Barnocky and Davis (1988).

This report summarizes an experimental study aimed at clarifying this discrepancy and an attempt to find a predictive law accounting for the observed behaviour. It is organized as follows. The experimental setup is introduced in section 2. Sections 3 and 4 deal with the viscous dissipation and the theory of Barnocky and Davis (1988). Some theoretical developments are shown in section 3 and the experimental results are presented in section 4. As in previous studies, experimental results deviate significantly from the existing theory. The experiments allow the formulation of an empirical predictive law, which is presented in section 4. Section 5 adresses the influence of capillary forces at the fluid-air interface. A few experiments with varied contact angle are presented. A conclusion is given in section 6.

2 THE EXPERIMENT

A target plate (polished granite, about 5cm thick) is placed on a table and trimmed to be practically horizontal. A thin liquid film (of typical thickness 0.5mm) is applied to the table. The liquid is very viscous, typically with a dynamic viscosity about 1000 times that of water.

An impactor sphere is then dropped onto the target from a variable height. Special care must be taken to minimize the initial spin and horizontal velocity of the impactor sphere, so as to keep the problem simple and symmetric. Of the ones tested, the preferred release method consists of sucking the sphere onto the end of a rubber tube, and releasing by stopping the suction.

The collisions are studied with a high-speed video camera (operating at about 10000fps).

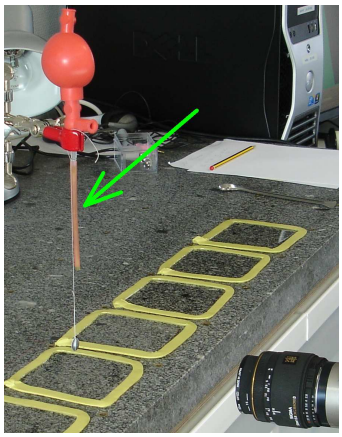

Figure 2: The experimental setup. The release mechanism is seen to the left. The rubber bulb provides suction for the rubber tube hanging down from it (the green arrow). The pending lead weight is used for aiming.

The liquid-filled basin is seen below. To the right is the lens of the video camera. The setup is lit from the left by a powerful lamp.

The impacts are filmed from the side, while being illuminated from the back. The high frame rates and the need for high spatial resolution mean that only a small region of space (and time) is recorded and in focus. The exposure time is necessarily short and a fairly small aperture is needed in order to get a reasonable depth of field. So a powerful light source behind a diffuser screen is needed. A persistent difficulty is to hit the small target area, so the release mechanism must be mounted such that its position can be accurately controlled.

A picture of the setup is shown in figure 2.

The liquid film thickness

The film thickness is controlled by letting a well-known volume of fluid (determined by weighing) settle to horizontal in a basin of known area. Near the basin edges, the liquid-air interface will deform due to surface tension. The basin wall is made of a sticky modelling paste (a commercial product called 'Tacky Tape'), on which the fluids used are wetting (contact angle $\theta_c < 90°$). The deformation has a cross section area $a \approx l_c^2/4$, where l_c is the capillary length. Denoting the liquid volume is V and the basin area is A and the circumference $4\sqrt{A}$, the film thickness is $\delta = V/A - a/4\sqrt{A}$. The basin area is measured on a top-down photograph and is typically about 10cm×10cm. For the typical liquid (silicon oil), $l_c \approx 1.4$mm, so the correction term is $a/\sqrt{A} \approx 20\mu$m. In the experiment, the film thickness ranges from 100μm to 1000μm, so the edge effect is a small correction, which will be neglected.

Film liquids

For the experiments presented in section 4, silicon oils were used. Silicon oils are easy to work with, in that they are available with a range of well-defined properties. They all have a very low surface-air energy, so they are wetting on most solids and they are not very susceptible to surface pollution.

Properties of silicon oils (Dow Corning) [2].:
$\rho_{V100} = 965\mathrm{kg/m}^3$, $\mu_{V100} = 0.0965\mathrm{Pa\,s} = 0.965\mathrm{Poise}$.
$\rho_{V1000} = 970\mathrm{kg/m}^3$, $\mu_{V1000} = 0.970\mathrm{Pa\,s} = 9.7\mathrm{Poise}$.
$\rho_{V5000} = 973\mathrm{kg/m}^3$, $\mu_{V5000} = 4.87\mathrm{Pa\,s} = 48.7\mathrm{Poise}$.

For the experiments presented in section 5, both silicon oils and glycerol were used. Glycerol has a viscosity very close to that of V1000 silicon oil, while the capillary properties are different. Glycerol tends to wet solids much less than silicon oils. Changing between the two is a means of testing the influence of capillary effects. One drawback is that the properties of glycerol depend sensitively on the water contents and the temperature. Glycerol also has a high affinity to water, so a bath of glycerol is quickly contaminated by water from the ambient air. The viscosities were found at a table at 'http://www.dow.com/glycerine/resources/table18.htm'. Experiments were performed at an ambient temperature of 21° C, and the fluid temperature, which was not measured, is presumably that. With glycerol of 99% purity (as indicated by the bottle label), the viscosity (interpolating linearly between the table values for 20 and 30°C) is $\eta = 1.085$Pa s, so very close to that of V1000 silicon oil.

Elastic solids

A number of spheres were tested in the experiments.

Steel spheres of diameters 4mm, 5.5mm and 10mm, with a density ρ_s =7800kg/m^3 and a Young's modulus E =190GPa and the Poisson ratio ν =0.29. The steel spheres used are nearly perfectly spherical, and the surfaces are smooth, so far as can be seen under the slight magnification in the videos.

Glass spheres of diameters 6mm and 10mm with $\rho_s = 2500$kg/m^3, E =72GPa and ν =0.29. The glass spheres that were available are not perfectly spherical, with deviations from spherical up to a few percent of the radius. Small grooves and imperfections are apparent in the video images. The glass surface is practical, in that the capillary properties may be controlled, for example by coating the glass with a thin layer of soot, rendering glycerol nearly non-wetting.

Polypropylene spheres of diameter 10mm with ρ_s =840kg/m^3, E =2.0GPa and ν =0.28. The polypropylene spheres are nearly spherical, but the surface roughness is not well-known.

The target plate is made of polished granite. The elastic properties are approximately given by $E = 40$GPa and $\nu = 0.3$. Note that the plate has a smaller Young modulus than do the steel spheres. The surface roughness is unknown. The plate is about 5cm thick. This is quite a bit greater than the impactor sphere radius, and the target plate will be thought of as occupying a half-space bounded by the surface plane.

Data processing

The collisions are studied using video recordings. Each frame of the video is an image like the one shown in figure 3 (Left). The impactor height at a given time ($z(t)$) is measured by the height of the top edge of the sphere. This height is assumed to represent adequately the

[2] Units used: $1\mathrm{Poise} = 1\mathrm{g/(cm\,s)} = 0.1\mathrm{Pa\,s}$. $1\mathrm{Stokes} = 1\mathrm{cm}^2/s = 10^{-4}\mathrm{m}^2/\mathrm{s}$

position of the rather rigid sphere, whose deformations are negligible in the present experiments. Time zero is defined as the time of lowest height, and that height is defined $z(0) \equiv 0$. Spacetime plots of the function $z(t)$ for a series of experiments are shown in figure 3 (Center).

The majority of measurements (figs. 6 to 10) have been analyzed simply by measuring the height at the central pixel column. In order to get a smooth reading for $z(t)$, a better method is to take the mean height along the width of the sphere. This technique enables differentiation of $z(t)$ and thus the extraction of reliable instantaneous velocities ($z'(t)$) and kinetic energies ($\propto [z'(t)]^2$), as in fig 13.

In the experiments, gravity merely acts as a motor, accelerating the impactor towards the target. The collision and the interaction between the impactor sphere and the fluid film take place over a very short time-scale (typically 10^{-4}s), over which the effect of gravity is negligible. When analyzing $z(t)$, it is advantageous to compensate for the gravitational acceleration by adding a term $\frac{1}{2}gt^2$ to $z(t)$. This is equivalent to changing to a freely falling frame of reference in which the target is stationary at the time of impact.

Once this is done, the input and output velocities (V_{in} and V_{out}) can be determined by taking the average velocity before and after the collision, excluding a short time interval near the time of impact, when the impactor may be interacting with the target. The rebound coefficient is defined as $e \equiv V_{out}/V_{in}$. A sequence of rebound coefficients measured for a range of V_{in} is shown in figure 3 (Right).

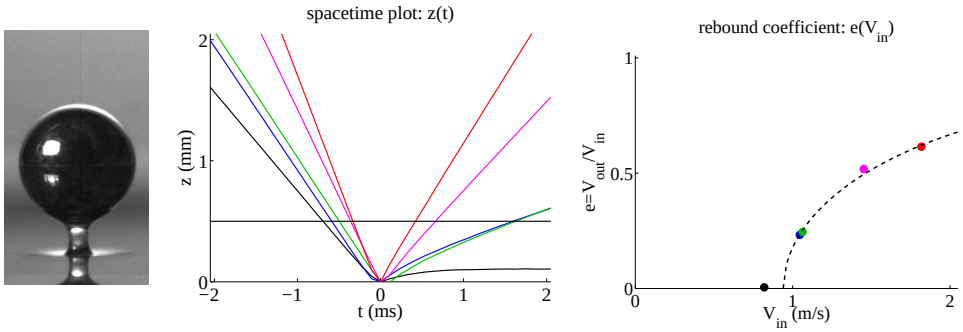

Figure 3: Extracting data from videos.

Left) Frame from a video recording. The impactor height at a given time is measured by the height of the top edge of the sphere. The most sophisticated method consists of taking the mean height along the width of the sphere. This gives a smoother reading for the height as a function of time.

Center) Spacetime plot extracted from high speed video footage. The example shows collisions at various speeds for a steel sphere of radius 5.5mm on a 500μm thick film of V1000 silicone oil. The height corresponding to the film thickness is marked by the horizontal black line. The rebound velocity is seen to vary strongly, becoming practically zero for the slowest impact (black curve). The resolution is high, the video is recorded at 9216fps, and the pixel resolution is about 30μm/pixel. The position is taken as an average over 200 pixel columns, so the corresponding position uncertainty is about $30\mu\mathrm{m}/\sqrt{200} \approx 2\mu m$.

Right) Rebound coefficient as extracted from the spacetime curves. The dashed curve is a fit.

3 THEORETICAL CONSIDERATIONS

Dry collisions

Dry collisions obey simple laws and serve as a good introduction to the present topic. Consider an elastic sphere bouncing on a rigid surface. The *coefficient of restitution* is defined as the ratio of the outgoing to the incoming velocity:

$$e \equiv \frac{V_{out}}{V_{in}}.$$

The coefficient of restitution was first introduced by Isaac Newton in the *Principia*. Newton observed that for any particular pair of sphere and rigid surface, the collisions are characterized by the simple law

$$e = \text{constant}, \tag{1}$$

with $0 < e < 1$. This is the source of the familiar behaviour of bouncing balls. The time of flight between two collisions is shorter than the time of the preceding flight by a factor of e. The time after n collisions is therefore longer than the time of the first flight t_0 by a factor $1 + e + e^2 + \ldots + e^{n-1}$. Continuing the sum, we get a convergent geometric series, meaning

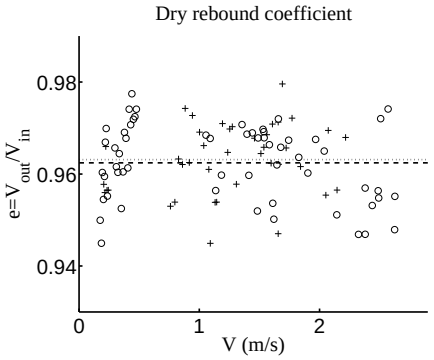

Figure 4: Rebound coefficients using a sound recording. The time interval t between consecutive impacts is recorded and the starting velocity is then given by $V = \frac{1}{2}gt$. Measurements are shown for glass spheres of diameter 10mm ($\circ$) and for steel spheres of diameter 5.5mm ($+$). The dotted and dashed lines at $e = 0.96$ show the average value for steel and glass, respectively. The rebound coefficient is practically constant over the range of impact velocities.

that the ball comes to rest at a finite time $t_0/(1-e)$. Ideally, the ball will reach its rest state only after an infinite number of collisions, and one can think of this phenomenon as a finite time singularity, where the bounce frequency blows up at a finite time.

Neglecting air resistance, the time of flight for a projectile launched vertically upwards with the velocity V is $t = 2V/g$. This relation can be used to determine the rebound coefficient directly from a sound recording. The bouncing of some glass and steel spheres on a granite table has been tested using this method, cf. figure 4. The result is in agreement with (1), with $e = 96\%$ for both glass and steel spheres.

The elastic deformation of the elastic sphere is studied using linear theory in the so-called *Hertz problem*. The elastically stored energy in the sphere deformed by a length z is given by $E\sqrt{R}\,z^{5/2}$, where R and E are the radius and the modulus of elasticity of the ball, cf. Falcon (1997). When a ball impacts after falling from a height h, the deformation is of order $z \sim R(\rho_s g h/E)^{2/5}$. For the typical experiment, $h \sim 1$m, $E \sim 10^{11}$Pa and $\rho_s \sim 10^4$kg/m^3, so the dimensionless factor is $z/R \sim (\rho_s g h/E)^{2/5} \sim 0.5\%$. I can thus safely assume that the ball deformation will be invisible.

The Stokes number

The Stokes number is a non-dimensional velocity. It is defined

$$\mathrm{St} \equiv \frac{2}{9}\frac{R\rho_s V_0}{\mu}, \tag{2}$$

where R and ρ_s are the radius and density of the sphere, and V_0 its initial velocity.

The Stokes number enters as a parameter whenever particle inertia competes with fluid viscosity. Consider for example a sphere in a viscous liquid moving with a velocity V. Neglecting fluid inertia, the sphere will come to a standstill under the viscous (Stokes) drag force $F_s = -6\pi R\mu V$. The equation of motion $m\frac{\mathrm{d}V}{\mathrm{d}t} = F_s$ has the dimensionless form

$$\frac{\mathrm{d}V}{\mathrm{d}\tilde{t}}(\tilde{t}) = -\frac{1}{\mathrm{St}}V(\tilde{t}) \tag{3}$$

where the non-dimensional time is defined in terms of the initial velocity by $\tilde{t} \equiv t/t_0$, with the time-scale $t_0 = R/V_0$.

Viscosity: Lubrication Results

The viscous force on a body approaching a plane may be computed using the lubrication approximation under the conditions that the gap seperating the solids is small and varies slowly across space.

Consider the axisymmetric flow between two axisymmetric bodies (cylindrical coordinates (r, θ, z)) with a radius dependent gap thickness $h(r)$. The bodies are approaching each other with the speed V. Assuming purely radial Stokes flow, the Stokes equation reads

$$\mu \frac{\partial^2 u}{\partial z^2}(r, z) = -\frac{\partial p}{\partial r}(r). \tag{4}$$

Now, using standard lubrication thinking, we assume the velocity profile everywhere to be parabolic, so that $\frac{\partial^2 u}{\partial z^2}(r, z) = 12\bar{U}(r)/h^2$, with $\bar{U}(r)$ denoting the gap-averaged radial flow velocity. By mass conservation we know that $V\pi r^2 = \bar{U}(r) r\, h(r)$, which we can insert into (4) to get

$$12\pi\mu \frac{V}{h^3} r = -\frac{\partial p}{\partial r}. \tag{5}$$

A flat disc approaching a plane: Inserting into (5) a flat height profile $h(r) = h_0$, one gets the result for the classic Reynolds problem of the viscous resistance of two disks separated by a narrow gap. The excess pressure in the gap is found by integrating (5) from an exterior radius R, where the pressure is ambient, giving $p(r) = (12\pi\mu V/h_0^3)(R^2 - r^2)$. The pressure force is then $F = \int_0^R 2\pi r \mathrm{d}r\; p(r) = 6\pi^2 \mu V R^4/h_0^3$.

A sphere approaching a plane: The sphere has radius R and the pole is a distance h_0 from the plane, so the height obeys $R^2 = r^2 + (h - h_0 - R)^2$. To first order in h and h_0, we have $h(r) = h_0 + \frac{1}{2} r^2/R$. One cannot simply disregard the first term when computing h^{-3}, as it is alway dominating in a neighbourhood of the origin.

Expanding in orders of r, we have $1/h^3 = \frac{1}{h_0^3} - \frac{3}{2}\frac{r^2}{R h_0^4}$. The function $1/h^3$ has a marked bump at the origin, the shape of which is reasonably well represented by the expansion. The quadratic has a root for $r = S \equiv \sqrt{\frac{2}{3} R h_0}$. We will pretend that this is the radius of ambient pressure and integrate from there. The integration yields

$$F = \frac{4\pi^2}{9} R^2 \mu V/h_0, \tag{6}$$

which is identical to the result of Davis et al. (1986), who used a different cut-off, except for the numerical prefactor.

On the result of Barnocky and Davis (1988)

With the prefactor 6π from Davis et al. (1986) put into (6), the equation of motion becomes

$$\frac{\mathrm{d}V}{\mathrm{d}\tilde{t}} = -\frac{1}{\mathrm{St}} \frac{V}{\tilde{z}}, \tag{7}$$

where St is based on the input velocity V_0, $\tilde{t}$ is time nondimensionalized by the timescale R/V_0 and $\tilde{z} \equiv h_0/R$. Here V and $\tilde{z}$ are functions of time. Noting that $\frac{1}{V}\frac{\mathrm{d}V}{\mathrm{d}\tilde{t}} = \frac{\mathrm{d}V}{\mathrm{d}\tilde{z}}$, (7) may be integrated through $\tilde{z}$, yielding

$$\frac{V}{V_0} = 1 - \frac{1}{\mathrm{St}} \log\left(\frac{\tilde{z}_0}{\tilde{z}}\right), \tag{8}$$

where $\tilde{z}_0$ is the nondimensionalized initial position. Barnocky and Davis (1988) used this to obtain a criteria for rebound, assuming that the sphere must approach the plane at least down to an elastic length scale l_e (typically a few μm) for significant elastic deformations and rebound to occur. In that case, the critical velocity is found when $V = 0$ at $z = l_e$, so the criterion becomes

$$\mathrm{St}^* = \log\left(\frac{z_0}{l_e}\right), \tag{9}$$

in terms of the critical Stokes number St* and the film thickness z_0. The logarithm means that this law involves a very weak dependence of St* on the film thickness as well as the elastic length scale. Note that according to the ideas of Davis et al. (1986) and Barnocky and Davis (1988), the two solids never actually come into contact.

We shall return to this prediction and compare it to experimental results in section 4.

Decay of deformations in the thin liquid film

The experiment relies on the ability of the thin liquid film to decay to horizontal, both after depositing and between collisions. The time scale of this process will now be discussed. Considering a thin film of thickness $h_0 + h$, where h_0 is constant and h varies slowly along the film, we can use the lubrication approximation. The pressure change induced by the deformation consists of a gravity term of the order of magnitude $\rho g h$ and a surface tension term of order $-\gamma\nabla^2 h$. The rate-of-change of h is then $\dot{h} \sim \frac{\rho g}{\mu} h_0^3 \nabla^2 h - \frac{\gamma}{\mu} h_0^3 \nabla^4 h$. Note that both terms act to stabilize the film against small deformations.

A typical impact leaves a small bump of radius $R \sim 1$cm in the film. Then, $\nabla^2 h \sim -h/R^2$ and $\nabla^4 h \sim h/R^4$, and

$$\dot{h} \sim -\frac{\rho g}{\mu}\frac{h_0^3}{R^2}\left(1 + l_c^2/R^2\right) h.$$

Typically, $l_c \ll R$, so gravity is the dominating restoring force. One part of the experimental work is the waiting for the film deformations to decay. The decay time is

$$\tau_g = \left(\frac{R}{h_0}\right)^2 \frac{\mu}{\rho g h_0}. \tag{10}$$

Evidently, the thickness is the critical parameter in the decay time. For a thick V5000 oil (5000 times the viscosity of water), the decay time ranges from merely 5s for a 1000μm thick film to an aggravating 1.5hours for a 100μm thick film.

4 EXPERIMENTS IN SILICON OILS

In order to determine the behaviour of wet collisions and in particular to test the theory of Barnocky and Davis (1988), a number of experiments have been performed. The liquid and

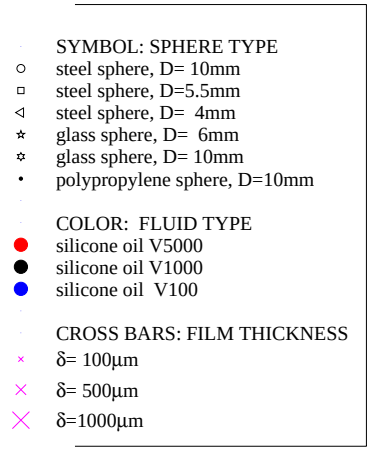

Figure 5: Legend for figs. 6-10.

A variety of liquid film/impactor sphere sets have been tested. The sphere type is indicated by the symbol. The spheres used are steel spheres of diameters 4, 5.5 and 10mm, glass spheres of diameters 6 and 10mm and polypropylene spheres of diameter 10mm. The fluid type is indicated by the color. The fluids used are silicon oils, V100, V1000 and V5000. The film thickness is indicated by a magenta × of size proportional to the film thickness. The film thickness ranges from 100μm to 1000μm.

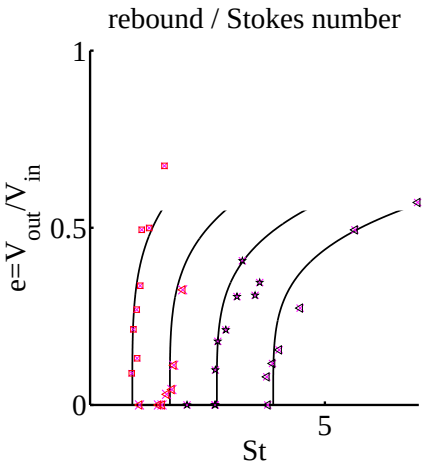

Figure 6: Rebound coefficient as a function of the Stokes number for a couple of experiments. Each of the four data sets fall approximately on one of the black curves. The shape of the curves are similar. The value of the Stokes number, for which the rebound coefficient becomes zero, will be called the critical Stokes number, St. It marks the transition between capture (St<St*) and rebound (St>St*).*

sphere types and the film thicknesses are shown in figure 5 together with a legend for the following figures. The majority of experiments are done using steel spheres, with the focus of varying in particular the impactor radius, the fluid viscosity and the film thickness.

For a given liquid film and impactor sphere, the rebound coefficient is determined for a range of impact velocities. A sample of the result is shown in figure 6. For each system (film-impactor pair), the data fall on some curve. The curves for different systems look similar, except that they are scaled by an individual factor in the Stokes number. The transition between capture and rebound occurs at a value of St, which is termed the *critical Stokes number*, St^*.

In figure 7, the rebound coefficients for the whole set of experiments is shown as a function of the normalized Stokes number St/St^*. The data collapse reasonably well, at least close to the transition, $St \approx St^*$. This indicates that the bouncing behaviour on liquid films near the

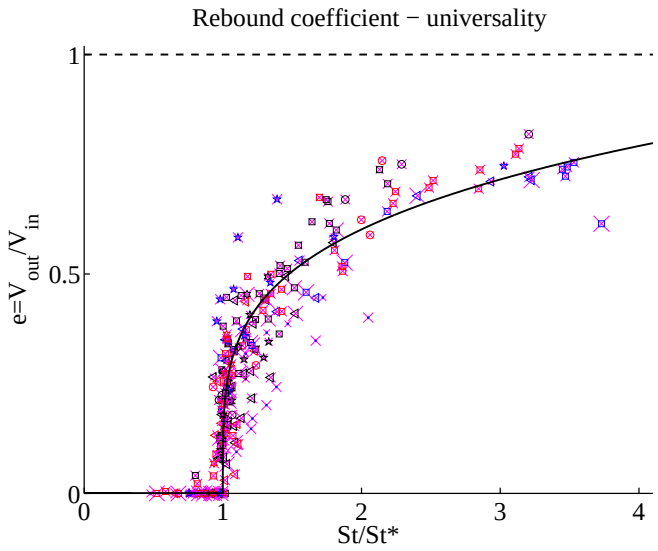

Figure 7: Rebound coefficients as a function of the normalized Stokes number, St/St. St* is the critical Stokes number, where the transition between capture and rebound occurs. The legend is shown in figure 5.*

It is seen that the data in the vicinity of the transition collapses fairly well to a single 'master' curve, indicating (11). In general, the rebound coefficient grows steeply from zero (the tangent is practically vertical) at the transition St=St, and slowly grows to a high value for large velocities, St/St* $\to \infty$.*

St is determined by fitting the master curve to the entire set of data, while optimizing also for St*. This is obtained through an iterative process.*

transition is described by a relation of the form

$$e = f\Big(\frac{\mathrm{St}}{\mathrm{St}^*}\Big), \tag{11}$$

where f is a universal function with $f(x < 1) = 0$ and $0 < f(x > 1) < 1$. This was remarked by Dupeux (2009) who, in line with Gondret et al. (2002) also normalized the rebound coefficient by the limiting value for $\mathrm{St/St}^* \to \infty$. Here, however, we shall focus on the transition and not the rebound coefficient far from it. Noting (11), the natural next step is to search for the behaviour of the critical Stokes number.

The behaviour of the critical Stokes number St^*

We saw in the above that the bouncing behaviour on a thin liquid film can be rather well understood, once we know the critical Stokes number, St^*, marking the transition from capture to rebound. The dependence of St^* on system parameters will now be discussed. The system parameters are:

- Fluid film properties - viscosity μ and film thickness δ.
- Impactor sphere - Density ρ_s and radius R.
- Material properties of target plate and impactor - Young's modulus and the Poisson ratio.
- Capillarity constants - Surface tension of the liquid γ and contact angle θ_c of the air-liquid-impactor contact line.
- Surface roughess - This parameter is not considered here. Cf. Barnocky and Davis (1988) for a discussion.

In the experiments, emphasis has been laid on varying the impactor sphere radius R, the fluid viscosity μ and the film thickness δ. In particular, steel spheres were used in the majority of experiments. The dependence of St* on these parameters has been plotted in log-log planes in figure 8. In each case, a power-law dependence is observed, i.e. $\mathrm{St}^* \propto \delta^{0.55}$, $\mathrm{St}^* \propto \mu^{-0.57}$ and $\mathrm{St}^* \propto R^{0.23}$. The dependance of St^* on material properties has not been explicitly tested, even though a few experiments have been done for varied sphere types.

These power laws suggest the possibility of collapsing all the data, with R, μ and δ varied, to a single curve. This is done in figure 9, where St^* is plotted as a function of the combined parameter $R^{1/5}\sqrt{\delta/\mu}$. The data is found to collapse well to the empirical power law

$$\mathrm{St}^* \approx 770 \left(R^{1/5} \sqrt{\frac{\delta}{\mu}} \ \left[\mathrm{m}^{-6/5} \mathrm{s}^{-1/2} \mathrm{kg}^{1/2} \right] \right)^{1.05}, \tag{12}$$

where the factor in the square brackets compensates for the dimensions of the combined parameters.

The fact that power law behaviour is observed indicates a balance between two physical effects. In this case, the governing law should be formulated

$$M = \text{constant}, \tag{13}$$

where M is a *dimensionless* number formed by combining powers of the physical parameters. Ignoring the power $1.05 \approx 1$ in (12) and referring to the definition of the Stokes number, (2),

$$M = V_0^* \, \frac{R^{4/5} \rho_s}{\sqrt{\mu \delta}} \cdot X, \tag{14}$$

where V_0^* is the critical impact velocity. The unknown quantity X must have the dimension $\mathrm{Length}^{6/5} \cdot \mathrm{Time}^{1/2} \cdot \mathrm{Mass}^{-1/2}$. Concluding from the experiments, X cannot depend very strongly on δ, μ or R. Note that the weak power in R occuring in (12) should not be taken too seriously. It may in fact be a R^0.

Comparison to the lubrication analysis of Barnocky and Davis (1988)

As discussed in section 3, Barnocky and Davis (1988) used the lubrication analysis of Davis et al. (1986) to formulate a theoretical prediction of the critical Stokes number as a function of system parameters. The law reads:

$$\mathrm{St}^* = \ln \frac{\delta}{L_e}, \tag{15}$$

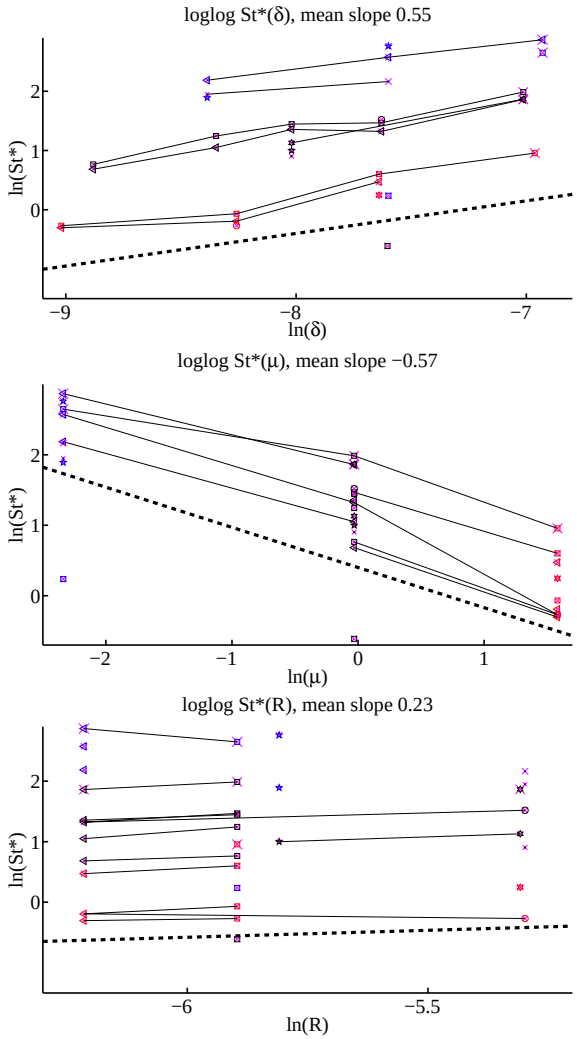

Figure 8: Looking for the behaviour of the critical Stokes number St^* *as a function of system parameters. Log-log planes are shown for* St^* *as a function of impactor sphere radius* R*, viscosity* μ *and film thickness* δ*. In each plot, black lines connect data points that differ only by the parameter of the abscissa. The power laws are deduced from the mean slope of these lines. The legend is shown in figure 5.*

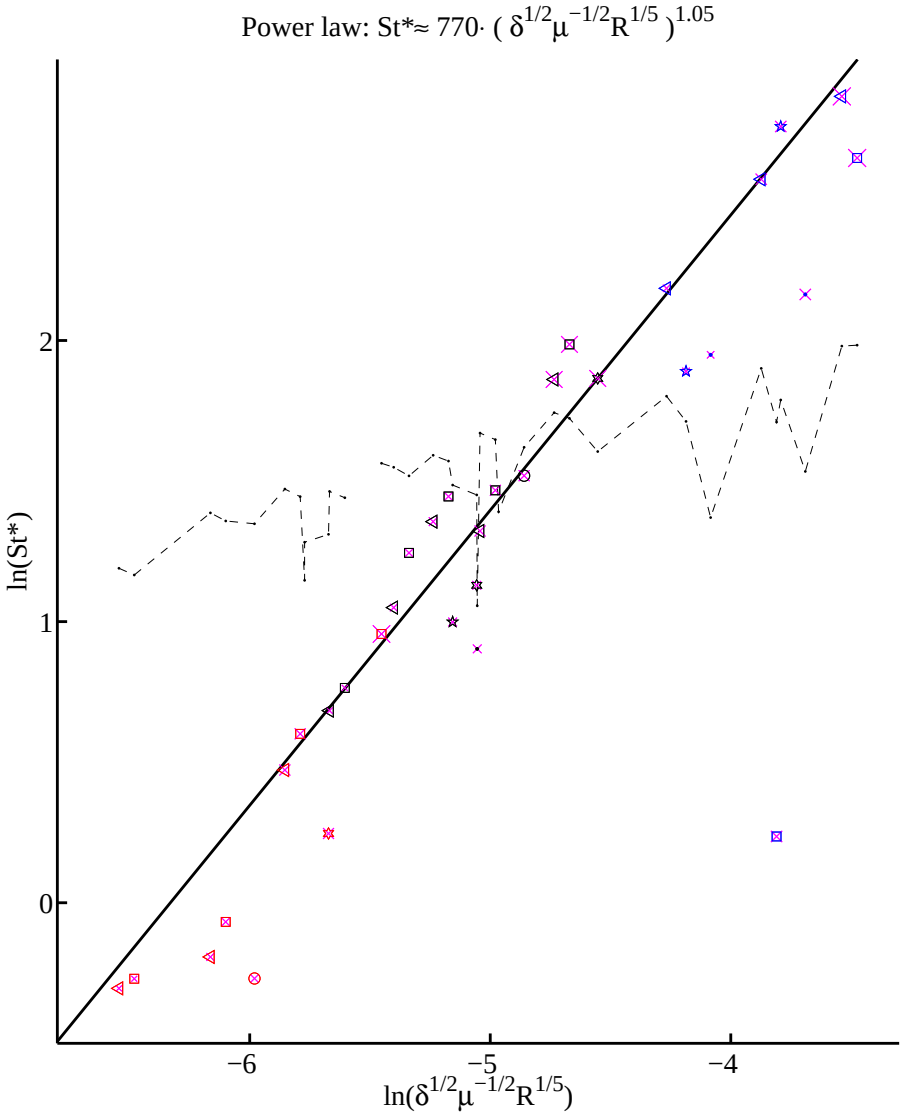

Figure 9: Collapse of all the data. A legend is shown in figure 5. The data is seen to collapse rather well to a power law.

The dots connected by a thin dashed line are the values of St^* *predicted by the theory of Barnocky and Davis (1988) for the corresponding system parameters. Clearly, the theory is unable to account for the distribution of data points. In particular, the theory predicts a much weaker variation in* St^* *than what is observed.*

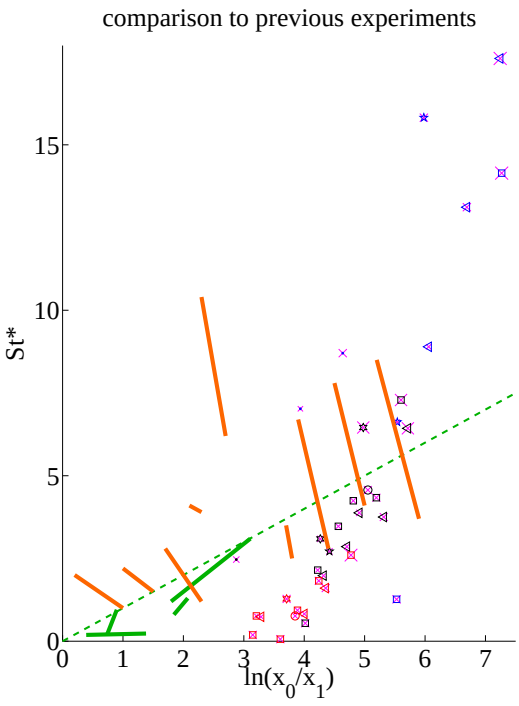

Figure 10: Comparison of the results to previous experiments.

The thick green bars mark the data from Barnocky and Davis (1988) (fig. 6) and the dashed green line mark the theoretical prediction $\mathrm{St}^* \sim \ln x_0/x_1$. *For each bar the film thickness is varied while the other parameters are held fixed. The same trend is observed in the present experiments.*

The thick orange bars mark the data from Maudou et al. (figs. 9 and 10). For each bar the sphere radius is varied while the film properties are held fixed. The same trend is observed in the present experiments.

It is apparent that the theory of Barnocky and Davis (1988) is unable to account for the observations. In particular, the data do not collapse onto a curve: Sphere radius variations and film thickness variations give rise to displacements along transversal directions in the plot. Hence the behaviour is not contained in a functional relation of the form $\mathrm{St}^* = f(x_0/x_1)$

where the elastic length scales like $L_e \sim (\mu V_0/E)^{2/5} R^{3/5}$. Here E is a characteristic Young's modulus for the combination of target and impactor materials. It is basically equal to Young's modulus of the less rigid material, which may be the target plate. Note that the critical impact velocity V_0 enters on both sides of (15).

The striking feature of (15) is the very weak dependence of St^* on system parameters. The predicted value of St^* for the actual system parameters is plotted in figure 9 together with experimental results. The figures clearly indicates that (15) underestimates the variation of St^*.

A more direct test of (15) is shown in figure 10, where the experimental results are plotted in a $\ln(\delta/L_e)$ - St^* plane (in the figure δ/L_e is denoted x_0/x_1). The figure also indicates the position of the data of Barnocky and Davis (1988) and Maudou et al.. The plot can be compared to Barnocky and Davis (1988) (fig. 6). The data are observed not to collapse, indicating that St^* is not a function of δ/L_e alone. In particular, variations in the sphere radius give rise to variations transversal to the prediction of Barnocky and Davis (1988). In fact, it seems that all data, including those of Barnocky and Davis (1988), vary transversally to the prediction curve.

Conclusion

In conclusion, the theoretical prediction of Barnocky and Davis (1988) seems unable to account for the observed behaviour of the critical Stokes number St^*. Rather, St^* appears to follow a power law, (12). In order to fully understand the empirical power law (12), one would need to formulate it in a dimensionally consistent way, showing explicitly the scaling behaviour on system parameters.

5 ON THE INFLUENCE OF CAPILLARY EFFECTS

Collisions on a liquid-coated plate involve movement and deformation of the free surface, cf. for example figure 12. The deformed surface is curved and supports capillary pressure discontinuities across the free surface. The mean curvature H and the surface tension (energy per surface area) are related to the pressure discontinuite Δp by the well-known Young-Laplace law,

$$\Delta p = 2\sigma H. \tag{16}$$

The resulting forces may be important to the capture dynamics. In this section, we shall discuss that effect.

The wetted radius after the collision

Figure 11 shows a measurement of the wetted radius after collisions in silicon oil. The simple geometric relation $R_{wet}^2 + (\delta - R)^2 = R^2$, or equivalently

$$\Big(\frac{R_{wet}}{R}\Big)^2 = 2\Big(\frac{\delta}{R}\Big) - \Big(\frac{\delta}{R}\Big)^2, \tag{17}$$

is seen to correspond very well to the measurements. Note that the measured wetted radii do not seem to depend on the impact velocity. A linearized version of (17) to be used below is $R_{wet} \approx \sqrt{2R\delta}$.

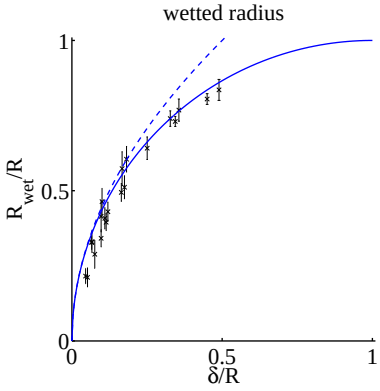

Figure 11: Wet radius and geometric prediction, (17). Measured after a series of collisions of steel spheres onto a film of silicone oil for varied impact velocity, sphere radius and film thickness. The geometric relationship (blue curve) and the linearized version (blue dashed) are seen to fit well to the measured radii, with no apparent dependence on other parameters.

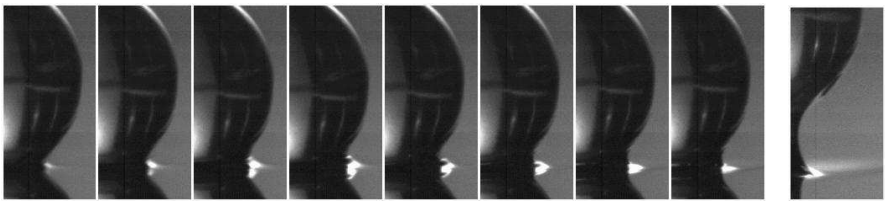

Figure 12: Close-up video montage of the deformed meniscus. A glass sphere ($\emptyset = 6mm$) impacts a 500μm thick layer of glycerol. To the left is shown 8 consecutive frames, separated by 0.1ms, and to the right is shown the liquid bridge 6ms after the time of closest approach.

A close look at the meniscus shape reveals a wave-like convex shape moving out near the contact line, until the direction of motion is reversed (frame number 6), and the shape abruptly shifts to concave. The curvatures involved are rather large (of order 1/100μm). The pressure in the liquid film near the contact line must change accordingly, cf. (16).

The rightmost image shows the liquid bridge that exists for a while during the rebound phase and eventually ruptures. The liquid bridge mediates an attractive force between the liquid film at the target and the impactor sphere.

The attractive force through the liquid bridge

A liquid bridge is usually formed in the collision, cf. figure 12. While the bridge persists, it mediates an attractive force between the liquid film and the impactor sphere, leading to further slowing down of the impactor sphere. If a quasistatic analysis is valid, the work involved in the breaking of a liquid bridge is of the order $W \approx 3.6\gamma\sqrt{RV}$, where R is the ball radius and V the bridge volume, cf. Simons et al. (1994). For small film thicknesses δ, the radius r of the wet area obeys $r^2 = 2R\delta$, and so $V \sim \delta r^2 = 2R\delta^2$. This gives $W \sim \gamma R\delta$.

The same result can be obtained in an even simpler way. The wetted area is of the order $r^2 \sim R\delta$, so

$$W \sim \gamma R\delta. \tag{18}$$

The kinetic energy of the sphere is $T \sim R^3\rho_s V^2$, so the energy to work-ratio is

$$\frac{T}{W} \sim \frac{R^2\rho_s V^2}{\gamma\delta} \sim 400, \tag{19}$$

for worst-case experimental conditions, $R \sim 2$mm, $V \sim 0.5$m/s, $\rho_s \sim 8000$kg/m^3, $\gamma \sim 20$mN/m, $\delta \sim 1000\mu$m. This seems to indicate that the attractive force through the liquid bridge is completely insignificant, at least so far as the quasistatic analysis goes.

Capillary work: The observed curvature

A close-up video montage of the meniscus during a collision is shown in figure 12. The meniscus as seen from the air is convex while the impactor moves into the liquid film, corresponding to a high-pressure near the contact line and a resistive force on the impactor motion. The meniscus curvature changes direction abruptly as the direction of motion is reversed, and the pressure must change accordingly. In figure 12, the curvature is seen to be of the order

$H \equiv 1/100\mu$m. The glycerol-air interface has a surface tension of about 64mN/m, so the pressure according to (16) would be of the order $\Delta p \sim$500Pa. The corresponding resistive force is of the order $\Delta p R\delta$. If this force were to persist while the sphere moves upwards a distance D from the bath, the work would be

$$W \sim \Delta p R \delta D. \tag{20}$$

Looking at figure 12, it seems that $D \sim \delta$. This work is greater than that of (18) by a factor $H\delta \sim 5$, the ratio of the curvatures. Hence the kinetic energy to capillary work would be of the order $T/W \sim 1/100$, still rather low.

We shall see below that capillary effects do seem to influence the capture dynamics. If a model were to be built on the basis of (20), one would need to understand the behaviour of the curvature H and the escape distance D as functions of system parameters.

Experiments

A few experiments have been done to test for the dependence of the critical Stokes number St^* on the capillary properties, the surface tension constant γ of the liquid-air interface and the contact angle θ_c of the liquid-air-impactor contact line.

In figure 13, the mechanical energy of the impactor sphere as a function of traversed distance is shown for steel spheres impacting liquid films of silicon oil and glycerol under other similar circumstances. The experiments are done for the same film thickness $\delta \approx 500\mu$m and the same viscosity $\mu \approx 10$Poise (1000 times the viscosity of water). In the figure, the mechanical energy of the impactor spheres is plotted as a function of the position. Also, the rebound coefficients as a function of impact velocity is shown. The critical velocity (where capture gives way to rebound) is significantly smaller in glycerol, indicating that the sphere is retarded less than in the case of silicon oil.

This would seem to indicate that the capillary properties are resbonsible for the different behaviours, since all other properties are nearly identical.

A further test is shown in figures 15 and 16. Two almost identical experiments are performed, with identical glass balls impacting the same liquid basin. The only difference is the surface properties of the impactor spheres. In the first experiment, the glass surface is clean (it has been soaking for 10 minutes in a 4mol/litre solution of sodium hydroxide), and the contact angle is $\theta_c = 27^\circ \pm 3^\circ$, i.e. the fluid is partially wetting, cf. figure 14. In the second, the glass surface has been covered by a thin layer of soot, rendering it very hydrophobic ($\theta_c \approx 180^\circ$). This is obtained by holding the sphere for a few seconds over a burning candle, until the surface has become completely black and opaque. Special care must be taken to ensure that the soot coating, which is porous and fragile, is not scraped off during handling. In practice only the impacting bottom side of the sphere is coated, and the adequacy of the coating is checked by looking at the free surface during collision.

In figure 15, a video montage of one of either type of collision is shown. The clean sphere impact leads to a large deformation of the liquid-air interface, as the liquid crawls up the sphere during collision. The soot-covered sphere, on the other hand, gives practically no visible deformation to the surface, which quickly recovers its initial flat shape after the collision. Dislodged fragments of soot are seen flying about after the collision.

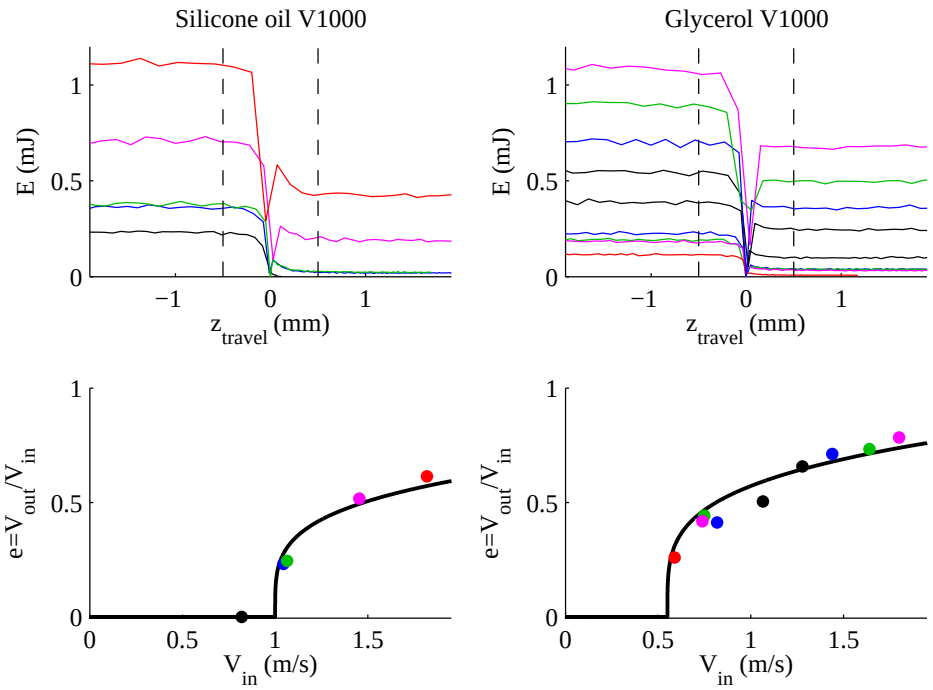

Figure 13: Varying the contact angle. Otherwise identical. The critical velocity is found to be 1.0m/s for silicone oil and only 0.55m/s for glycerol, while apparently only the contact angle is different. Note that the resisting force on the impactor $F = -\mathrm{d}E/\mathrm{d}z$ can in principle be extracted from this data as the slope of the curves.

Left) Silicone oil. The fluid is wetting, i.e. the contact angle is $\theta_c \approx 0$. Note that a considerable fraction of the lost energy is dissipated after the collision instant over a resolvable timescale. This is comparable to the time under which the sphere traverses the film thickness.

Right) Glycerol. The fluid is partially wetting with $\theta_c = 30.8^\circ \pm 2.3^\circ$. Note that the dissipation is smaller than in Silicone, and in particular that practically no dissipation takes place over a resolvable timescale.

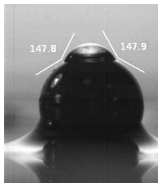

Figure 14: Measuring the contact angle. Here a drop of glycerol has been deposited on a steel surface.

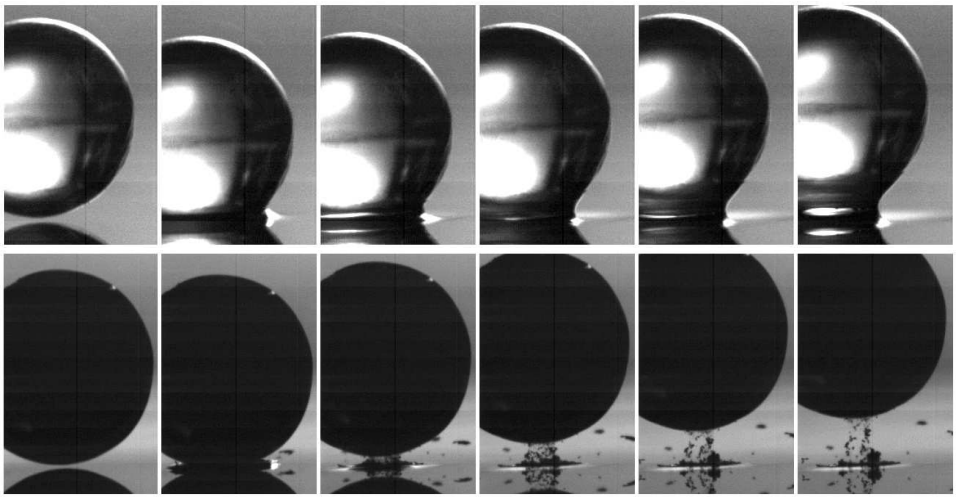

Figure 15: Rebound of a glass sphere ($\emptyset = 6mm$) in glycerol with different wetting angles. The time between frames is 0.5ms. The spheres impact with the same velocity $V_{in} = 1.05m/s$. The rebound coefficients are shown in figure 16.

Top) Clean sphere with contact angle $\theta_c = 27^\circ \pm 3^\circ$. Note how the contact line rapidly moves up the sphere as the glycerol wets the glass surface. A considerable amount of fluid is entrained in the liquid bridge connecting the plate and the sphere.

Bottom) And identical but soot-covered spheres impacting the same basin under non-wetting conditions ($\theta_c \approx 180^\circ$). The sphere rebounds with a much higher exit velocity than the clean sphere at the same impact velocity. After the sphere has flown off again, the fluid surface quickly regains its original shape. Notice the soot fragments that have been torn off the surface and are flying about after the collision.

It is apparent in figure 15 that the soot-covered sphere rebounds with a much larger velocity than does the clean sphere, in spite of nearly all parameters being the same. In particular, the input velocity is the same in the two cases, $V_{in} = 1.05$m/s. The surface coating must be responsible for the difference in behaviour. This may well be an effect of the changed wetting properties of the sphere surface, but another difference could also have an effect. The soot-covered sphere certainly has a higher roughness than the clean one, which may lead to enhanced flow between the sphere and the target plate during the collision, cf. Barnocky and Davis (1988). Also, air might be entrained in cavities at the hydrophobic soot surface, possibly altering the behaviour.

Rebound coefficients for both coated and clean spheres are shown in figure 16. The data indicated that the critical velocity is reduced by the soot coating, in agreement with the above remarks. However, only two collisions with soot-covered spheres were succesfully performed and recorded, so the amount of data is not overly convincing.

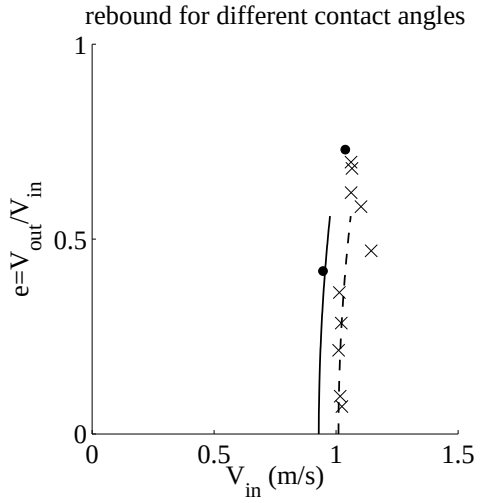

Figure 16: Rebound coefficients for impacts of a glass sphere in glycerol. Two configurations are tested. (×), Cleaned glass spheres under partial wetting (contact angle $\theta_c = 27^\circ \pm 3^\circ$) and, (•), identical but soot-covered glass spheres under non-wetting conditions ($\theta_c \approx 180^\circ$). A video montage is shown in figure 15.

It appears that the critical velocity is lower for the non-wetting situation (fitted by the solid curve) than for partial wetting (dashed curve). However, since only two data points are available for the non-wetting situation, the observation is hardly conclusive.

6 CONCLUSION

We have looked at the collisions between spherical particles and a hard surface coated by a thin liquid film, in particular the transition between capture and rebound. The existing theory of Barnocky and Davis (1988) was seen to underestimate the variation in the transition Stokes number. Furthermore, it was shown that the theory does not identify the correct parameters in the capture dynamics.

Instead, an empirical power law has been suggested, (12), which fits the data reasonably well. However, the law is not complete, in the sense that it is not yet formulated in the form $M =$constant, where M is a dimensionless number.

The effect of capillary forces has been addressed by a few experiments. The results indicate that capillary effects may play a role to the capture dynamics. In particular, changing the contact angle led to a considerable change in the critical impact velocity. This conclusion should not be taken too seriously, though, since very few experiments have been performed.

Outlook

Further work is needed to fully understand the capture dynamics of wet impacts. The influence of capillary forces and the contact angle might be examined through systematic experiments. It would be interesting to visually monitor the curvatures near the contact line during the collisions for a range of impact velocities, sphere sizes and liquid basins. Perhaps such a study could clarify the governing law, which should be put in dimensionless form.

On a practical note, the experiment becomes increasingly complex with increasing resolution and the introduction of a frail surface coating, such as the soot used in this study. For further experiments, I therefore recommend the construction of a more sturdy release mechanism allowing for a more secure aim.

I would like to thank Prof. Christophe Clanet for welcoming me so warmly at LadHYX. It was a pleasure to meet and work with the enthusiastic and professional people of the lab.

Bibliography

Guy Barnocky and Robert H. Davis. Elastohydrodynamic collision of two spheres: Experimental verification. *Phys. Fluids*, 31(6):1324–1329, 1988.

Robert H. Davis, Jean-Marc Serayssol, and E.J. Hinch. The elastohydrodynamic collision of two spheres. *J. Fluid Mech.*, 163:479–497, 1986.

Guillaume Dupeux. Report: *Rebonds sur film visqueux*, 2009.

Eric Falcon. *Comportements dynamiques associés au contact de Hertz...* PhD thesis, L'Université Claude Bernard - Lyon I, 1997.

P. Gondret, M. Lance, and L. Petit. Bouncing motion of spherical particles in fluids. *Phys. Fluids*, 14(6):643–652, 2002.

Anne Le Goff. *Impacts aux interfaces : freinage, rebond et capture.* PhD thesis, L'Université Pierre et Marie Curie, 2009.

Loïc Maudou, Mathieu Melgrani, and (MODEX). Rapport de MODEX MEC 441A phénomènes interfaciaux: *Étude du phénomène de capture d'une bille par un fluide visqueux* .

S.J.R. Simons, J.P.K. Seville, and M.J. Adams. An analysis of the rupture energy of pendular liquid bridges. *Chemical Engineering Science*, 49(14):2331 – 2339, 1994.

Bibliography

[Abrashkin *et al.* (1984)] Abrashkin, A. A. & Yakubovich, E. I. 1984 Planar rotational flows of an ideal fluid. *Soviet Physics Doklady* **29**, 370-371.

[Acheson (2000)] Acheson, D. J. 2000 Instability of vortex leapfrogging. *European Journal of Physics* **21**, 269-273.

[Aref *et al.* (1980)] Aref, H. & Pomphrey, N. 1980 Integrable and chaotic motions of four vortices. *Phys. Let. A* **78**, 297-300.

[Aref (1983)] Aref, H. 1983 Integrable, chaotic and turbulent vortex motion in two-dimensional flows. *Ann. Rev. Fluid Mech.* **15**, 345-389.

[Aref (1984)] Aref, H. 1984 Stirring by chaotic advection. *J. Fluid Mech.* **143**, 1-21.

[Aref (1985)] Aref, H. 1985 Chaos in the dynamics of a few vortices - fundamentals and applications. *Proc. of the 16th Int. Congress of Theoretical and Applied Mechanics, Lyngby, Denmark (1984)* pp.43-68.

[Aref (1989)] Aref, H. 1989 Three-vortex motion with zero total circulation: Addendum. *J. Appl. Math. & Phys. (ZAMP)* **40**, 495–500.

[Aref *et al.* (1996)] Aref, H. & Stremler, M. A. 1996 On the motion of three point vortices in a periodic strip. *J Fluid Mech.* **314**, 1-25.

[Aref *et al.* (1999)] Aref, H. & Stremler, M. A. 1999 Four-vortex motion with zero total circulation and impulse. *Phys. Fluids* **11**, 3704-3715.

[Aref (2002)] Aref, H. 2002 The development of chaotic advection. *Phys. Fluids* **14**, 1315-1325.

[Aref *et al.* (2003)] Aref, H., Newton, P. K., Stremler, M. A., Tokieda, T. & Vainchtein, D. L. 2003 Vortex crystals. *Adv. Appl. Mech.* **39**, 1–79.

[Aref *et al.* (2006)] Aref, H., Stremler, M. A. & Ponta, F. L. 2006 Exotic vortex wakes – point vortex solutions. *J. Fluids and Structures* **22**, 929-940.

[Aref *et al.* (2011)] Aref, H., Roenby, J., Stremler, M.A. & Tophøj, L. 2011 Nonlinear excursions of particles in ideal 2D flows. *Physica D: Nonlinear Phenomena* **240**(2), 199–207. Included on p. 69.

[Arnold (1978)] Arnold, V. I. 1978 *Mathematical Methods of Classical Mechanics* (Springer, ISBN 0-3879-6890-3)

[Bach (2011)] Bach, B 2011 Bachelor thesis: *Experimental Studies of Rotating Flows with a Free Surface.* DTU Physics, Technical University of Denmark.

[Barnocky & Davis (1988)] Barnocky, G & Davis, R. H. 1988 Elastohydrodynamic collision of two spheres: Experimental verification. *Phys. Fluids*, **31**(6):1324–1329.

[Bergmann *et al.* (2011)] Bergmann, R. & Tophøj, L. & Homan, T. A. M. & Hersen, P. & Andersen, A. & Bohr, T. 2011
Polygon formation and surface flow on a rotating fluid surface *J. Fl. Mech.* **679**, 415-431. Included on p. 33.

[Bergmann *et al.* (2012)] Bergmann, R. & Tophøj, L. & Homan, T. A. M. & Hersen, P. & Andersen, A. & Bohr, T. 2012 Polygon formation and surface flow on a rotating fluid surface - ERRATUM. J. Fl. Mech. **691**, 605-606. Included on p. 51.

[Borisov *et al.* (2007)] Borisov, A. V., Mamaev, I. S. & Ramodanov, S. M. 2007 Dynamic interaction of point vortices and a two-dimensional cylinder. *J. Math. Phys.* **48**, 065403.

[Davis *et al.* (1986)] Davis, R. H., Serayssol, J. & Hinch, E.J. 1986 The elastohydrodynamic collision of two spheres. *J. Fluid Mech.*, **163** 479–497.

[Dupeux (2009)] Dupeux, G. 2009 *Report: Rebonds sur film visqueux.* Private communication.

[Eckhardt *et al.* (1988)] Eckhardt, B. & Aref, H. 1988 Integrable and chaotic motions of four vortices II. Collision dynamics of vortex pairs. *Philosophical Transactions of the Royal Society (London)* A **326**, 655-696.

[Falcon (1997)] Falcon, E. 1997 PhD thesis: *Comportements dynamiques associés au contact de Hertz...* L'Université Claude Bernard - Lyon I.

[Floquet (1883)] Floquet, G. 1883 Sur les équations différentielles linéaires à coefficients périodiques. *Annal Scientifiques de l'É.N.S.* (2nd series), **12** 47-88.

[Fruleux (2010)] Fruleux, A. 2010 Private communication.

[Godfrey (1988)] Godfrey, D. A. 1988 A hexagonal feature around Saturn's north pole. *Icarus* **76**, 335–356.

[Gondret *et al.* (2002)] Gondret, P., Lance, M. & Petit, L. 2002 Bouncing motion of spherical particles in fluids. *Phys. Fluids*, **14**(6):643–652.

[Gröbli (1877)] Gröbli, W. 1877 *Spezielle probleme über die Bewegung geradliniger paralleler Wirbelfäden*, *Vierteljahrsschrift der Naturforschenden Gesellschaft in Zürich* **22**, 37-81, 129-165.

[van Heijst *et al.* (1989)] van Heijst, G. J. F. & Kloosterziel, R. C. 1989 Tripolar vortices in a rotating fluid. *Nature* **338**, 569-571.

[Helmholtz (1858)] Helmholtz, H. von 1858 Über Integrale der hydrodynamischen Gleichungen, welche den Wirbelbewegungen entsprechen. *Journal für reine und angewandte Mathematik* **55**, 25-55. English translation by P. G. Tait, "On integrals of the hydrodynamical equations, which express vortex-motion." *Philosophical Magazine* (4) **33**, 485-512 (1867).

[Hirsa, Lopez & Miraghaie (2002)] Hirsa, A. H., Lopez, J. M. & Miraghaie, R. 2002 Symmetry breaking to a rotating wave in a lid-driven cylinder with a free surface: Experimental observation. *Phys. Fluids* **14**, L29–L32.

[Jansson *et al.* (2006)] Jansson, T. R. N., Haspang, M. P., Jensen, K. H., Hersen, P. & Bohr, T. 2006 Polygons on a rotating fluid surface. *Phys. Rev. Lett.* **96**, 174502.

[Joukovskii (1892)] Joukovskii, N. E. 1892 Helmholtz's works on mechanics. In: *Hermann von Helmholtz 1821-1891. Publichnye lekcii, chitannye v Imperatorskom Moskovskom universitete v pol'zu Helmholtzovskogo fonda (Hermann von Helmholtz 1821-1891. Public lectures delivered at the Imperior Moscow University for the Helmholtz fund)*, A.G. Stoletov, ed., (Moscow University Press) pp.37–52 (in Russian).

[Kanso *et al.* (2008)] Kanso, E., & B. Oskouei 2008 Stability of a coupled body-vortex system. *J. Fluid Mech.* **800**, 77-94.

[Lamb (1932)] Lamb, H. 1932, *Hydrodynamics*, 6th ed., (Cambridge University Press, Cambridge)

[Landay & Lifshitz (1987)] Landau & Lifshitz 1987 *Fluid Mechanics, 2nd ed.* Butterworth-Heinemann

[Le Goff (2009)] Le Goff, A. 2009 PhD thesis: *Impacts aux interfaces: freinage, rebond et capture.* L'Université Pierre et Marie Curie.

[Lin (1943)] Lin, C. C. 1943 *On the motion of vortices in two dimensions* (University of Toronto Press, Toronto)

[Lopez *et al.* (2004)] Lopez, J. M., Marques, F., Hirsa, A. H. & Miraghaie, R. 2004 Symmetry breaking in free-surface cylinder flows. *J. Fluid Mech.* **502**, 99–126.

[Love (1894)] Love, A. E. H. 1894, On the motion of paired vortices with a common axis. *Proceedings of the London Mathematical Society* **25**, 185-194.

[Maxwell (1870)] Maxwell, J. C. 1870 On the displacement in a case of fluid motion. *Proc. London Math. Soc.*, **1-3**, 82-87.

[Michelin *et al.* (2009)] Michelin, S. & Llewellyn Smith, S. G. 2009 An unsteady point vortex method for coupled fluid-solid problems. *Theoretical and Computational Fluid Dyn.* **23**, 127-153.

[Milne-Thomson (1968)] Milne-Thomson, L. M. 1968 *Theoretical Hydrodynamics*, 5th ed., (MacMillan & Co., Ltd., London; republished by Dover Publications, New York)

[Miraghaie, Lopez & Hirsa (2003)] Miraghaie, R., Lopez, J. M. & Hirsa, A. H. 2003 Flow induced patterning at the air-water interface. *Phys. Fluids* **15**, L45–L48.

[Morton (1913)] Morton, W. B. 1913 On the displacements of the particles and their paths in some cases of two-dimensional motion of a frictionless liquid. *Proc. R. Soc. A* **89**, 106-124.

[Nayfeh *et al.* (1995)] Nayfeh, A. H. & Balachandran, B. 1995 *Applied Nonlinear Dynamics – Analytical, Computational and Experimental Methods.* (John Wiley & Sons, Inc., New York)

[Péntek *et al.* (1995)] Péntek, A., Tél, T. & Toroczkai, T. 1995 Chaotic advection in the velocity field of leapfrogging vortex pairs. *Journal of Physics A: Mathematical and General* **28** 2191-2216.

[Poncet & Chauve (2007)] Poncet, S. & Chauve, M. P. 2007 Shear-layer instability in a rotating system. *Journal of Flow Visualization and Image Processing* **14**, 85–105.

[Rabaud & Couder (1983)] Rabaud, M. & Couder, Y. 1983 A shear-flow instability in a circular geometry. *J. Fluid Mech.* **136**, 291–319.

[Roenby *et al.* (2010a)] Roenby, J. & Aref, H. 2010 Chaos in body-vortex interactions. *Proc. R. Soc. A* 466 **2119** 1871-1891

[Roenby *et al.* (2010b)] Roenby, J. & Aref, H. 2010 On the atmosphere of a moving body. *Phys. Fluids* **22**, 057103

[Rom-Kedar *et al.* (1990)] Rom-Kedar, V., Leonard, A. & Wiggins, S. 1990 An analytical study of transport, mixing and chaos in an unsteady vortical flow. *J. Fluid Mech.* **214**, 347-394.

[Saffman (1992)] Saffman, P 1992 *Vortex Dynamics* Cambridge University Press.

[Simons *et al.* (1994)] Simons, S.J.R., Seville, J.P.K. & Adams, M.J. 1994 An analysis of the rupture energy of pendular liquid bridges. *Chem. Eng. Science*, **49**(14):2331 – 2339.

[Suzuki, Iima & Hayase (2006)] Suzuki, T., Iima, M. & Hayase, Y. 2006 Surface switching of rotating fluid in a cylinder. *Phys. Fluids* **18**, 101701.

[Tasaka & Iima (2009)] Tasaka, Y. & Iima, M. 2009 Flow transitions in the surface switching of rotating fluid. *J. Fluid Mech.* **636**, 475–484.

[Tophøj *et al.* (2008)] Tophøj, L. & Aref, H. 2008 Chaotic scattering of two identical point vortex pairs revisited. *Physics of Fluids* **20**, 093605.

[Tophøj (2009)] Tophøj, L. 2009 Private communication. Results that were later included in the paper *Stationary ideal flow on a free surface of a given shape* given in this thesis, cf. p. 9.

[Vatistas (1990)] Vatistas, G. H. 1990 A note on liquid vortex sloshing and Kelvin's equilibria. *J. Fluid Mech.* **217**, 241–248.

[Vatistas, Wang & Lin (1992)] Vatistas, G. H., Wang, J. & Lin, S. 1992 Experiments on waves induced in the hollow core of vortices. *Exp. Fluids* **13**, 377–385.

[Vatistas, Wang & Lin (1994)] Vatistas, G. H., Wang, J. & Lin, S. 1994 Recent findings on Kelvin's equilibria. *Acta Mech.* **103**, 89–102.

[Vatistas *et al.* (2008)] Vatistas, G. H., Abderrahmane, H. A. & Kamran Siddiqui, M. H. 2008 Experimental confirmation of Kelvin's equilibria. *Phys. Rev. Lett.* **100**, 174503.

[Yamada *et al.* (1978)] Yamada, H. & Matsui, T. 1978 Preliminary study of mutual slip-through of a pair of vortices. *Physics of Fluids* **21**, 292-294.